Springer Theses
Recognizing Outstanding Ph.D. Research

Shu Fen Tan

Molecular Electronic Control Over Tunneling Charge Transfer Plasmons Modes

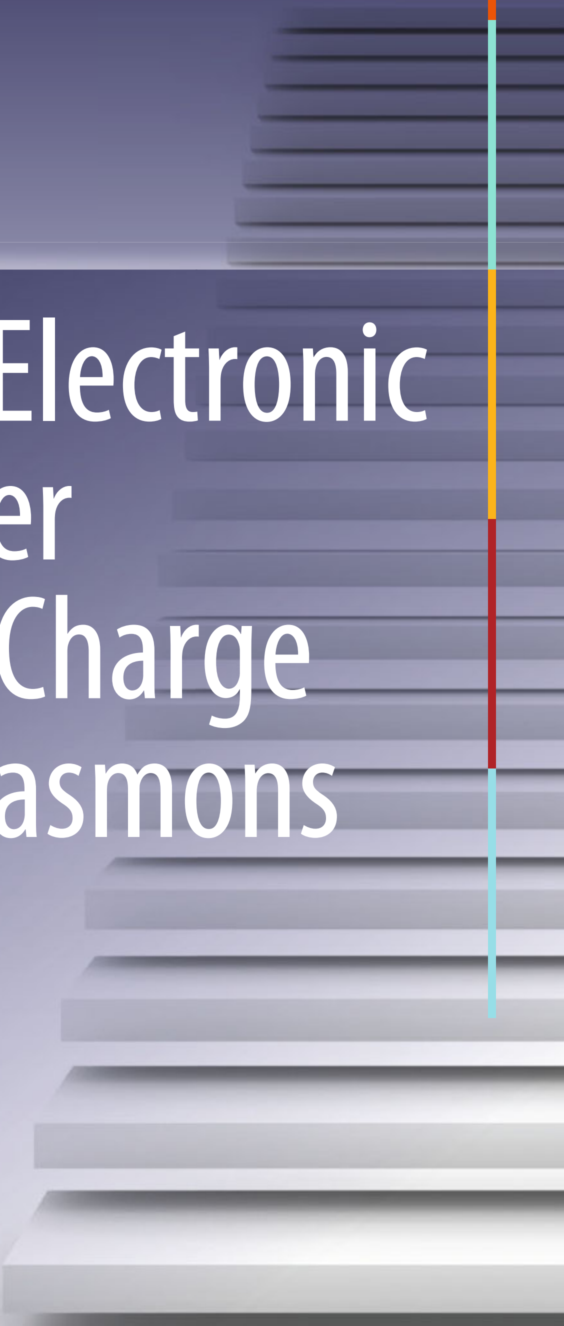

Springer

Springer Theses

Recognizing Outstanding Ph.D. Research

Aims and Scope

The series "Springer Theses" brings together a selection of the very best Ph.D. theses from around the world and across the physical sciences. Nominated and endorsed by two recognized specialists, each published volume has been selected for its scientific excellence and the high impact of its contents for the pertinent field of research. For greater accessibility to non-specialists, the published versions include an extended introduction, as well as a foreword by the student's supervisor explaining the special relevance of the work for the field. As a whole, the series will provide a valuable resource both for newcomers to the research fields described, and for other scientists seeking detailed background information on special questions. Finally, it provides an accredited documentation of the valuable contributions made by today's younger generation of scientists.

Theses are accepted into the series by invited nomination only and must fulfill all of the following criteria

- They must be written in good English.
- The topic should fall within the confines of Chemistry, Physics, Earth Sciences, Engineering and related interdisciplinary fields such as Materials, Nanoscience, Chemical Engineering, Complex Systems and Biophysics.
- The work reported in the thesis must represent a significant scientific advance.
- If the thesis includes previously published material, permission to reproduce this must be gained from the respective copyright holder.
- They must have been examined and passed during the 12 months prior to nomination.
- Each thesis should include a foreword by the supervisor outlining the significance of its content.
- The theses should have a clearly defined structure including an introduction accessible to scientists not expert in that particular field.

More information about this series at http://www.springer.com/series/8790

Shu Fen Tan

Molecular Electronic Control Over Tunneling Charge Transfer Plasmons Modes

Doctoral Thesis accepted by
the National University of Singapore, Singapore

Springer

Author
Dr. Shu Fen Tan
Department of Chemistry
National University of Singapore
Singapore

Supervisor
Assoc. Prof. Christian Nijhuis
Department of Chemistry
National University of Singapore
Singapore

ISSN 2190-5053 ISSN 2190-5061 (electronic)
Springer Theses
ISBN 978-981-10-8802-5 ISBN 978-981-10-8803-2 (eBook)
https://doi.org/10.1007/978-981-10-8803-2

Library of Congress Control Number: 2018939945

© Springer Nature Singapore Pte Ltd. 2018
This work is subject to copyright. All rights are reserved by the Publisher, whether the whole or part of the material is concerned, specifically the rights of translation, reprinting, reuse of illustrations, recitation, broadcasting, reproduction on microfilms or in any other physical way, and transmission or information storage and retrieval, electronic adaptation, computer software, or by similar or dissimilar methodology now known or hereafter developed.
The use of general descriptive names, registered names, trademarks, service marks, etc. in this publication does not imply, even in the absence of a specific statement, that such names are exempt from the relevant protective laws and regulations and therefore free for general use.
The publisher, the authors and the editors are safe to assume that the advice and information in this book are believed to be true and accurate at the date of publication. Neither the publisher nor the authors or the editors give a warranty, express or implied, with respect to the material contained herein or for any errors or omissions that may have been made. The publisher remains neutral with regard to jurisdictional claims in published maps and institutional affiliations.

Printed on acid-free paper

This Springer imprint is published by the registered company Springer Nature Singapore Pte Ltd.
part of Springer Nature
The registered company address is: 152 Beach Road, #21-01/04 Gateway East, Singapore 189721,
Singapore

Supervisor's Foreword

Today's computer chips process information at clock rates in the order of a few gigahertz (GHz), or a few billion cycles per second. Imagine a computer that can operate at a speed which is tens of thousands times faster than current microprocessors or close to the frequencies of visible light. Light is already used as an information carrier and transmitted through fiber optic cables, but these large optical elements are diffraction limited and a major challenge is to combine the ultrafast properties of photonic elements with nanoscale electronics.

To bridge the gap between fast operating speed optics and small scale of microelectronics, metal nanoparticles are seen as potential candidates due to their unique capability of interacting with light so as to produce surface plasmons (SPs). SPs are collective, ultrafast oscillations of electrons at metal-dielectric interface.

Shu Fen's thesis revealed a new way to generate an extremely rapidly oscillating current between two metal nanoparticles bridge by molecules that define the tunneling pathway between the two nanoparticles. Based on a physical effect called quantum plasmonic tunneling, her work essentially proves that it is possible to design optical circuits where tunnel currents are generated by light. These results imply that it is possible to vastly speed up the computing speeds to the hundred-terahertz (THz) regime, allowing the integration of optical and electronic components.

Her Ph.D. work is a pioneering effort in this new field of molecular plasmonics, in which the frequency of the tunnel currents (between 140 and 245 THz) can be tuned by simply changing the chemical structure (and by doing so the electronic structure) of the molecules inside the tunneling gap. In this way, the tunneling rate between the two metal nanoparticles can be precisely controlled. These findings were published in the prestigious journal ***Science***. This journal article was not only commented by an expert, Prof. Peter Nordlander in journal of ***Science*** perspectives, but also highlighted in reputable media, such as *Science Daily*, *Nanowerk* and also a broadcast report/radio story in *Techfocusmedia.net* etc.

Her thesis also describes an extensive study on other related practical issues such as the stability of the metal nanoparticles under electron beam irradiation and the real-time visualization of chemical reactions of metal nanoparticles in solution. These studies provided a quantitative picture of the nanoparticle growth process which is useful for engineering the composition and morphology of metal nanoparticles that could potentially open up more opportunities for application in plasmonics.

Her thesis work was conducted between 08/2011 and 08/2015 at the National University of Singapore, leading to several high-impact publications and presentations at international conferences. This work was honored by multiple prestigious academic awards, including the Best Graduate Researcher Award 2014 from the Department of Chemistry, the TOP Graduate Researcher Award 2014 from the Faculty of Science NUS, the Best Poster Award 2015 at International Conference for Materials and Advanced Technologies (ICMAT) and Singapore National Institute of Chemistry (SNIC) Gold Medal for Most Outstanding Ph.D. Thesis in Chemistry for AY2015/2016.

Singapore
December 2017

Assoc. Prof. Christian Nijhuis

Thesis Declaration

I hereby declare that this thesis is my original work and it has been written by me in its entirety, under the supervision of Associate Professor Christian A. Nijhuis, Department of Chemistry, National University of Singapore. I have duly acknowledged all the sources of information which have been used in the thesis.

This thesis has not been submitted for any degree in any university previously.

The content of the thesis has been partly published in:

(1) Tan, S. F.; Wu, L.; Yang, J. K. W.; Bai, P.; Bosman, M.; Nijhuis, C. A. "Quantum Plasmon Resonances Controlled by Molecular Tunnel Junctions" *Science* **2014**, *343*, 1496.

(2) Tan, S. F.; Lin, G.; Bosman, M.; Mirsaidov, U. M.; Nijhuis, C. A. "Real-Time Dynamics of Galvanic Replacement Reactions of Silver Nanocubes and Au Studied by Liquid-Cell Transmission Electron Microscopy" *ACS Nano* **2016**, *10*, 7689.

(3) Tan, S. F.; Chee, S. W.; Lin, G.; Bosman, M.; Lin, M.; Mirsaidov, U. M.; Nijhuis, C. A. "Real-Time Imaging of the Formation of Au–Ag Core-Shell Nanoparticles" *J. Am. Chem. Soc.* **2016**, *138*, 5190.

(4) Tan, S. F.; Bosman, M.; Nijhuis, C. A. "Molecular Coatings for Stabilizing Silver and Gold Nanocubes under Electron Beam Irradiation" *Langmuir* **2017**, *33*, 1189.

August 2015 Shu Fen Tan

Acknowledgements

I would like to express my sincere appreciation to all the people who helped and supported me during the research and their contributions to the work presented here.

First of all, I would like to thank Associate Professor Christian, A. Nijhuis, my supervisor who gave me the opportunity to join his group as a Ph.D. student. Thank you so much for his guidance, stimulation in research, and dedication throughout my entire graduate study. Without his support, this thesis would not have been possible. I would like to thank my co-supervisor Associate Professor Michel Bosman in Department of Materials Science and Engineering, NUS. I am very grateful for his support in electron microscopy and his constructive inputs in writing process.

This work would have not been completed without the help and collaboration with people from different fields. I would like to thank Dr. Wu Lin and Dr. Bai Ping from A*STAR's Institute of High Performance and Computing, Singapore, who have contributed in modeling and simulations. I would also like to thank Associate Professor Joel Yang from Singapore University of Technology and Design, Singapore, for his contribution in plasmonics electronics study. Also, I would like to offer special thanks to Asst. Prof. Utkur M. Mirsaidov from Department of Physics who offered me his time, all the advice and knowledge about *in situ* liquid-cell electron microscopy. Thank you See Wee, Guanhua, and Zainul for their contribution to this work in liquid-cell electron microscopy study. Thanks all of you for the time you have invested, for your help, and guidance in Cryo Electron Microscopy Centre.

I wish to express sincere appreciation to all my colleagues and friends, and I owe many thanks to Jiang Li, Li Yuan, Wang Dandan, Gan Lu, Du Wei, Calvin Wong Pei Yu, and Harshini Venkata Annadata, for being such good colleagues and friends over the years during the good and bad moments. Thank you for your help, willing to discuss all kind of issues, and making such a nice atmosphere in a lab.

Finally, I wish to thank my family and friends in Malaysia and Singapore. Without their encouragement and support, I would not have made it this far.

Contents

Abbreviations

AA	L-ascorbic acid
BDP	Bonding dipole plasmon
BDT	1,4-benzenedithiol
BPDT	1,4-biphenyldithiol
CPK	Corey–Pauling–Koltun model
CTAB	Cetyltrimethylammonium bromide
CTP	Charge transfer plasmon
DIET	Desorption-induced electronic transitions
EBID	Electron beam induced deposition
EBL	Electron beam lithography
EDT	1,2-ethanedithiol
EDTA	Ethylenediaminetetraacetic acid
EDX	Energy-dispersive X-ray spectroscopy
EELS	Electron energy-loss spectroscopy
EG	Ethylene glycol
FCC	Face-centered cubic
FEM	Finite-element model
GLC	Graphene liquids cell
HAADF	High angle annular dark field
HDT	1,6-hexanedithiol
HOMO	Highest occupied molecular orbital
HRTEM	High-resolution transmission electron microscopy
LCEM	Liquid-cell electron microscopy
LSPR	Localized surface plasmon
LUMO	Lowest unoccupied molecular orbital
NDT	1,5-dimercaptonapthalene
NP	Nanoparticle
ODT	1,8-octanedithiol
OPV	4,4-dimercaptostilbene
PT	1-propanethiol

PVP	Poly (vinyl) pyrrolidone
QCM	Quantum-corrected model
SAMs	Self-assembled monolayers
SEM	Scanning electron microscopy
SERS	Surface-enhanced Raman spectroscopy
STEM	Scanning transmission electron microscopy
tCTP	Tunneling charge transfer plasmon
TEM	Transmission electron microscopy
THF	Tetrahydrofuran
TXM	Transmission X-ray microscopy
UPS	Ultraviolet photoelectron spectroscopy
UV-Vis	Ultraviolet–visible light spectroscopy
XPS	X-ray photoelectron spectroscopy

Symbols

D_c	Critical electron dose
d_l	Molecular length
d_g	Gap size
E_res	Plasmon resonance energy
E_s	Sputtering threshold energy
E_d	Displacement threshold energy
E_0	Incident energy
E_HL	HOMO-LUMO energy gap
E_gap	Gap field
E_plasmon	Plasmon energy stored in capacitor
$\hbar$	Planck constant
G_0	Quantum conductance
J_0	Hypothetical current when tunneling width equals to 0
m	Mass of charge carrier
$V_{deposition}$	Atom deposition rate
$V_{diffusion}$	Surface diffusion rate
ε_r	Relative static permittivity (dielectric constant)
ε_0	Vacuum permittivity
σ	Electron scattering cross section
β	Tunneling decay coefficient
φ	Barrier height
α	Energy level alignment of molecular frontier orbitals with respect to the Fermi levels of Ag electrode
λ	Absorption peak

List of Figures

List of Tables

Summary

This thesis describes the controlled immobilization of molecules between two cuboidal metal nanoparticles by self-assembly method to control over the quantum plasmon resonances. Unlike top-down nanofabrication, the molecules between the closely spaced metal nanoparticles could control the gap sizes down to sub-nanometer scales and act as the frequency controllers in the terahertz regime, providing a new control parameter in the fabrication of electrical circuits facilitated by quantum plasmon tunneling.

The first part of the thesis (Chaps. 3–5) describes the fabrication of high aspect ratio, sub-nanometer gaps between two cuboidal metal nanostructures, their application in quantum plasmonics, and the stability study of these nanostructures under the electron beam irradiation. We studied quantum mechanical effects of the metal-molecules-metal junctions by a combination of complimentary characterization techniques, e.g., electron microscopy, spectroscopy, and theoretically confirmed by quantum-corrected finite-element model (FEM) simulations. The second part of the thesis (Chaps. 6 and 7) deals with the real-time imaging of chemical reactions of cuboidal metal nanoparticles in solution.

Chapter 1 gives an introduction to this thesis and Chap. 2 provides a literature overview of the self-assembly of nanoparticles with sub-nanometer separations for application in plasmonics and stability study of the metal nanoparticles.

Chapter 3 describes the fabrication of the high aspect ratio gaps between metal nanoparticles with different mixed self-assembled monolayers (SAMs) of thiolates and dithiolates. We study the metal-molecules-metal nanostructures with various characterization techniques (TEM, 3D STEM Tomography, XPS, UPS, UV-Vis spectroscopy). Chapter 4 demonstrates the realization of quantum plasmon tunneling using the metal-molecules-metal junctions as a platform and electron microscopy as characterization techniques. We demonstrate how the molecules in the gaps control the gap sizes and the opto-electronic properties of the tunnel junctions, thereby providing a control over the tunneling charge transfer plasmon mode. In Chap. 5, we give a stability study of the cuboidal metal nanoparticles under electron beam and discuss the strategies that could be taken for avoiding radiation damage. The synthesis of high-quality cuboidal metal nanoparticles we use for quantum plasmonics requires deeper understanding of the reaction chemistry and kinetics at nanoscale. Chapters 6 and 7 describe the real-time visualization of chemical reactions of cuboidal metal nanoparticles in solution using liquid-cell electron microscopy techniques.

The result presented in this thesis shows that self-assembly in bottom-up nanofabrication is a promising strategy to obtain high aspect ratios gap between nanoparticles. Additionally, the molecules could act as the frequency controllers in terahertz regime, leading to the realization of molecular electronics at optical frequencies.

Chapter 1
General Introduction

1.1 Introduction

Light can be used as an information carrier and transmitted in fibre optic cables or in on-chip optical interconnects. Photonic circuit elements are large but they operate at frequencies close to 1 terahertz, several orders of magnitude higher than typical switching speeds in microchip transistors. As current state-of-the-art nano-electronic devices operate at length scales that are much smaller than the wavelength of visible or infrared light, the diffraction limit makes it very difficult to combine the ultra-fast properties of photonic elements with nano-scale electronics.

Metal nanostructures have drawn much attention in the research fields of physics and chemistry in the past decades due to their unique capability to interact with light so as to constitute surface plasmons, which are collective, ultra-fast oscillations of electrons at the metal-dielectric interface. Due to this high-frequency oscillatory nature of surface plasmons, they are seen as potential candidates to bridge the gap between optics and electronics. By combining the small scale of microelectronics and the fast operating speed of optics, surface plasmons promise to hold the key to great improvements in device efficiency and speed.

Plasmonic behavior of metals can be described by classical physics based on Maxwell's equations. However, these descriptions ignore quantum effects and fail for plasmonic systems with confined dimensions or interparticle gaps smaller than 1 nm. In the latter case, quantum mechanical tunneling between plasmonic structures becomes non-negligible when two plasmonic resonators are placed so closely in space that the plasmon-induced fields induce significant numbers of electrons to tunnel across the gap [1–11]. Direct experimental access to the resulting tunneling charge transfer plasmon mode is expected to open up new opportunities in, for instance, nano-scale opto-electronics, single molecule sensing, and non-linear optics [1].

Hints of such a quantum mechanical plasmon mode have been measured indirectly [6, 10], and were theoretically shown to become important at length scales

S. F. Tan, *Molecular Electronic Control Over Tunneling Charge Transfer Plasmons Modes*, Springer Theses, https://doi.org/10.1007/978-981-10-8803-2_1

< 0.3 nm, inaccessible by present-day nanofabrication techniques. Top-down nanofabrication techniques such as electron-beam lithography (EBL) and photolithography do not provide the accuracy to fabricate such small gaps between two metal nanostructures accurately and reproducibly [12–14]. Due to this lack of resolution in device fabrication, quantum-plasmon effects have been difficult to investigate experimentally.

Despite the lack of control over the device layout design, wet chemical synthesis techniques and self-assembly in bottom-up nanofabrication provide a promising alternative strategy to achieve such narrow, high aspect ratio gaps at a large scale. Moreover, the molecules between the closely-spaced metal particles may act as frequency controllers in the terahertz regime, providing a new control parameter in the fabrication of electrical circuits that may show quantum plasmon tunneling effects. One of the key practical issues in this approach is the controlled immobilization of the molecules linking two metal nanoparticles (NPs) leading to well-characterized and stable nanostructures.

The research presented in this thesis focuses on the fabrication of high aspect ratio, sub-nanometer gaps between two cuboidal metal nanostructures and how these gaps are useful in quantum plasmonics. In Chap. 2, a literature overview is given on the self-assembly of NPs with sub-nanometer separations for application in plasmonics. Of particular interest is the stability study of the metal nanostructures.

Chapter 3 deals with the formation of sub-nanometer gaps (metal/molecules/ metal junctions) by functionalizing the cuboidal metal NP with different mixed self-assembled molecular monolayers (SAMs) of thiolates and dithiolates.

Chapter 4 demonstrates the application of such high aspect ratio gaps to realize quantum plasmon tunnelling. Using electron microscopy characterization techniques, we demonstrate how the molecules in the gap control the gap sizes and the electronics properties of the junctions, providing a way to control the tunnelling charge transfer plasmon mode.

In Chapter 5, we do a step back and give a more detailed stability study on the cuboidal metal NPs under electron beam irradiation. This chapter discusses the sample degradation effects and the preventive approaches that could be taken against radiation damage during experiments involving high energy electron beams encountered in transmission electron microscopes (TEMs) for instance.

The synthesis of the high-quality cuboidal metal NPs that we produce for quantum plasmonics is not trivial, and its success directly depends on the reaction chemistry and kinetics during synthesis. A key issue in the field of wet-synthetic NP synthesis is the real-time visualization of the chemical reaction to track the reaction kinetics and dynamics at nanoscale. The mechanisms of the formation of NPs during chemical synthesis in solution have been widely studied using *ex situ* methods. A popular method is to stop the reaction at various stages and image the intermediate reaction products by various techniques based on TEM. Chapters 6 and 7 describe the mechanisms of the galvanic replacement reaction between silver (Ag) nanocubes and chloroauric acid, and the overgrowth of Ag on gold (Au) nanocubes in aqueous medium, respectively, followed in real-time with *in situ* TEM using liquid-cell.

The last Chapter gives a summary and the conclusions, as well as an outlook to further extend the work presented in this thesis.

References

1. Tame MS, McEnery KR, Ozdemir SK, Lee J, Maier SA, Kim MS. Quantum plasmonics. Nat Phys. 2013;9(6):329–40.
2. Brongersma ML, Shalaev VM. The case for plasmonics. Science. 2010;328(5977):440–1.
3. Romero I, Aizpurua J, Bryant GW, García De Abajo FJ. Plasmons in nearly touching metallic nanoparticles: singular response in the limit of touching dimers. Opt Express. 2006;14 (21):9988–99.
4. Zuloaga J, Prodan E, Nordlander P. Quantum description of the plasmon resonances of a nanoparticle dimer. Nano Lett. 2009;9(2):887–91.
5. Marinica DC, Kazansky AK, Nordlander P, Aizpurua J, Borisov AG. Quantum plasmonics: nonlinear effects in the field enhancement of a plasmonic nanoparticle dimer. Nano Lett. 2012;12(3):1333–9.
6. Savage KJ, Hawkeye MM, Esteban R, Borisov AG, Aizpurua J, Baumberg JJ. Revealing the quantum regime in tunnelling plasmonics. Nature. 2012;491(7425):574–7.
7. Song P, Nordlander P, Gao S. Quantum mechanical study of the coupling of plasmon excitations to atomic-scale electron transport. J Chem Phys. 2011;134(7).
8. Kern J, Großmann S, Tarakina NV, Häckel T, Emmerling M, Kamp M, Huang J-S, Biagioni P, Prangsma JC, Hecht B. Atomic-scale confinement of resonant optical fields. Nano Lett. 2012;12(11):5504–9.
9. Esteban R, Borisov AG, Nordlander P, Aizpurua J. Bridging quantum and classical plasmonics with a quantum-corrected model. Nat Commun. 2012;3:825.
10. Scholl JA, García-Etxarri A, Koh AL, Dionne JA. Observation of quantum tunneling between two plasmonic nanoparticles. Nano Lett. 2012;13(2):564–9.
11. Duan H, Fernández-Domínguez AI, Bosman M, Maier SA, Yang JKW. Nanoplasmonics: classical down to the nanometer scale. Nano Lett. 2012;12(3):1683–9.
12. Broers AN, Molzen WW, Cuomo JJ, Wittels ND. Electron-beam fabrication of 80-Å metal structures. Appl Phys Lett. 1976;29(9):596–8.
13. Cord B, Yang J, Duan H, Joy DC, Klingfus J, Berggren KK. Limiting factors in sub-10 nm scanning-electron-beam lithography. J Vac Sci Technol, B. 2009;27(6):2616–21.
14. Ou FS, Hu M, Naumov I, Kim A, Wu W, Bratkovsky AM, Li X, Williams RS, Li Z. Hot-spot engineering in polygonal nanofinger assemblies for surface enhanced raman spectroscopy. Nano Lett. 2011;11(6):2538–42.

Chapter 2
Plasmonic Properties, Stability and Chemical Reactivity of Metal Nanoparticles—A Literature Review

2.1 Introduction

Noble metal nanostructures are widely studied for applications in optics [1], meta-materials [2, 3], superlenses [4–6], photovoltaics [7–9], plasmonics [10], and sensing [11], due to their ability to interact with light to constitute surface plasmons [12] which are collective electron oscillations at optical frequencies (Fig. 2.1a) that can be manipulated at dimensions far below the diffraction limit [13]. Their high oscillation frequencies can potentially enable high speed transport of information (> 100 THz) to bypass the inherently limited operating speed of microelectronics. Another technological advantage is the potential to scale plasmonic resonators far below the diffraction limit, which provides a route to miniaturize photonic elements [14] (Fig. 2.1b), thereby improving the efficiency and speed of future electro-optical devices.

In this work, we aim to generate tunnel currents between plasmon resonators. This is challenging on an experimental level as discussed in Chap. 1, but also requires new simulation approaches that include quantum-mechanical effects beyond the commonly-used numerical methods that solve Maxwell's equations. In order to model the electron tunnelling, Esteban et al. [15] and Wu et al. [16] adopted a quantum-corrected model (QCM). The former shows that the observation of charge transfer plasmon mode (CTP) is expected only when the distance down to 0.3 nm [15] (indicated as by a red oval in Fig. 2.2a). Alternatively, an extremely high field (10^{10} V/m) is required to enable sufficient electrons to tunnel through a vacuum gap [16]. For this work, we collaborated with the latter group of Wu Lin and Bai Ping at IHPC (A*STAR) Singapore to support our experimental work with quantum-corrected simulations.

After the theoretical predictions were published, a few experimental attempts [17–19] have been carried out to investigate the plasmon-induced electron tunnelling phenomena. However, overinterpretation of the results often leads to too strong claims. For instance, Savage et al. [17] has no correlated distance

S. F. Tan, *Molecular Electronic Control Over Tunneling Charge Transfer Plasmons Modes*, Springer Theses, https://doi.org/10.1007/978-981-10-8803-2_2

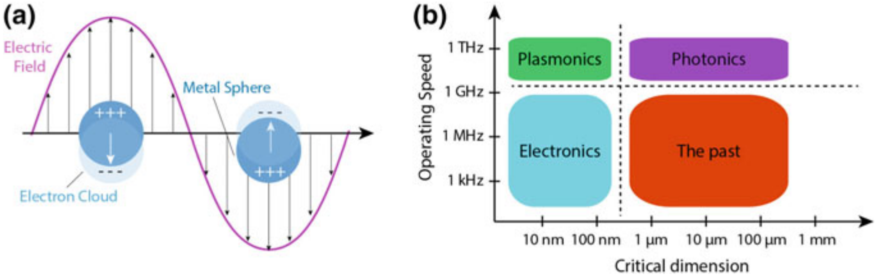

Fig. 2.1 **a** Surface plasmons are charge oscillations in noble metal nanostructures [12]. **b** Operating speed and critical dimension of various chip-scale device technologies [14]. Figure **a** adapted from Ref. [12]. Figure **b** reprinted from Ref. [14], with permission from Elsevier, Copyright 2006

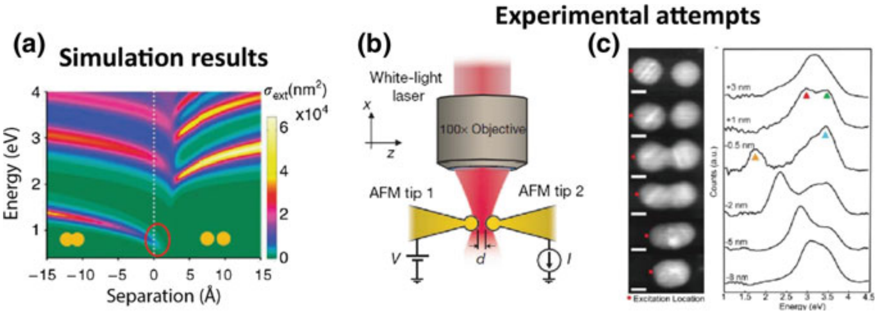

Fig. 2.2 **a** Simulation result [15] and **b**, **c** experimental attempts [17, 18] for observing the charge transfer plasmon mode (tCTP). Figure **a** reprinted from Ref. [15], with permission from Nature Publishing Group, Copyright 2012, **b** reprinted from Ref. [17], with permission from Nature Publishing Group, Copyright 2012, and **c** reprinted from Ref. [18], with permission from American Chemical Society, Copyright 2013

measurements as shown in Fig. 2.2b while Scholl et al. [18] did not investigate tunneling effect directly but indirectly in the form of a shift of the high-energy peak as shown by the red triangle in Fig. 2.2c which could also have caused unrelated to tunneling phenomena. For example, such a shift indicates the presence of electrostatic coupling, but it is not experimental evidence of tunneling. To prove the occurrence of tunneling, we need to observe the low-energy peak below 1 eV, while the resonators are not in contact with each other, according to theory: one needs to carry out optical measurements with spatial resolution far below the diffraction limit.

As mentioned in Chap. 1, the theoretically predicted small gaps (< 0.3 nm) that are necessary for tunneling to occur are inaccessible by state-of-the-art nanofabrication techniques. However, self-assembled monolayers of molecules serve as a potential method to bring the two nanostructures to close proximity. In addition, from routine experimental tunnel junctions in molecular electronics, molecules with their own characteristic highest occupied molecular orbital-lowest unoccupied molecular orbital (HOMO-LUMO) gaps are known to participate in energy level tuning of the studied plasmonic system. To investigate the quantum tunneling effect at this length scales (< 0.3 nm) and at these frequencies conclusively, atomic resolution imaging and single particle nano-optical spectroscopy is required, involving the utilization of transmission electron microscopy (TEM) and monochromated electron energy-loss spectroscopy (EELS). Thus, the stability of the nanostructures against electron beam damage becomes an important issue. In future, bimetallic or core-shell plasmon resonators may become important in the study of plasmon-induced tunneling, as they allow more flexibility in plasmon frequency-tuning. This thesis therefore also contains a section where galvanic replacement and overgrowth in solution are observed to form bimetallic and core-shell gold-silver nanoparticles (NPs).

To conduct this study, several questions must be answered: (i) How to precisely control the gap sizes between two nanostructures down to the quantum regime (< 1 nm)? (ii) What is the role of the self-assembled monolayer of molecules and how to correlate the molecular properties to the charge transfer plasmon mode? (iii) How does the stability of the metal nanostructures impact on the quantum plasmonics study? (iv) How does the chemical composition of the metal nanostructures change in the presence of other metal ions? Therefore, well-defined chemical and structural plasmonic nanostructures are needed to study quantum plasmonics in practice.

Here, we review recent progress of noble metal nanostructures in engineering sub-nm separations, characterization techniques to study the charge transfer plasmon mode, stability of the NPs against electron beam irradiation, and also their chemical reactivity with other metal ions in solution.

2.2 Engineering Sub-nm Gaps in Nanostructures for Applications in Plasmonics

A textbook system for studying the quantum mechanical tunneling is a NP dimer with a small gap. Engineering sub-10 nm gaps in nanostructure dimers or larger assemblies of nanostructures have been readily achieved by top-down and bottom-up approaches. Here, we briefly review these two general approaches, and discuss the pros and cons for each approach.

2.2.1 Top-Down Approach

Top-down fabrication techniques such as electron beam lithography (EBL) provide several advantages. (i) Tailorable metal patterns and arrays can be fabricated. For instance, particles of any geometries and sizes, can be arranged in any array including dimers, trimers, oligomers, chains, etc. (ii) It gives high yield and reproducibility over other techniques. Mirkin group [20–29] introduced a new method which is called on-wire lithography (Fig. 2.3a). This novel, high-throughput method is useful to synthesize one-dimensional arrays of metal nanostructures (Fig. 2.3b) that could control the separation between adjacent structures down to 1–2 nm. The drawbacks of EBL are: (i) it requires relatively complicated and expensive equipment, (ii) it can only generate metal patterns over small areas, (iii) it is difficult to up-scale without running into time restraints, and (iv) the metal patterns generated are polycrystalline, which can cause significant plasmon damping at grain boundaries.

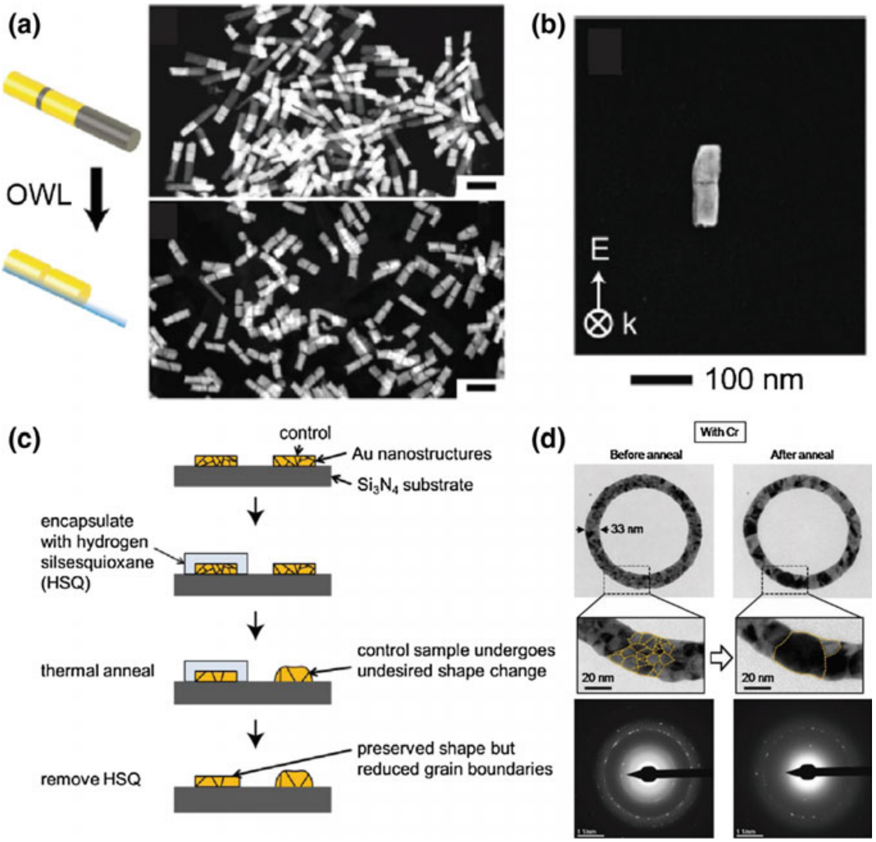

Fig. 2.3 **a** On-wire lithography (OWL) introduced by Mirkin's group and **b** the resulting gold nanorods dimers [20]. **c** Encapsulating annealing method reported by Bosman et al. and **d** the TEM image and electron diffraction pattern of the same ring structure before and after annealing [30]. Figure **a**, **b** reprinted from Ref. [20], with permission from American Chemical Society, Copyright 2012. Figure **c**, **d** reprinted from Ref. [30], with permission from Springer Nature, Copyright 2014

Moreover, surface roughness, adhesion layers and substrate effects have also been reported as causes of plasmon damping in EBL-fabricated samples. Bosman et al.[30]. reported a method of encapsulated annealing (Fig. 2.3c) that could preserve the shape of polycrystalline gold nanostructures, i.e. reducing the grain boundaries density (Fig. 2.3d) so as to reduce the plasmon damping in lithographically-defined structures. (v) It is unlikely to achieve routine sub-nanometer gap fabrication any time soon, which makes this top-down technique less useful for exploring plasmon-induced electron tunneling phenomena [31–33].

2.2.2 Bottom-Up Approach

On the other hand, aligning nanostructures with a small separation is relatively easily-achievable by wet-chemical solution processing methods. There are two common interactions used to assemble the NPs. (i) Supramolecular assembly where molecules act as the linkers for guiding the nanoparticle assembly. This can be done via covalent forces [34–41] (Fig. 2.4a, b) such as metal-thiolate covalent bonding or non-covalent (Fig. 2.4c) interactions [42–44] such as van der Waals interaction, electrostatic forces, etc. (ii) Solvent interactions [45–49] (Fig. 2.4d) where the assembly is driven by solvent-mediated interactions among hydrophobic ligands such as alkanethiols selectively bound to one side of the NPs and hydrophilic surfactants such as cetyltrimethylammonium bromide (CTAB) on the other side of the NPs.

Wet-chemical or bottom-up approaches have been widely used for synthesizing silver NPs of different sizes[124] [51] and shapes [52–55] with high monodispersity. Chemically-synthesized NPs are single-crystalline and experience less plasmon damping than those lithographically-defined nanostructures. In particular, the atomically smooth surfaces of silver nanocubes would enable the formation of high-quality interparticle gaps with distinct and flat interfaces. In addition, wet-chemical methods facilitate large-scale production of nanostructures without escalating time restrictions. Unlike top-down lithography, in wet-chemical synthesis, it is possible to control the inter-particle distance with the surface molecules.

However, large scale solution-phase method encounters reproducibility problems because of a lack of control over the assembly process, so the yield of—say—particle dimers is typically much lower for wet-chemical synthesis than for top-down methods.

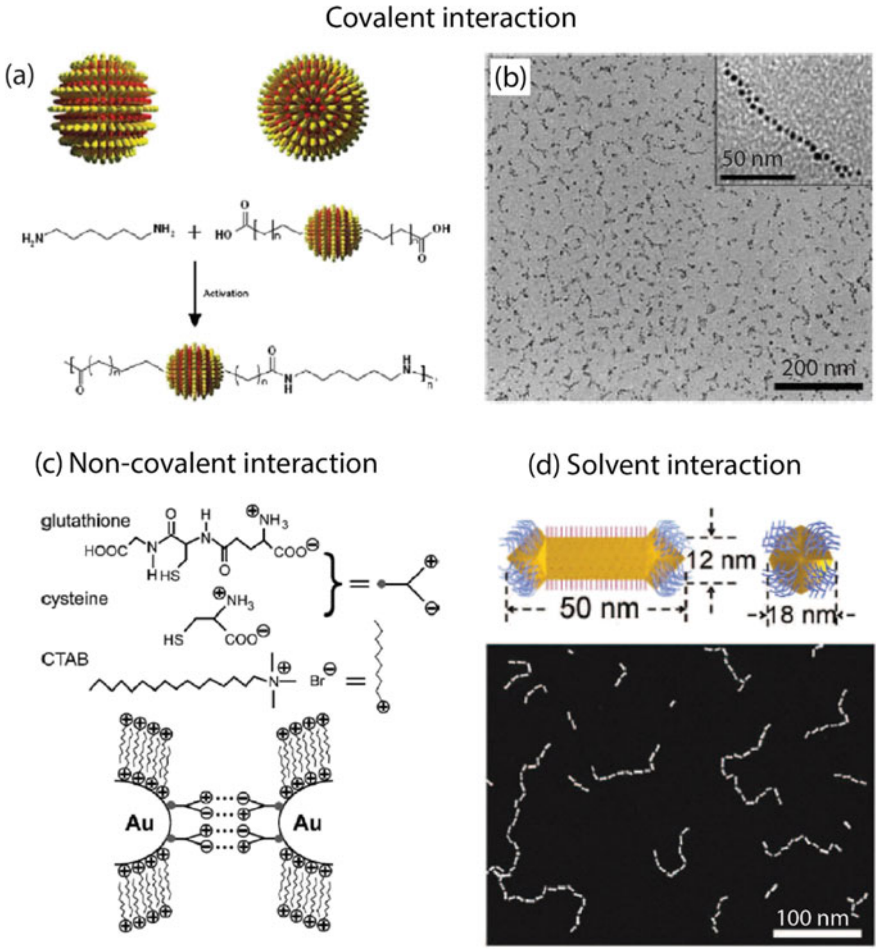

Fig. 2.4 **a** Scheme and **b** TEM images of linear chain of Au nanocrystals formation through covalent interaction (amide bond) [41]. **c** Schematic assembly mechanism using glutathione, cysteine and CTAB *via* non-covalent interaction (electrostatic forces) [44]. **d** The growth of colloidal polymer chains where the nanorods carrying CTAB (hydrophilic) on the long side and thiol-terminated polystyrene (hydrophobic) molecules on the ends [45]. Figure **a**, **b** reprinted from Ref. [41], with permission from The American Association for the Advancement of Science, Copyright 2007, **c** reprinted from Ref. [44], with permission from Royal Society of Chemistry, Copyright 2007, **d** reprinted from Ref. [45], with permission from The American Association for the Advancement of Science, Copyright 2010

2.3 Characterization Techniques for the Charge Transfer Plasmon Mode

A number of methods have been developed to characterize and study the plasmon-induced quantum tunneling phenomenon between closely-spaced metal nanostructures. The ultimate goal of plasmonics is to manipulate surface plasmons at the nanoscale, and complicated technologies have been used to characterize plasmons in detail. Here, we review the recent characterization techniques that have been in attempts to demonstrate quantum tunneling in plasmonics. Generally, they can be classified into two categories: (i) far-field optics (ii) near-field spectroscopy.

2.3.1 Far-Field Optical Characterization

The most traditional and economic way to measure the plasmonic response of metal nanostructures is collecting the absorption or extinction spectrum by using the UV-Vis NIR spectrometer [53]. Metal nanostructures exhibit a strong signal at their localized surface plasmon resonance frequencies. This can be done for nanostructures in suspension to examine the shapes, sizes, uniformity, etc. of the nanostructure morphologies. However, to study the quantum tunneling effect, dried nanostructures on well-dispersed substrates are much more practical study objects than NP suspensions. Thus, dark-field scattering microscopy coupled with UV-Vis spectrometry has been used. The scattering spectrum changes as a function of incident light polarization, wavelength, and dielectric environment.

Kern et al. [57] studied the white-light scattering spectra of side-by-side aligned nanorod dimers followed by the gap characterization in scanning electron microscopy (SEM). They reported that a peak at 800 meV corresponds to the symmetric and antisymmetric dimer modes due to the presence of atomically confined and resonantly enhanced optical fields in the gap. The energy splitting of each mode is a measure of coupling strength which depends on the gap width and refractive index of the material inside the gap. Without any means of controlling the gap width (simply drop-casting as shown in Fig. 2.5a, b), various geometries of the assembly products can be expected.

Lassiter et al. [58] reported an optical study of 1,9-nonanedithiolates SAMs functionalized gold nanoshell dimers (Fig. 2.5c) and fused dimers (coined as “nanopeanuts” in Fig. 2.5d) with dark-field micro-spectroscopy. At close distances (1.0–1.5 nm), hybridized plasmon modes appear whose energies are extremely sensitively to the presence of a small number of molecules in the interparticle junction. When touching, a new plasmon mode arises from charge transfer via conduction, as the particles are in electrical contact and charge oscillates over the whole length of the fused double-particle system.

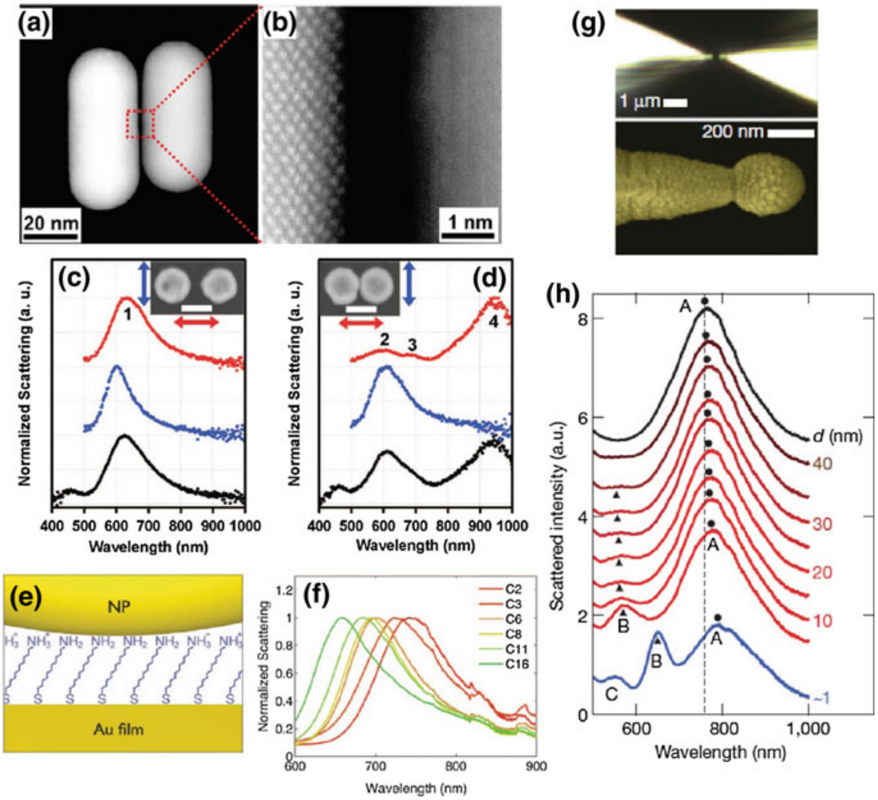

Fig. 2.5 **a** STEM image and **b** zoom in gap region of a nanorod dimer [57]. Normalized scattering spectra of a nanoshell dimer **c** from non-touching to **d** touching region. (black spectra: unpolarised illumination; blue and red: polarization arrows of the same colours in the insets) [58]. **e** Schematic of nanoparticle film separated by an amine-terminated alkanethiolates SAM. **f** The corresponding normalized dark-field measured spectra for films with SAM spacer layers of different carbon numbers [59]. **g** Dark-field microscopy image of the gap consisted of two AFM-tips, SEM image of the ball-type tip and **h** measured scattering spectra at different distances between two tips [17]. Figure **a**, **b** reprinted from Ref. [57], with permission from American Chemical Society, Copyright 2012, **c**, **d** reprinted from Ref. [58], with permission from American Chemical Society, Copyright 2008, **e**, **f** reprinted from Ref. [59], with permission from The American Association for the Advancement of Science, Copyright 2012, **g**, **h** reprinted from Ref. [17], with permission from Nature Publishing Group, Copyright 2012

Yang et al. [60] studied the Rayleigh scattering spectra of silver nanospheres dimers with diameters of 41.0 ± 4.6 nm, self-assembled with a rational DNA programmed procedure to form gaps ranging from 1 to 25 nm. For larger gaps, the plasmon resonance energy (E_{res}) red-shifts continuously with decreasing center-to-center distance (L) until the L-to-diameter (D) ratio reaches a value of $L/D \approx 1.05$. For small gaps, E_{res} does not further red-shift; but the measured resonance energies become broadly distributed. Overall, they concluded that the spectral response of nearly touching dimers does not continue to intensify with decreasing gap sizes. This is not conclusive evidence for the occurrence of tunneling, as these gap sizes are still not considered small enough to observe significant quantum tunneling.

Ciracì and co-workers [59] demonstrated the use of SAMs of amine-terminated alkanethiolates to control the gap between the Au NP and gold film in order to study the field enhancements of this metal support surface plasmons (Fig. 2.5e). The optical scattering of the Au NPs spaced a few angstroms from a gold film is studied. The plasmon resonant scattering spectra for each sample, corresponds to different gap sizes as determined by the chain length of SAMs. Ellipsometry results further support the statement that the gap could be precisely controlled by the spacers of SAMs. When the NPs were brought closer to the film, coupling between NP and film induced a red-shift in the plasmon resonance wavelength (Fig. 2.5f). They compared the experimental results with a hydrodynamic theoretical model, and concluded that non-local effects are dominant where the electric permittivity of the spacer layer must be taken into account.

Savage et al. [17] also reported observing the quantum tunneling effect by placing two AFM tips at sub-nm distances ($\sim$0.3 nm) by piezoelectric actuation stages as shown in Fig. 2.5g, followed by plasmon excitation with a laser, while the scattered light was collected and filtered to suppress background signal. They investigated three interaction regimes: capacitive near-field coupling ($50\ \text{nm} > d > 1\ \text{nm}$), the quantum regime ($1\ \text{nm} > d > 0\ \text{nm}$), and physical contact with conductive coupling ($d < 0$ nm). They found that when the separation between two nanostructures reduces below a critical size, the plasmon interactions enter the quantum regime, thereby showing a blue-shift of the resonances (Fig. 2.5h). They attribute this observation to the screening of localized surface charges by quantum tunneling and a consequent reduction in plasmonic coupling. However, their imaging technique could not confirm the proposed gap sizes and therefore the conclusive evidence of plasmon-induced quantum tunneling remains incomplete.

2.3.2 *Near-Field Spectroscopy of Plasmons*

Near-field techniques such as scanning near-field optical spectroscopy (SNOM) [56] can offer better spatial resolution than traditional optical microscopy. Unlike far-field techniques, SNOM scans the surface with a metal-coated optical probe that can detect evanescent waves, i.e., plasmons. However, the resolution is limited by the size of the probe that could offer the best resolution of $\sim$20 nm. Other near-field techniques are provided by TEM-based spectroscopy, especially EELS and cathodoluminescence. The probe in these techniques is a converged beam of electrons, typically a nanometer or so in diameter, which can be placed with sub-nanometer accuracy at any location to excite surface plasmons. The advantage of all near-field techniques is the ease of probing single particles or single dimers, which is more difficult to achieve with far-field techniques that typically measure the response of large assemblies of nanostructures.

To conclusively study the gap sizes and the quantum tunneling effect, electron beam imaging and spectroscopy are a step forward, as they will provide much better resolution than photon-based probes. Besides the ability to perform local spectroscopy, it is also possible to perform direct sub-nanometer imaging at the same location. Using a scanning transmission electron microscope (STEM) and simultaneous EELS, Duan et al. [19] observed the gradual evolution of the bonding dipole plasmon (BDP) between pairs of nanoprisms separated by gaps down to 0.5 nm and also pairs connected by conductive bridges of >3 nm in width, as shown in Fig. 2.6c, d. Scholl et al. [18] reported the observation of unusual quantum phenomena for the BDP mode for silver nanosphere dimers from 3 nm

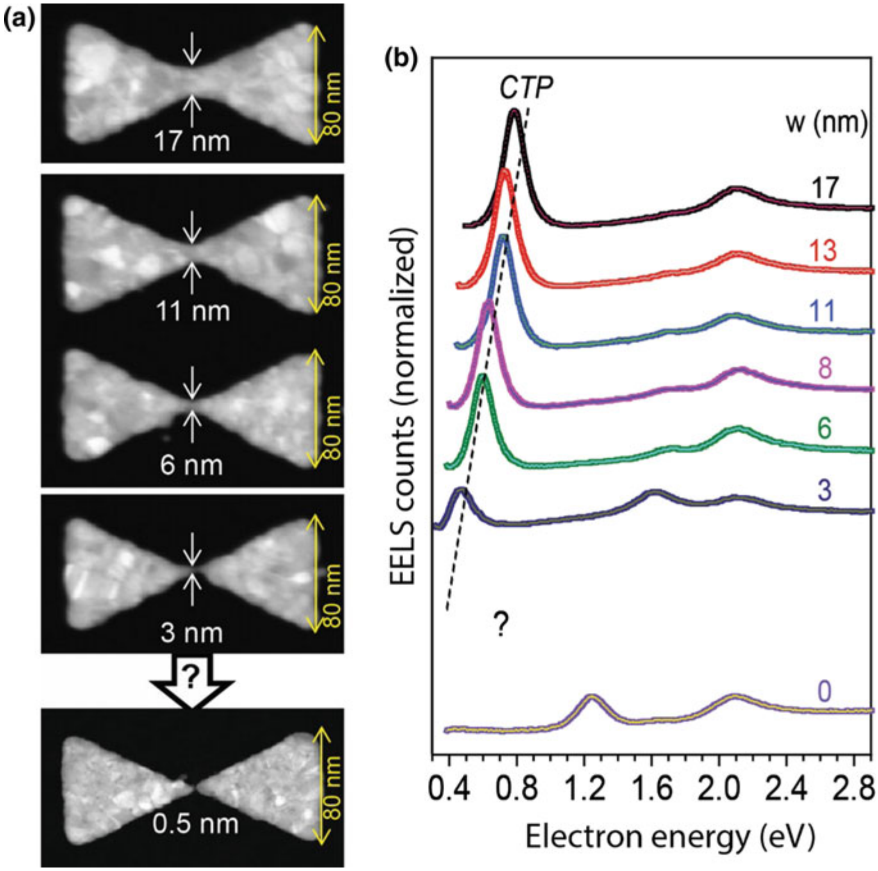

Fig. 2.6 **a** STEM images and **b** corresponding EELS spectra of gold nanoprisms pairs with different bridge and gap sizes [19]. Figure **a**, **b** reprinted from Ref. [19], with permission from American Chemical Society, Copyright 2012

separation to 8 nm wide bridges by using a STEM probe and simultaneous EELS measurements (Fig. 2.2c). For both studies, the tunneling cross sections (the surface areas that define the gap in the case of spheres and prisms) are not large enough, so the tunneling charge transfer plasmon mode still remains elusive, as manifested by the absence of the low-energy resonance (tunneling charge transfer mode) around 0.4–1.0 eV in these experiments for structures separated by a gap.

2.4 Stability of the Metal Nanoparticles Against Electron Beam Irradiation

The characterization of NPs often involves the utilization of TEM or SEM-based techniques, but these techniques are based on high-energy electron beams which may cause (un)wanted changes to the specimen such as structural degradation, radiolysis of surface molecules, contamination build-up, electron-induced atomic displacements, or heating. Here, we review the mechanisms of electron beam-induced damage on functionalized metal NPs and dimers.

2.4.1 Electron Beam-Induced Damage

Electron beam-induced damage comes in many forms, such as electron-nucleus scattering, which has been identified to produce electrostatic charging. Atomic displacement ("knock-on" effect) and electron beam sputtering of the TEM specimen are examples of such electron-nucleus interactions. On the other hand, inelastic scattering of the electron can cause specimen heating, ionization damage (radiolysis), hydrocarbon contamination, and electrostatic charging effect as well [61].

1. Knock-on effect (atomic displacement)

If the incident electron energy, E (in eV) exceeds some displacement energy, E_d (dependent on bond strength, crystal lattice and atomic weight of the constituent atoms), atomic nuclei can be displaced to interstitial positions and thereby degrading the crystalline order. This damage is predominant in conducting specimens such as metals. The degree of damage is dependent on the TEM accelerating voltage [62]. The E_d values are very much lower than the TEM accelerating voltages, so knock-on damage will always occur to certain degree (Table 2.1).

2. Electrostatic charging

The net charge added to the specimen per second depends on backscattering coefficient and the yield for the emission of secondary electrons. The charge repulsion between the beam and the charged sample can cause a mechanical force [61] that the specimen is unable to withstand, e.g., tearing of polymer films, dislodging of particles, and sample vibrations.

Table 2.1 Displacement energy (E_d); and the corresponding threshold value of incident energy (E_0), for some common materials. Adapted from Hobbs et al. [63]

Materials	E_d (eV)	E_0 (keV)
Graphite	30	140
Diamond	80	330
Aluminium	17	180
Copper	20	420
Gold	34	1320

3. Electron beam sputtering

If high-angle scattering occurs at an atom which lies at the surface of a specimen, the energy, E_s required for displacement is relatively low; surface atoms do not have to be squeezed into an interstitial site, they are free to leave the specimen and enter the vacuum of the microscope. In addition, they are bound less tightly as the number of bonds to neighbouring atoms is low (i.e., low coordination number) at the surface. This is dependent on incident direction in a high angle collision and only happens at the beam-exit surface. Light and medium-Z atoms appear to be vulnerable to sputtering by 200 keV electrons [61].

4. Electron beam heating

Energy transferred during inelastic scattering can turn into X-rays, UV or visible radiation; it may also end up as heat within the specimen. Heat loss occurs through thermal conduction and radiation. It is found that the heating is independent of specimen thickness and also insensitive to beam diameter [61]. Li et al. [64] reported that the temperature rise in an organic specimen can reach a few hundred degrees for a stationary probe. However, the temperature could easily go down by a factor of ten if the beam is scanned at video rate.

5. Ionization damage (radiolysis)

Electron beam degradation occurs when the specimen undergoes loss of crystallinity or mass loss. This damage arises from the inelastic scattering of the incident electrons and is predominant for insulating specimens [62]. Examples of known beam-sensitive materials are alkali halides, oxides, and transition metal oxides. Chemical bonds of organic materials are broken, molecule changes in shape, shift in position and loss of crystallinity. This damage can be distinguished from knock-on damage in terms of incident energy, E and temperature dependence, T. The electron dose required to create damage, D_c for radiolysis increases with E and decreases with T while for knock-on effect, D_c decreases with E and varies little with T [62].

6. Hydrocarbon contamination

This leads to mass gain as hydrocarbon molecules on the sample surface are polymerized by electrons, this polymer has low vapour pressure and surface mobility so the thickness is increased during irradiation. Diffusion of hydrocarbons along the specimen surface is the main source of most hydrocarbon contamination. The specimen itself is the local source of hydrocarbons; to minimize this effect, organic residues on the samples should therefore be minimized. This can be done by plasma cleaning, heating to desorb hydrocarbons, cooling the specimen to reduce their mobility, or for samples made from particle suspensions by washing the suspension well.

Among the effects mentioned above, the knock-on damage and the ionization damage are critical for organic monolayer-coated inorganic NPs. Knock-on effects usually occur in conducting inorganic specimen [62] where the accelerating voltage of the incident electron beam is higher than the displacement energy of the material or the electron dose exceeds about 1000 C cm^{-2}. On the other hand, the ionization damage is predominant for insulators such as organic monolayer molecules at all commonly used SEM and TEM beam energies (5–300 keV).

2.4.2 Sintering Mechanisms for Dimers or Clusters of Nanoparticles

When two NPs are separated by a narrow gap of 1–2 nm, sintering is dominant when the NP atoms diffuse across the boundaries of the particles, fusing the particles together resulting in one solid piece. Chen et al. [65] reported two kinds of sintering mechanisms (Fig. 2.7a, b). (1) Ostwald ripening, where the metal atoms leave a metal particle, diffuse over the sample support and attach to another metal particle. (2) Surface diffusion, where the particles diffuse across the metal surface and collide with other particles, leading to the formation of neck like structures bridging adjacent particles, driven by the large surface tension resulting from the small particle size. Moreover, the sintering behaviour of bare metal particles is dependent on size while for passivated particles, it is dependent on the stability of ligands to the electron beam. Larger passivated particles will have a larger electron scattering cross section (σ) which could enhance electron-material interaction, much more efficient for ligands removal, therefore lower dose is needed to produce sintering than small non-passivated particles.

In addition, surface diffusion between two metal NPs with narrow gaps of 1–2 nm has also been reported [18, 66–68]. Flüeli and co-workers [68] reported that the intense incident electron beam (20 A cm^{-2} at 300 kV) would favour the coalescence of the particles. The presence of stacking faults and other structural defects in the newly formed crystal were first observed and subsequently a neck was formed between particles. The sintering process was further enhanced by the migration of surface atoms which partly took place via the carbon substrate. The initial relative orientation of the particles was also a determining factor for the rapid sintering process.

Lim et al. [66] reported a real-time TEM study of the coalescence of individual pairs of decahedral gold NPs. They observed the rate of growth of the neck that joins two particles during coalescence and compare this to classical continuum

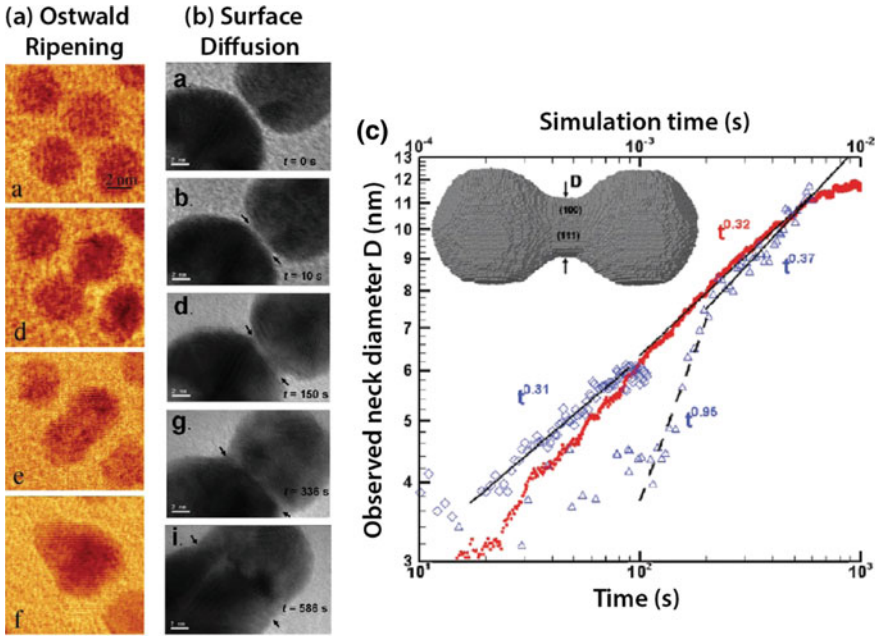

Fig. 2.7 Two sintering processes: **a** Ostwald ripening [65]. **b** Surface diffusion induced neck formation and **c** the evolution of size as a function of time [66]. Figure **a** reprinted from Ref. [65], with permission from American Chemical Society, Copyright 2006, **b**, **c** reprinted from Ref. [66], with permission from American Chemical Society, Copyright 2009

theory and to atomistic kinetic Monte Carlo simulations as shown in Fig. 2.7c. The authors attributed the disagreement between the observed results and classical continuum model to the faceted nature of the particles. Observations of spatially isolated pairs of NPs have revealed a late-stage neck growth process with characteristic power law of $D \sim t^{0.31\text{–}0.37}$, which differs substantially from the relationship $D \sim t^{0.16}$ predicted by the classical continuum theory.

Surrey et al. [67] reported quantitative measurements of surface self-diffusion. They indicated that the observed motion is due to the diffusion of the gold atoms at steps and edges of the particle surface. Impressively, they recorded the whole self-diffusion process at the atomic scale using aberration-corrected high resolution transmission electron microscopy (HRTEM). They also estimated the diffusion coefficient by measuring the fluctuation of the atom column occupation at the surface of a gold NP. The estimated diffusion coefficient was found to be $D = 10^{-17}$ to 10^{-16} cm^2/s for both gold icosahedra and truncated octahedra.

Scholl et al. [18] demonstrated the use of the electron beam to induce motion of the particles along a substrate, following earlier work by Batson et al. [69], which allowed the controlled convergence and coalescence of particles. They attributed the cause of the movement to (1) the electron beam-facilitated surface diffusion of the NPs' atoms and (2) NP polarization due to the passing electron's electric field. If the polarizations of the individual particles of a dimer become aligned, an attractive Coulombic force can be generated between them.

2.4.3 Strategies to Control Damage Caused by Electron Beam

To minimize the radiation damage caused by the electron beam, many strategies have been proposed. For instance, low-energy or low-dose imaging techniques [70], specimen cooling with liquid nitrogen [71] or specimen coating [72, 73] have been adopted to reduce the radiation damage. Specifically, ionization damage could be reduced by lowering the specimen temperature by reducing the atomic mobility [71, 74, 75] while lowering the incident beam energy and electron dose could minimize the knock-on effect [76, 77].

In addition, specimen coating with carbon [72, 73, 78] has also been demonstrated to show the protective effect where the coating acts as a diffusion barrier, reducing the escape rate for light gaseous elements. For inorganic materials, the coating not only reduces the rate of desorption-induced electronic transitions (DIET) [79] but also reduces the electrostatic charging effect [72]. Although this method is able to reduce the radiation damage, it also causes another problem of hydrocarbon contamination [61] where the hydrocarbon molecules on the specimen surface for a coating that gets thicker while irradiation proceeds. This makes the characterization of NPs by the electron beam much more difficult as much of the transmitted electron signal is absorbed or elastically scattered.

2.5 Chemical Reactivity with Other Metal Ions in Solution

Real-time visualization of chemical reactions at the nanoscale is a key challenge in the field of wet synthetic NP synthesis. A popular method to investigate the reaction kinetics is to stop the reaction at various stages and image the intermediate reaction products by TEM. This approach yields detailed information about the structure of the (intermediate) reaction products, but early stages of the reaction, or fast reactions (on the order minutes or less), cannot be investigated. In addition, the effects of sample preparation—treating the suspension with other solvents followed by centrifugation and drop casting of a small volume of the reaction mixture on the TEM grid following by removal of the solvents and associated changes in the concentrations (and the reaction kinetics) during evaporation—are not known.

2.5.1 Introduction to Liquid-Cell Electron Microscopy (LC-EM)

In situ electron microscopy with liquid-cell (LC) is an emerging technique for elucidating the mechanisms of nanostructure formation [80–82]. The first electrochemical LC as shown in Fig. 2.8a was introduced by Williamson et al. [83] in the year of 2003. However, the resolution was limited by the large total sample thickness (100 nm of each SiN membrane, 50 nm gold electrode and liquid thickness > 1 µm), the best resolution achieved was 5 nm. Zheng et al. [81] pushed the membrane thickness to 25 nm (Fig. 2.8b) in the year of 2009 so as to study the platinum (Pt) NP growth with sub-nm resolution in LC TEM.

In the same year, de Jonge et al. [84] described the use of the flow cell (Fig. 2.8c) to image whole biological cells in liquids with a constant flow of a buffer solution. This capability made it possible to study the reactions involving mixing of solvents or injecting reactants. Nonetheless, critical issues still need to be addressed, such as sample drift introduced by the liquid flow, membrane rupture, contamination, etc.

With the development of *in situ* liquid-cell (LC) electron microscopy and microfluidic devices, real-time high-resolution TEM/STEM imaging of processes in liquids was made possible. Many dynamic processes have been reported so far, such as the synthesis of colloidal NPs of different shapes, e.g., nanospheres [81, 85, 86], nanocubes [87], and nanorods [88], electrochemical deposition [83], self-assembly

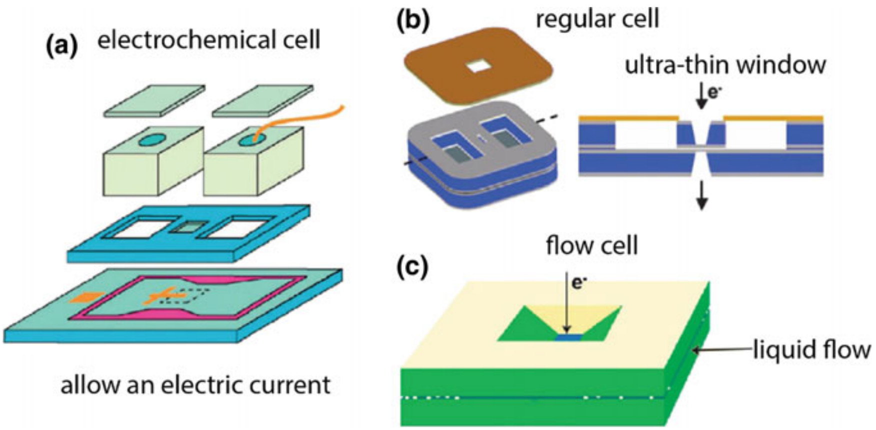

Fig. 2.8 Schematic of an assembled liquid-cell. **a** Electrochemical cell [83], **b** regular cell [81] and **c** flow cell [84]. Figure **a** reprinted from Ref. [83], with permission from Nature Publishing Group, Copyright 2003, **b** reprinted from Ref. [81], with permission from The American Association for the Advancement of Science, Copyright 2009, **c** reprinted from Ref. [84], with permission from PNAS, Copyright 2009

of NPs [89, 90] biological processes [84, 91], and NP dynamics [92]. Here, we summarize the recent progress in metal NPs synthesis using LC TEM.

1. Growth mechanisms

Zheng et al. [81] compared growth by NP coalescence with that by monomer attachment side-by-side within the same field of view (Fig. 2.9a). It is very interesting that two types of growth mechanisms reached the same particle size of the final product (Fig. 2.9b). It showed that the coalesced NP experienced recrystallization and shape re-arrangement, which prevented additional Pt atoms from attaching to the NP. So, a pause during growth was observed after a coalescence event, which allowed the NP by monomer attachment to catch up. Kraus et al. [93] reported that the dendritic nucleation was induced by the electron beam which led to an initial burst of growth as shown in Fig. 2.9c. They studied the growth rate of the tip and concluded that the dendritic growth at this scale is limited by diffusion.

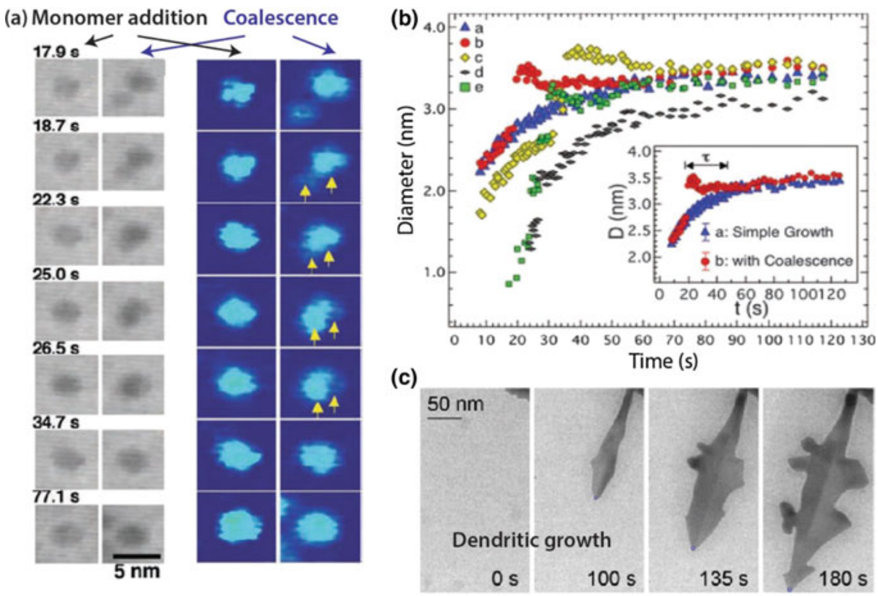

Fig. 2.9 **a** Time-lapsed TEM images (left column) and false colour enlarged (1.5 times) images (right column) for Pt nanoparticles growth by means of monomer addition and coalescence. **b** Evolution of particle size as a function of time for two types of growth means [81]. **c** Time-lapsed TEM images indicating the growth of Au dendrites [93]. Figure **a**, **b** reprinted from Ref. [81], with permission from The American Association for the Advancement of Science, Copyright 2009, **c** reprinted from Ref. [93], with permission from American Chemical Society, Copyright 2013

2. Shape control mechanisms and the role of surfactants

Many factors such as the concentration of the precursors, temperature, surfactants, etc. would affect the chemical potential of crystallization, thereby determining the final shape of the particles formed. Liao et al. [94] reported the role of the surfactant (oleylamine) on the shape evolution of platinum iron (Pt_3Fe) NPs (Fig. 2.10a). They claimed the prominence of the dipolar interactions between NPs where the NPs are stabilized without breaking down. They also attributed this to the steric hindrance effect. Jungjohann et al. [95] showed Pd growth in dilute Pd salt solution on Au seeds resulting in the formation of core-shell NPs as demonstrated in Fig. 2.10b–g. They showed that the size and shape of the Au seeds determine the morphology of the Pd shells via preferential Pd incorporation in low-coordination sites and avoidance of extended facets. The growth was limited by the ion diffusion in the solution. Recently, Liao et al. [87] further reported the growth of Pt nanocubes in a LC using TEM with high spatial and temporal resolution. Time-lapsed images are shown in Fig. 2.10h. They studied the growth rate of all facets and found that for all low index facets the growth rates are similar until the {100} facets stop growing while the other facets continue to grow to finally lead to the formation of a nanocube. This study is supported by calculations which show that the much lower ligand mobility on the {100} facets is responsible for arresting the growth of the {100} facets.

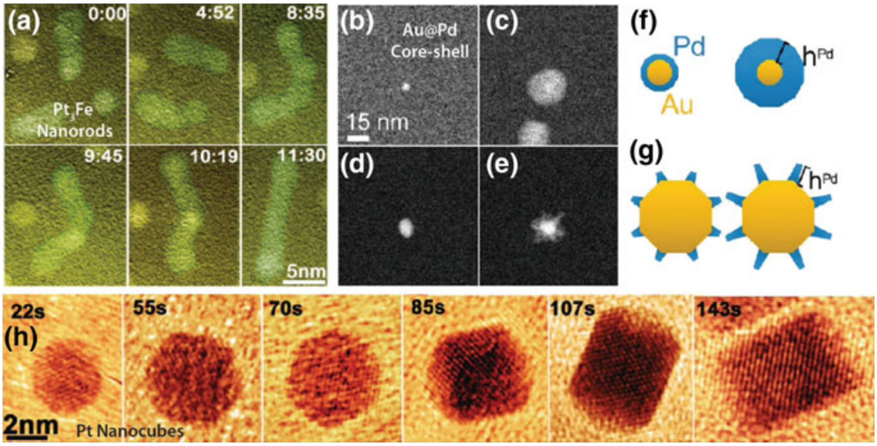

Fig. 2.10 **a** The formation of twisted Pt_3Fe nanorods and the subsequent straightening process [88]. **b**–**g** Comparison of Pd growth on **b** 5 and **d** 15 nm Au seeds and **c**, **e** their corresponding Au–Pd core-shell nanostructures. The schematic in **f**, **g** illustrate the final morphologies of the two sizes Au seeds [95]. **h** Sequential high-resolution TEM images showing the growth of a single Pt nanocube [87]. Figure **a** reprinted from Ref. [88], with permission from the American Association for the Advancement of Science, Copyright 2012, **b**–**g** reprinted from Ref. [95], with permission from American Chemical Society, Copyright 2013, **h** reprinted from Ref. [87] with permission from The American Association for the Advancement of Science, Copyright 2014

3. High resolution imaging using graphene liquid-cells (GLCs)

The graphene liquid-cell (GLC) as shown in Fig. 2.11a, b has enabled the study of colloidal nanocrystal growth with excellent high resolution imaging. This is because electron scattering due to the thin membrane window can be minimized. Yuk et al. [96] used this new type of LC to explore the mechanism of Pt nanocrystal growth and discovered site-selective coalescence (Fig. 2.11c), structural reshaping after coalescence, and surface faceting along the growth trajectories. A disadvantage of GLCs is their limited size; they are typically less than 100 nm in diameter.

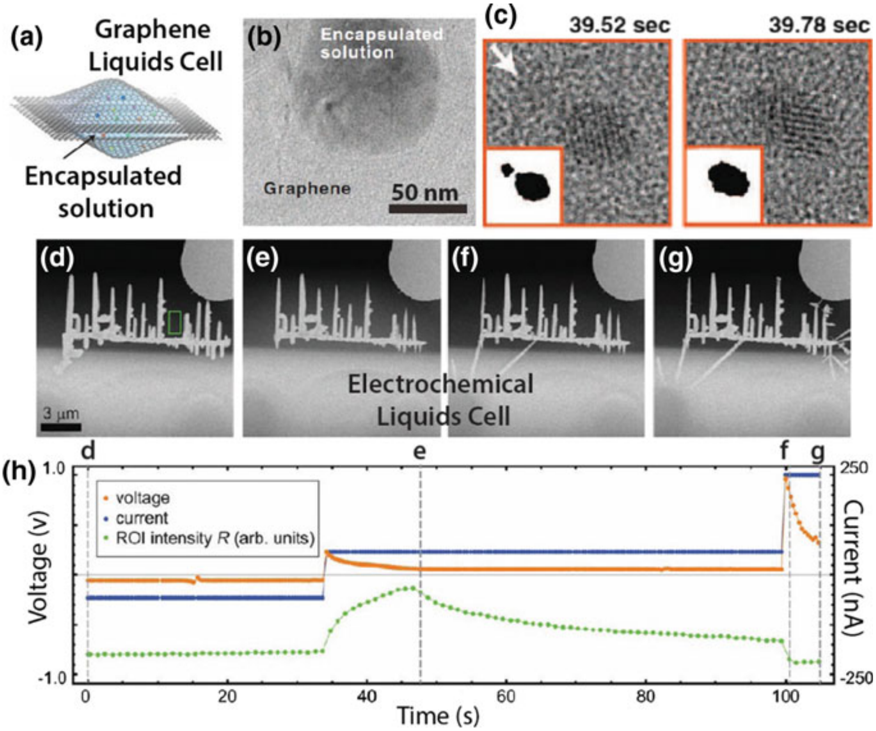

Fig. 2.11 **a** A schematic illustration of a graphene liquid-cell (GLC), encapsulating a solution. **b** TEM image of a GLC. **c** Atomic-resolution TEM imaging indicates the Pt nanocrystal growth *via* coalescence [96]. **d**–**g** Time evolution of the dendritic structure and **h** its corresponding applied electrical potential and measured electrical current. The intensity R from the ROI indicated by the green box demonstrates the sensitivity of the Pb^{2+} ions concentration to the STEM beam's sensitivity [97]. Figure **a**–**c** reprinted from Ref. [96] with permission from the American Association for the Advancement of Science, Copyright 2012, **d**–**h** reprinted from Ref. [97] with permission from American Chemical Society, Copyright 2012

4. Electrochemical liquid cells

The electrochemical deposition of metal clusters or dendritic structures has attracted a lot of attention due to its relevance to batteries and fuel cells [98]. White et al. [97] reported the electrochemical deposition of lead (Pb) from an aqueous solution of lead (II) nitrate (Fig. 2.11d–g). Both the Pb deposits and the local Pb^{2+} concentration were monitored. They used quantitative image analysis to extract the rate of Pb deposition and found that the current passed through the sample correlated well as shown in Fig. 2.11h.

5. Nanoparticle motion

Motion of NPs in growth solutions may dominated by Brownian motion, chemical reaction-induced local concentration gradient, liquid flow, electron beam effects during TEM observation, etc. Zheng et al. [99] studied the diffusion of spherical and rod-shaped gold NPs in water with 15% glycerol. It was observed that NPs show random Brownian motion plus jumps. Long distance motion due to liquid drag was also recorded. de Jonge et al. [100] used STEM to image gold NPs in several micrometer thicken films of water. White et al. [101] studied the charged Pt NP dynamics in water and Mueller et al. [102] captured the motion of gold nanorods in a flow cell. Liu et al. [90] studied the self-assembly of charged gold NPs in liquid. Park et al. [89] directly observed NP super lattice formation. Lu et al. [92] studied the dynamics of NPs in a single nanodroplet and they reported the motion is heavily damped by the strong particle-surface interactions mediated by the few atomic layers of liquids between them (Fig. 2.12a). Aabdin et al. [103] reported that the critical misalignment angle for nanocrystals (Fig. 2.12b) to merge would result in two distinct bonding pathways for two gold NPs undergoing merging process involving defect-free and defect-mediated attachment of the NPs.

6. Reduction mechanisms and electron beam effects

An electron beam not only reduces dissolved metal salt ions, but also produces bubbles in liquids, generates solvated ions/electrons and may flatten and move the studied liquid film. Thus, the reactions under electron beam irradiation can be complex and the efforts to elucidate NP growth mechanisms under electron beam irradiation are highly valuable for the understanding of nanocrystal growth in general. Woehl et al. [104] studied silver particle growth by using a flow cell and found that electron beam current played a major role in controlling the morphology of silver nanocrystals (Fig. 2.12c). It was demonstrated that under a low beam current, reaction-limited growth was preferred and nanocrystals with faceted structures were obtained. Under a higher beam current, diffusion limited growth was dominant and nanocrystals with more complex shapes were formed. Isolation of these two growth regimes showed a new level of control over nanocrystal growth under electron beam irradiation.

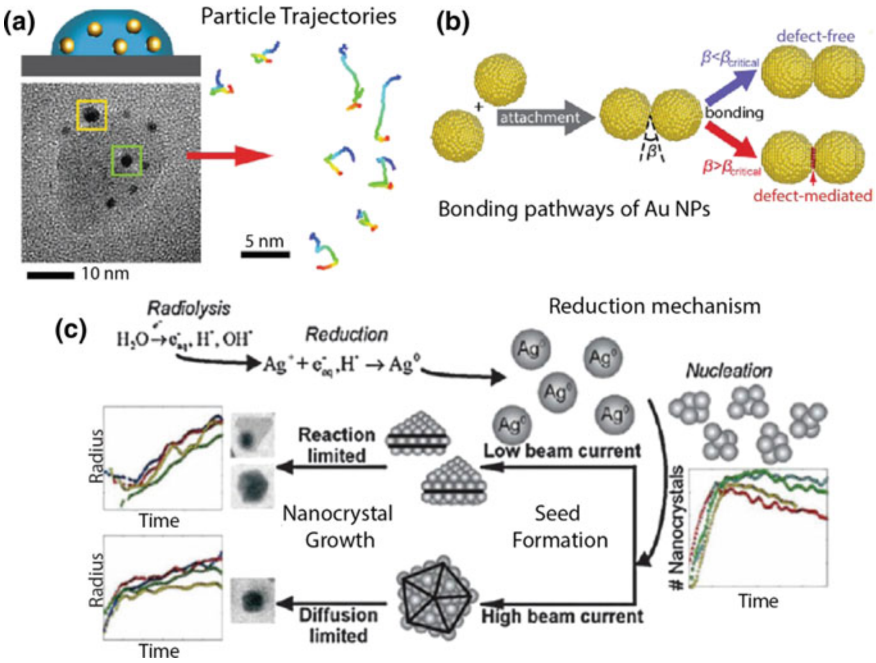

Fig. 2.12 **a** Schematic diagram and TEM image showing the motion of nanoparticles in a nanodroplet [92]. **b** Schematic illustrates the bonding pathways of two Au nanoparticles in term of critical misalignment angle [103]. **c** Schematic of beam induce growth of Ag nanoparticles [104]. Figure **a** reprinted from Ref. [92] with permission from American Chemical Society, Copyright 2014, **b** reprinted from Ref. [103] with permission from American Chemical Society, Copyright 2014, **c** reprinted from Ref. [104] with permission from American Chemical Society, Copyright 2012

2.5.2 Engineering the Gold and Silver Nanostructures via *Control of Elemental Composition*

Galvanic replacement reactions and core-shell NP formation have attracted much attention due to their versatility to generate novel metal nanostructures with tuneable and well-controlled properties. For instance, the localized surface plasmon resonances (LSPR) of Ag-Au alloy nanocages formed via a galvanic replacement reaction can be tuned across the visible regime and into the NIR [105]. The Ag–Au core-shell nanostructure exhibits one strong peak at ~500 nm wavelength together with a broad shoulder at ~400 nm [106] which is different from the Au and Ag individual particles (Au at 520 nm, Ag at 400 nm) [107].

2.5.2.1 Galvanic Replacement

Galvanic replacement reactions are used to prepare bimetallic/alloy nanostructures based in which the metal ions with higher oxidation potentials undergo reduction by oxidizing the metal present on the NP [108, 109]. Silver nanocubes are often used as sacrificial templates for galvanic replacement reactions with different oxidizing agents such as aurate ($HAuCl_4$) [109, 110], platinum (II) ions (Na_2PtCl_4) [111], palladium (II) ions (Na_2PdCl_4) [112]. In this study, we focus on the replacement of Ag with Au resulting in the formation of nanobox/hollow nanostructures composed of Au–Ag alloy single crystals. More complex structures could be generated by coupling galvanic reactions with other chemical/physical processes. For instance, Sun et al. has fabricated hollow metal nanostructures with multiple walls by coupling galvanic replacement with sequentially deposited templates where specifically single-walled Au-Ag nanoshells were first prepared via galvanic replacement, subsequently followed by reduction and another round of galvanic replacement to generate double-walled nanoshells, by repeating the cycle to produce multi-walled nanostructures [113]. While González et al. has fabricated Au–Ag double-walled nanoboxes preparation through simultaneous galvanic replacement and Kirkendall effect [114].

For galvanic replacement between Ag nanocubes and aurate, Sun et al. [115] identified three distinct steps in the reaction of silver nanostructures with chloroauric acid by *ex situ* TEM imaging (Fig. 2.13a, b): (i) pinholes form in the

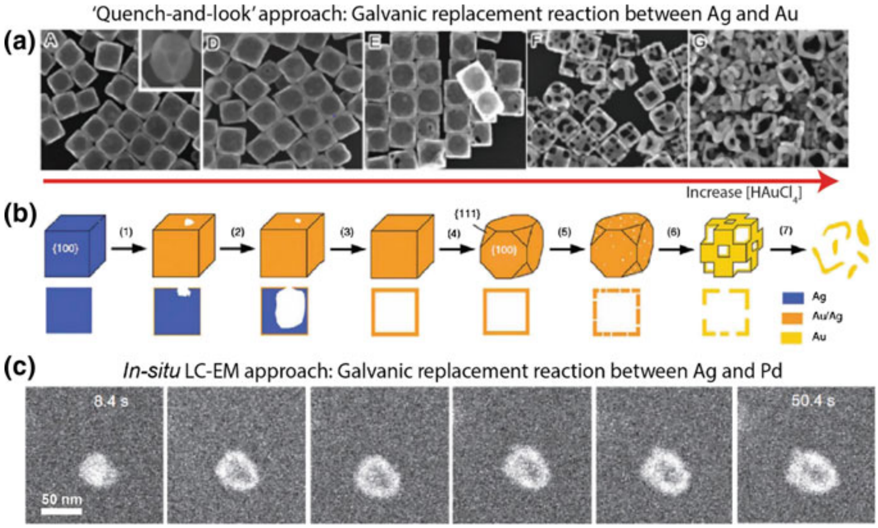

Fig. 2.13 **a** Mechanism proposed and **b** schematic based on the *ex situ* SEM observation, the so-called 'quench-and-look' approach for galvanic replacement reaction between Ag and Au [115]. **c** *In situ* liquid-cell electron microscopy (LC-EM) used for observing the galvanic replacement reaction between Ag and Pd [116]. Figure **a**, **b** reprinted from Ref. [115] with permission from American Chemical Society, Copyright 2004, **c** reprinted from Ref. [116] with permission from Nature Publishing Group, Copyright 2014

silver nanocubes via etching of the Ag by the aurate, (ii) the dissolution of silver nanocubes which also an Au–Ag alloy forms on cubes walls, and (iii) de-alloying, followed by growth of the Au layer at the expense of the Ag until finally the Au structures form.

Sun et al. [117] have also proposed that the galvanic replacement between silver nanowires and $HAuCl_4$ involves multiple steps, based on the images recorded by using *in situ* transmission X-ray microscopy (TXM) in combination with a flow cell reactor: (i) local initiation of the pitting process (ii) anisotropic etching of the silver nanowires and uniform coating of gold and (iii) reconstruction of the nanotube walls via the Ostwald ripening process. However, the spatial resolution of the TXM is rather low, 10–25 nm, relative to conventional TEM imaging which routinely achieves sub-nanometer resolution.

Sutter et al. [116] have performed *in situ* LC imaging of galvanic replacement reactions between silver NOs and $PdCl_2$ (Fig. 2.13c). They captured the transformation of solid silver NPs into hollow silver-palladium nanostructures and compared the results of *in situ* and *ex situ* preparation on the reaction rates. For *in situ* reactions, it takes 8 s to observe significant changes while the same reaction *ex situ* requires ~ 2 h. They attribute this to the presence of hydrated electrons, which are generated when the electron beam interacts with the specimen, and significantly accelerate the reaction. However, a quantification on the reaction rate is still lacking.

2.5.2.2 Core-Shell Nanostructures

Core-shell NPs are highly functionalized NPs with distinctive properties that originate from their different constituent materials. The properties of core-shell NPs can be tuned by either changing the constituting materials or the core to shell ratio [118]. This tunability makes it possible to manipulate the surface properties so as to meet the requirements for diverse applications.

The fabrication of core-shell NPs with different morphologies and compositions can be accomplished by various chemical/physical methods [119–121]. The synthesis parameters are derived empirically and the final NP morphology is confirmed with *ex situ* imaging. However, early stages of the reaction and intermediate structures cannot be investigated this way.

It is also well-known that the electron beam itself can act as a reducing agent and reduce metal ions into atoms through the action of solvated electrons (from radiolysis of water). This effect has been exploited for dynamical studies of silver [104, 122] NP nucleation directly from solution. Recently, Jungjohann et al. [95] and Wu et al. [50] demonstrated the use of *in situ* LC microscopy to study the solution growth of Au–Pd (Fig. 2.14a, b) and Pt–Au (Fig. 2.14c–e) core-shell NPs respectively. In both studies, the electron beam replaces the reducing agent, leading to metal deposition.

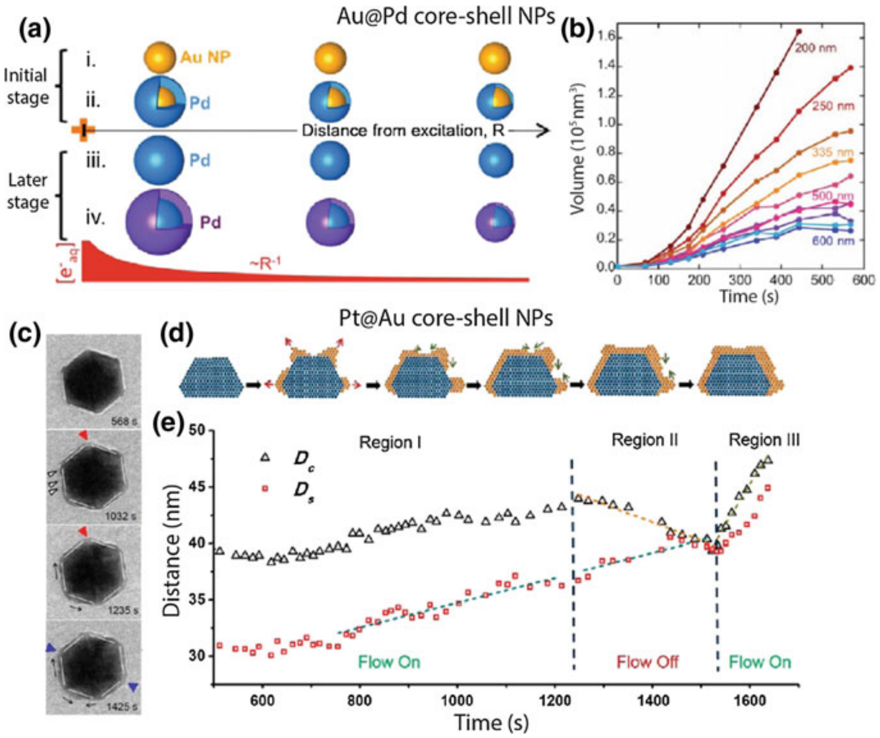

Fig. 2.14 **a** Schematic showing the growth of Pd on Au core nanoparticles in two stages. **b** The particle volume evolution as a function of time for particles at different distances from the excitation spot as indicated in (**a**) [123]. **c** Time-lapsed TEM images, **d** schematic and **e** quantitative analysis of the growth of Au on Pt icosahedron core nanoparticles [50]. Figure **a**, **b** reprinted from Ref. [123] with permission from American Chemical Society, Copyright 2014, **c**, **d** reprinted from Ref. [50] with permission from American Chemical Society, Copyright 2015

Sutter et al. [123] further demonstrated the use of *in situ* TEM to quantify the palladium deposition rate on Au NPs as a function of distance and beam currents. They reported a first-order reaction rate with respect to the concentration of hydrated electrons. The quantitative data acquisition is excellent but this study only focuses on electron beam effects and reduction mechanisms.

Fine-tuning of the structure, i.e., the dominant crystalline facets and surface composition is important for applications such as plasmonics and can be accomplished with the addition of different chemicals [119]. As such, the interplay of different chemical additives, such as surfactants and reducing agents, etc., remains largely unresolved.

2.6 Conclusions and Outlook

The ability to precisely control the structural and opto-electronic properties between two closely-spaced NPs and the understanding of the stability of the nanostructures are the keys to study quantum-plasmonic effects at sub-nanometer length scales. The level of control requires a deeper understanding of gap engineering in NP dimers and controlling their composition. Although many experimental and theoretical studies have been proposed to observe indirectly the quantum tunnelling effects, direct experimental access to the resulting tunneling charge transfer plasmon mode is still lacking. In order to achieve this, self-assembly of NPs with sub-nanometer separations by well-controlled characterization techniques is required to study plasmon-induced electron tunneling conclusively. In addition, experiments involving *in situ* liquid-cell microscopy would also provide a way to study the reaction chemistry and kinetics during the NP synthesis so as to engineer the composition of the nanostructures which is expected to open up more opportunities for application in plasmonics.

References

1. Zentgraf T, Liu Y, Mikkelsen MH, Valentine J, Zhang X. Plasmonic Luneburg and Eaton lenses. Nat Nano. 2011;6(3):151–5.
2. Liu Y, Zhang X. Metamaterials: a new frontier of science and technology. Chem Soc Rev. 2011;40(5):2494–507.
3. Wang XF, Liu RH, Gui Z, Xie YL, Yan YJ, Ying JJ, Luo XG, Chen XH. Superconductivity at 5 K in alkali-metal-doped phenanthrene. Nat Commun. 2011;2:507.
4. Fang N, Lee H, Sun C, Zhang X. Sub–diffraction-limited optical imaging with a silver superlens. Science. 2005;308(5721):534–7.
5. Kawata S, Ono A, Verma P. Subwavelength colour imaging with a metallic nanolens. Nat Photon. 2008;2(7):438–42.
6. Yuan H-K, Chettiar UK, Cai W, Kildishev AV, Boltasseva A, Drachev VP, Shalaev VM. A negative permeability material at red light. Opt Express. 2007;15(3):1076–83.
7. Shen H, Bienstman P, Maes B. Plasmonic absorption enhancement in organic solar cells with thin active layers. J Appl Phys. 2009;106(7):073109.
8. MacDonald KF, Samson ZL, Stockman MI, Zheludev NI. Ultrafast active plasmonics. Nat Photon. 2009;3(1):55–8.
9. Atwater HA, Polman A. Plasmonics for improved photovoltaic devices. Nat Mater. 2010;9 (3):205–13.
10. Ozbay E. Plasmonics: merging photonics and electronics at nanoscale dimensions. Science. 2006;311(5758):189–93.
11. Mayer KM, Hafner JH. Localized surface plasmon resonance sensors. Chem Rev. 2011;111 (6):3828–57.
12. Willets KA, Van Duyne RP. Localized surface plasmon resonance spectroscopy and sensing. Annu Rev Phys Chem. 2007;58(1):267–97.
13. Barnes WL, Dereux A, Ebbesen TW. Surface plasmon subwavelength optics. Nature. 2003;424(6950):824–30.
14. Zia R, Schuller JA, Chandran A, Brongersma ML. Plasmonics: the next chip-scale technology. Mater Today. 2006;9(7–8):20–7.

15. Esteban R, Borisov AG, Nordlander P, Aizpurua J. Bridging quantum and classical plasmonics with a quantum-corrected model. Nat Commun. 2012;3:825.
16. Wu L, Duan H, Bai P, Bosman M, Yang JKW, Li E. Fowler-Nordheim tunneling induced charge transfer plasmons between nearly touching nanoparticles. ACS Nano. 2012;7 (1):707–16.
17. Savage KJ, Hawkeye MM, Esteban R, Borisov AG, Aizpurua J, Baumberg JJ. Revealing the quantum regime in tunnelling plasmonics. Nature. 2012;491(7425):574–7.
18. Scholl JA, García-Etxarri A, Koh AL, Dionne JA. Observation of quantum tunneling between two plasmonic nanoparticles. Nano Lett. 2012;13(2):564–9.
19. Duan H, Fernández-Domínguez AI, Bosman M, Maier SA, Yang JKW. Nanoplasmonics: classical down to the nanometer scale. Nano Lett. 2012;12(3):1683–9.
20. Osberg KD, Rycenga M, Harris N, Schmucker AL, Langille MR, Schatz GC, Mirkin CA. Dispersible gold nanorod dimers with sub-5 nm gaps as local amplifiers for surface-enhanced Raman scattering. Nano Lett. 2012;12(7):3828–32.
21. Chen X, Jeon Y-M, Jang J-W, Qin L, Huo F, Wei W, Mirkin CA. On-wire lithography-generated molecule-based transport junctions: a new testbed for molecular electronics. J Am Chem Soc. 2008;130(26):8166–8.
22. Chen X, Braunschweig AB, Wiester MJ, Yeganeh S, Ratner MA, Mirkin CA. Spectroscopic tracking of molecular transport junctions generated by using click chemistry. Angew Chem Int Ed. 2009;48(28):5178–81.
23. Chen X, Yeganeh S, Qin L, Li S, Xue C, Braunschweig AB, Schatz GC, Ratner MA, Mirkin CA. Chemical fabrication of heterometallic nanogaps for molecular transport junctions. Nano Lett. 2009;9(12):3974–9.
24. Banholzer MJ, Qin L, Millstone JE, Osberg KD, Mirkin CA. On-wire lithography: synthesis, encoding and biological applications. Nat Protoc. 2009;4(6):838–48.
25. Braunschweig AB, Schmucker AL, Wei WD, Mirkin CA. Nanostructures enabled by on-wire lithography (OWL). Chem Phys Lett. 2010;486(4–6):89–98.
26. Osberg KD, Schmucker AL, Senesi AJ, Mirkin CA. One-dimensional nanorod arrays: independent control of composition, length, and interparticle spacing with nanometer precision. Nano Lett. 2011;11(2):820–4.
27. Qin L, Jang J-W, Huang L, Mirkin CA. Sub-5-nm gaps prepared by on-wire lithography: correlating gap size with electrical transport. Small. 2007;3(1):86–90.
28. Qin L, Park S, Huang L, Mirkin CA. On-wire lithography. Science. 2005;309(5731):113–5.
29. Qin L, Zou S, Xue C, Atkinson A, Schatz GC, Mirkin CA. Designing, fabricating, and imaging Raman hot spots. Proc Natl Acad Sci. 2006;103(36):13300–3.
30. Bosman M, Zhang L, Duan H, Tan SF, Nijhuis CA, Qiu CW, Yang JKW. Encapsulated annealing: enhancing the plasmon quality factor in lithographically-defined nanostructures. Sci Rep. 2014;4.
31. Broers AN, Molzen WW, Cuomo JJ, Wittels ND. Electron-beam fabrication of 80-Å metal structures. Appl Phys Lett. 1976;29(9):596–8.
32. Cord B, Yang J, Duan H, Joy DC, Klingfus J, Berggren KK. Limiting factors in sub-10 nm scanning-electron-beam lithography. J Vac Sci Technol B. 2009;27(6):2616–21.
33. Ou FS, Hu M, Naumov I, Kim A, Wu W, Bratkovsky AM, Li X, Williams RS, Li Z. Hot-spot engineering in polygonal nanofinger assemblies for surface enhanced raman spectroscopy. Nano Lett. 2011;11(6):2538–42.
34. Caswell KK, Wilson JN, Bunz UHF, Murphy CJ. Preferential end-to-end assembly of gold nanorods by biotin–streptavidin connectors. J Am Chem Soc. 2003;125(46):13914–5.
35. Henzie J, Andrews SC, Ling XY, Li Z, Yang P. Oriented assembly of polyhedral plasmonic nanoparticle clusters. Proc Natl Acad Sci. 2013;110(17):6640–5.
36. Baranov D, Manna L, Kanaras AG. Chemically induced self-assembly of spherical and anisotropic inorganic nanocrystals. J Mater Chem. 2011;21(42):16694–703.
37. Jones ST, Taylor RW, Esteban R, Abo-Hamed EK, Bomans PHH, Sommerdijk NAJM, Aizpurua J, Baumberg JJ, Scherman OA. Gold nanorods with sub-nanometer separation using cucurbit[n]uril for SERS applications. Small. 2014;10(21):4298–303.

38. Wang L, Zhu Y, Xu L, Chen W, Kuang H, Liu L, Agarwal A, Xu C, Kotov NA. Side-by-side and end-to-end gold nanorod assemblies for environmental toxin sensing. Angew Chem Int Ed. 2010;49(32):5472–5.
39. Gao B, Arya G, Tao AR. Self-orienting nanocubes for the assembly of plasmonic nanojunctions. Nat Nano. 2012;7(7):433–7.
40. Kasera S, Biedermann F, Baumberg JJ, Scherman OA, Mahajan S. Quantitative SERS using the sequestration of small molecules inside precise plasmonic nanoconstructs. Nano Lett. 2012;12(11):5924–8.
41. DeVries GA, Brunnbauer M, Hu Y, Jackson AM, Long B, Neltner BT, Uzun O, Wunsch BH, Stellacci F. Divalent metal nanoparticles. Science. 2007;315(5810):358–61.
42. Shevchenko EV, Talapin DV, Kotov NA, O'Brien S, Murray CB. Structural diversity in binary nanoparticle superlattices. Nature. 2006;439(7072):55–9.
43. Sun Z, Luo Z, Fang J. Assembling nonspherical 2d binary nanoparticle superlattices by opposite electrical charges: the role of Coulomb forces. ACS Nano. 2010;4(4):1821–8.
44. Zhang S, Kou X, Yang Z, Shi Q, Stucky GD, Sun L, Wang J, Yan C. Nanonecklaces assembled from gold rods, spheres, and bipyramids. Chem Commun. 2007;18:1816–8.
45. Liu K, Nie Z, Zhao N, Li W, Rubinstein M, Kumacheva E. Step-growth polymerization of inorganic nanoparticles. Science. 2010;329(5988):197–200.
46. Liu K, Lukach A, Sugikawa K, Chung S, Vickery J, Therien-Aubin H, Yang B, Rubinstein M, Kumacheva E. Copolymerization of metal nanoparticles: a route to colloidal plasmonic copolymers. Angew Chem. 2014;126(10):2686–91.
47. Rycenga M, McLellan JM, Xia Y. Controlling the assembly of silver nanocubes through selective functionalization of their faces. Adv Mater. 2008;20(12):2416–20.
48. Wang Y, DePrince AEK, Gray S, Lin X-M, Pelton M. Solvent-mediated end-to-end assembly of gold nanorods. J Phys Chem Lett. 2010;1(18):2692–98.
49. Fava D, Nie Z, Winnik MA, Kumacheva E. Evolution of self-assembled structures of polymer-terminated gold nanorods in selective solvents. Adv Mater. 2008;20(22):4318–22.
50. Wu J, Gao W, Wen J, Miller DJ, Lu P, Zuo J-M, Yang H. Growth of Au on Pt icosahedral nanoparticles revealed by low-dose in situ TEM. Nano Lett. 2015;15(4):2711–5.
51. Zhang Q, Li W, Moran C, Zeng J, Chen J, Wen L-P, Xia Y. Seed-mediated synthesis of Ag nanocubes with controllable edge lengths in the range of 30–200 nm and comparison of their optical properties. J Am Chem Soc. 2010;132(32):11372–8.
52. Zeng J, Zheng Y, Rycenga M, Tao J, Li Z-Y, Zhang Q, Zhu Y, Xia Y. Controlling the shapes of silver nanocrystals with different capping agents. J Am Chem Soc. 2010;132 (25):8552–3.
53. Link S, El-Sayed MA. Spectral properties and relaxation dynamics of surface plasmon electronic oscillations in gold and silver nanodots and nanorods. J Phys Chem B. 1999;103 (40):8410–26.
54. Wiley BJ, Im SH, Li Z-Y, McLellan J, Siekkinen A, Xia Y. Maneuvering the surface plasmon resonance of silver nanostructures through shape-controlled synthesis. J Phys Chem B. 2006;110(32):15666–75.
55. Zeng J, Roberts S, Xia Y. Nanocrystal-based time-temperature indicators. Chem A Eur J. 2010;16(42):12559–63.
56. Schnell M, Garcia-Etxarri A, Huber AJ, Crozier KB, Borisov A, Aizpurua J, Hillenbrand R. Amplitude- and phase-resolved near-field mapping of infrared antenna modes by transmission-mode scattering-type near-field microscopy. J Phys Chem C. 2010;114 (16):7341–5.
57. Kern J, Großmann S, Tarakina NV, Häckel T, Emmerling M, Kamp M, Huang J-S, Biagioni P, Prangsma JC, Hecht B. Atomic-scale confinement of resonant optical fields. Nano Lett. 2012;12(11):5504–9.
58. Lassiter JB, Aizpurua J, Hernandez LI, Brandl DW, Romero I, Lal S, Hafner JH, Nordlander P, Halas NJ. Close encounters between two nanoshells. Nano Lett. 2008;8 (4):1212–8.

59. Ciracì C, Hill RT, Mock JJ, Urzhumov Y, Fernández-Domínguez AI, Maier SA, Pendry JB, Chilkoti A, Smith DR. Probing the ultimate limits of plasmonic enhancement. Science. 2012;337(6098):1072–4.
60. Yang L, Wang H, Yan B, Reinhard BM. Calibration of silver plasmon rulers in the 1–25 nm separation range: experimental indications of distinct plasmon coupling regimes. J Phys Chem C. 2010;114(11):4901–8.
61. Egerton RF, Li P, Malac M. Radiation damage in the TEM and SEM. Micron. 2004;35 (6):399–409.
62. Egerton RF. Mechanisms of radiation damage in beam-sensitive specimens, for TEM accelerating voltages between 10 and 300 kV. Microsc Res Tech. 2012;75(11):1550–6.
63. Hobbs LW. Introduction to analytical electron microscopy. New York: Plenum Press; 1987.
64. Li P. Electron irradiation damage to organic light-emitting materials. Canada: University of Alberta; 2003.
65. Chen Y, Palmer RE, Wilcoxon JP. Sintering of passivated gold nanoparticles under the electron beam. Langmuir. 2006;22(6):2851–5.
66. Lim TH, McCarthy D, Hendy SC, Stevens KJ, Brown SA, Tilley RD. Real-time TEM and kinetic Monte Carlo studies of the coalescence of decahedral gold nanoparticles. ACS Nano. 2009;3(11):3809–13.
67. Surrey A, Pohl D, Schultz L, Rellinghaus B. Quantitative measurement of the surface self-diffusion on Au nanoparticles by aberration-corrected transmission electron microscopy. Nano Lett. 2012;12(12):6071–7.
68. Flüeli M, Buffat PA, Borel JP. Real time observation by high resolution electron microscopy (HREM) of the coalescence of small gold particles in the electron beam. Surf Sci. 1988;202 (1–2):343–53.
69. Batson PE, Reyes-Coronado A, Barrera RG, Rivacoba A, Echenique PM, Aizpurua J. Plasmonic nanobilliards: controlling nanoparticle movement using forces induced by swift electrons. Nano Lett. 2011;11(8):3388–93.
70. David B, Carlson JEE. Low-dose imaging techniques for transmission electron microscopy. The transmission electron microscope. InTech; 2012.
71. Egerton RF. Chemical measurements of radiation damage in organic samples at and below room temperature. Ultramicroscopy. 1980;5(1–3):521–3.
72. Salih SM, Cosslett VE. Reduction in electron irradiation damage to organic compounds by conducting coatings. Phil Mag. 1974;30(1):225–8.
73. Fryer JR, Holland F. The reduction of radiation damage in the electron microscope. Ultramicroscopy. 1983;11(1):67–70.
74. Egerton RF. Control of radiation damage in the TEM. Ultramicroscopy. 2013;127:100–8.
75. Cryoprotection in electron microscopy. J Microsc. 1986;141(3):385–91.
76. Egerton RF, McLeod R, Wang F, Malac M. Basic questions related to electron-induced sputtering in the TEM. Ultramicroscopy. 2010;110(8):991–7.
77. Isaacson MS. Principles and techniques of electron microscopy. 7th ed. New York: Van Nostrand; 1973.
78. Egerton RF, Crozier PA, Rice P. Electron energy-loss spectroscopy and chemical change. Ultramicroscopy. 1987;23(3–4):305–12.
79. Strane J, Marks LD, Luzzi DE, Buckett MI, Zhang JP, Wessels BW. Encapsulation, diffusion and diet in the electron microscope. Ultramicroscopy. 1988;25(3):253–7.
80. Mirsaidov UM, Zheng H, Bhattacharya D, Casana Y, Matsudaira P. Direct observation of stick-slip movements of water nanodroplets induced by an electron beam. Proc Natl Acad Sci. 2012;109(19):7187–90.
81. Zheng H, Smith RK, Jun Y-W, Kisielowski C, Dahmen U, Alivisatos AP. Observation of single colloidal platinum nanocrystal growth trajectories. Science. 2009;324(5932):1309–12.
82. Liao H-G, Niu K, Zheng H. Observation of growth of metal nanoparticles. Chem Commun. 2013;49(100):11720–7.
83. Williamson MJ, Tromp RM, Vereecken PM, Hull R, Ross FM. Dynamic microscopy of nanoscale cluster growth at the solid-liquid interface. Nat Mater. 2003;2(8):532–6.

84. Jonge ND, Peckys DB, Kremers GJ, Piston DW. Electron microscopy of whole cells in liquid with nanometer resolution. Proc Nat Acad Sci 2009;106(7):2159–64.
85. Parent LR, Robinson DB, Woehl TJ, Ristenpart WD, Evans JE, Browning ND, Arslan I. Direct in situ observation of nanoparticle synthesis in a liquid crystal surfactant template. ACS Nano. 2012;6(4):3589–96.
86. Evans JE, Jungjohann KL, Browning ND, Arslan I. Controlled growth of nanoparticles from solution with in situ liquid transmission electron microscopy. Nano Lett. 2011;11(7):2809–13.
87. Liao H-G, Zherebetskyy D, Xin H, Czarnik C, Ercius P, Elmlund H, Pan M, Wang L-W, Zheng H. Facet development during platinum nanocube growth. Science. 2014;345 (6199):916–9.
88. Liao H-G, Cui L, Whitelam S, Zheng H. Real-time imaging of Pt3Fe nanorod growth in solution. Science. 2012;336(6084):1011–4.
89. Park J, Zheng H, Lee WC, Geissler PL, Rabani E, Alivisatos AP. Direct observation of nanoparticle superlattice formation by using liquid cell transmission electron microscopy. ACS Nano. 2012;6(3):2078–85.
90. Liu Y, Lin X-M, Sun Y, Rajh T. In situ visualization of self-assembly of charged gold nanoparticles. J Am Chem Soc. 2013;135(10):3764–7.
91. Jonge ND, Dukes M, Kremers G, Northan B, Peckys D, Ring E, Piston D, Sougrat R. Liquid and three-dimensional scanning transmission electron microscopy for biological specimen. Microsc Microanal 2009;15(SupplementS2):686–7.
92. Lu J, Aabdin Z, Loh ND, Bhattacharya D, Mirsaidov U. Nanoparticle dynamics in a nanodroplet. Nano Lett. 2014;14(4):2111–5.
93. Kraus T, de Jonge N. Dendritic gold nanowire growth observed in liquid with transmission electron microscopy. Langmuir. 2013;29(26):8427–32.
94. Liao H-G, Zheng H. Liquid cell transmission electron microscopy study of platinum iron nanocrystal growth and shape evolution. J Am Chem Soc. 2013;135(13):5038–43.
95. Jungjohann KL, Bliznakov S, Sutter PW, Stach EA, Sutter EA. In situ liquid cell electron microscopy of the solution growth of Au–Pd core-shell nanostructures. Nano Lett. 2013;13 (6):2964–70.
96. Yuk JM, Park J, Ercius P, Kim K, Hellebusch DJ, Crommie MF, Lee JY, Zettl A, Alivisatos AP. High-resolution EM of colloidal nanocrystal growth using graphene liquid cells. Science. 2012;336(6077):61–4.
97. White ER, Singer SB, Augustyn V, Hubbard WA, Mecklenburg M, Dunn B, Regan BC. In situ transmission electron microscopy of lead dendrites and lead ions in aqueous solution. ACS Nano. 2012;6(7):6308–17.
98. Leenheer AJ, Jungjohann KL, Zavadil KR, Sullivan JP, Harris CT. Lithium electrodeposition dynamics in aprotic electrolyte observed in situ *via* transmission electron microscopy. ACS Nano. 2015;9(4):4379–89.
99. Zheng H, Claridge SA, Minor AM, Alivisatos AP, Dahmen U. Nanocrystal diffusion in a liquid thin film observed by in situ transmission electron microscopy. Nano Lett. 2009;9 (6):2460–5.
100. de Jonge N, Poirier-Demers N, Demers H, Peckys DB, Drouin D. Nanometer-resolution electron microscopy through micrometers-thick water layers. Ultramicroscopy. 2010;110 (9):1114–9.
101. White ER, Mecklenburg M, Shevitski B, Singer SB, Regan BC. Charged nanoparticle dynamics in water induced by scanning transmission electron microscopy. Langmuir. 2012;28(8):3695–8.
102. Mueller C, Harb M, Dwyer JR, Miller RJD. Nanofluidic cells with controlled pathlength and liquid flow for rapid, high-resolution in situ imaging with electrons. J Phys Chem Lett. 2013;4(14):2339–47.
103. Aabdin Z, Lu J, Zhu X, Anand U, Loh ND, Su H, Mirsaidov U. Bonding pathways of gold nanocrystals in solution. Nano Lett. 2014;14(11):6639–43.

104. Woehl TJ, Evans JE, Arslan I, Ristenpart WD, Browning ND. Direct in situ determination of the mechanisms controlling nanoparticle nucleation and growth. ACS Nano. 2012;6 (10):8599–610.
105. Skrabalak SE, Chen J, Sun Y, Lu X, Au L, Cobley CM, Xia Y. Gold nanocages: synthesis, properties, and applications. Acc Chem Res. 2008;41(12):1587–95.
106. Kahraman M, Aydın Ö, Çulha M. Oligonucleotide-mediated Au–Ag core-shell nanoparticles. Plasmonics. 2009;4(4):293–301.
107. Lim D-K, Kim I-J, Nam J-M. DNA-embedded Au/Ag core-shell nanoparticles. Chem Commun. 2008;42:5312–4.
108. Lin W, Warren TH, Nuzzo RG, Girolami GS. Surface-selective deposition of palladium and silver films from metal-organic precursors: a novel metal-organic chemical vapor deposition redox transmetalation process. J Am Chem Soc. 1993;115(24):11644–5.
109. Sun Y, Xia Y. Shape-controlled synthesis of gold and silver nanoparticles. Science. 2002;298(5601):2176–9.
110. Skrabalak SE, Au L, Li X, Xia Y. Facile synthesis of Ag nanocubes and Au nanocages. Nat Protoc. 2007;2(9):2182–90.
111. Chen J, Wiley B, McLellan J, Xiong Y, Li Z-Y, Xia Y. Optical properties of Pd–Ag and Pt–Ag nanoboxes synthesized *via* galvanic replacement reactions. Nano Lett. 2005;5(10):2058–62.
112. Cobley CM, Campbell DJ, Xia Y. Tailoring the optical and catalytic properties of gold-silver nanoboxes and nanocages by introducing palladium. Adv Mater. 2008;20(4):748–52.
113. Sun Y, Wiley B, Li Z-Y, Xia Y. Synthesis and optical properties of nanorattles and multiple-walled nanoshells/nanotubes made of metal alloys. J Am Chem Soc. 2004;126 (30):9399–406.
114. González E, Arbiol J, Puntes VF. Carving at the nanoscale: sequential galvanic exchange and kirkendall growth at room temperature. Science. 2011;334(6061):1377–80.
115. Sun Y, Xia Y. Mechanistic study on the replacement reaction between silver nanostructures and chloroauric acid in aqueous medium. J Am Chem Soc. 2004;126(12):3892–901.
116. Sutter E, Jungjohann K, Bliznakov S, Courty A, Maisonhaute E, Tenney S, Sutter P. In situ liquid-cell electron microscopy of silver–palladium galvanic replacement reactions on silver nanoparticles. Nat Commun. 2014;5.
117. Sun Y, Wang Y. Monitoring of galvanic replacement reaction between silver nanowires and HAuCl4 by in situ transmission X-ray microscopy. Nano Lett. 2011;11(10):4386–92.
118. Oldenburg SJ, Averitt RD, Westcott SL, Halas NJ. Nanoengineering of optical resonances. Chem Phys Lett. 1998;288(2–4):243–7.
119. Tsuji M, Matsuo R, Jiang P, Miyamae N, Ueyama D, Nishio M, Hikino S, Kumagae H, Kamarudin KSN, Tang X-L. Shape-dependent evolution of Au@Ag core–shell nanocrystals by PVP-assisted *N*,*N*-dimethylformamide reduction. Crys Growth Des. 2008;8(7):2528–36.
120. Ma Y, Li W, Cho EC, Li Z, Yu T, Zeng J, Xie Z, Xia Y. Au@Ag core–shell nanocubes with finely tuned and well-controlled sizes, shell thicknesses, and optical properties. ACS Nano. 2010;4(11):6725–34.
121. Gong J, Zhou F, Li Z, Tang Z. Synthesis of Au@Ag core-shell nanocubes containing varying shaped cores and their localized surface plasmon resonances. Langmuir. 2012;28 (24):8959–64.
122. Noh KW, Liu Y, Sun L, Dillon SJ. Challenges associated with in-situ TEM in environmental systems: the case of silver in aqueous solutions. Ultramicroscopy. 2012;116:34–8.
123. Sutter EA, Sutter PW. Determination of redox reaction rates and orders by in situ liquid cell electron microscopy of Pd and Au solution growth. J Am Chem Soc. 2014;136(48):16865–70.

124 Y. Sun, Shape-Controlled Synthesis of Gold and Silver Nanoparticles. Science 298 (5601):2176-2179

Chapter 3
Self-Assembly of Silver Nanoparticles with Sub-nanometer Separations

Abstract A bottom-up method was developed to fabricate structures of the form Ag-SAM-Ag (where SAM = self-assembled monolayer). Silver nanocubes with edge lengths of 30–40 nm were synthesized via established methods, with mixed SAMs of thiolates and dithiolates on their surfaces. The SAMs were used to control the self-assembly process and the width of the sub-nanometer gap sizes. The fabricated structures were characterized by various techniques: transmission electron microscopy (TEM), scanning electron microscopy (SEM), X-ray photoelectron spectroscopy (XPS), Ultraviolet photoelectron spectroscopy (UPS), and UV-visible spectroscopy (UV-Vis). It was demonstrated that the SAMs control the structure's optical properties and provide molecular-electronic control over the barrier heights of the studied system. The synthesis routines discussed here will be used in Chap. 4 to demonstrate quantum plasmonics.

3.1 Introduction

Nanostructures with tunable gap sizes are good candidates to study plasmon-induced tunneling effects [1–3] or surface-enhanced Raman spectroscopy (SERS) enhancement [4, 5]. These structures are challenging to fabricate by top-down nanofabrication techniques such as electron-beam lithography (EBL), because of resolution limitations. Additionally, top-down approaches only yield polycrystalline structures that suffer from defects and plasmon damping [6–9].

On the other hand, sub-nanometer gaps are relatively easily achievable by wet-chemical solution processing methods. Wet chemical or bottom-up approaches have been widely used for the fabrication of silver (Ag) nanoparticles (NPs) with different sizes and shapes and with high monodispersity. Despite their single-crystallinity, the atomically smooth surfaces also enable the formation of interparticle gaps with distinct and flat interfaces. Moreover, wet chemical method facilitates the production of single-crystalline defect-free Ag nanostructures with sub-nanometer gap sizes at massive scales.

S. F. Tan, *Molecular Electronic Control Over Tunneling Charge Transfer Plasmons Modes*, Springer Theses, https://doi.org/10.1007/978-981-10-8803-2_3

In this Chapter, we report a new method to prepare crystalline structures of Ag plasmonic resonators with edge lengths of 30–40 nm and with high aspect ratio nano-gaps by functionalizing the Ag nanocube surfaces with mixed self-assembled monolayers (SAMs) of thiolates and dithiolates. The SAMs were used to control the sub-nanometer gap sizes and optical properties between two Ag NPs. We characterized the functionalized NPs with transmission electron microscopy (TEM), UV-visible spectroscopy (UV-Vis), X-ray photoelectron spectroscopy (XPS), Ultraviolet photoelectron spectroscopy (UPS) and 3D scanning TEM tomography.

3.2 Results and Discussion

3.2.1 Synthesis and Functionalization of Silver Nanocubes

We used single crystalline Ag nanocubes to form dimers for three reasons. (i) These NPs can be functionalized with ligands with a length of approx. 0.5–2 nm which can direct the self-assembly of dimers and the gap size. (ii) These particles have atomically flat surfaces, resulting in defect-free nanogaps. (iii) These NPs have high aspect ratios of the nanogap that can be tuned by controlling NP size and the length of the molecule.

We followed the polyol method developed by the Xia's group to chemically synthesize the single-crystalline Ag nanocubes [10]. The experimental details of the synthetic procedures and characterization techniques are reported in the experimental section at the end of this Chapter. Here, we only give a brief description.

In this reaction, ethylene glycol acts as both solvent and reducing agent while sodium sulfide acts as the catalyst. The silver nitrate is used as the Ag precursor. The polymer, poly(vinyl)pyrrolidone (PVP) was used as a surfactants which selectively capped the {100} facets of the nanocrystals. The careful control among the ratios of these four reactants and temperature enables the formation of Ag nanocubes with PVP stabilized {100} facets.

The Ag nanocubes were functionalized with mixed self-assembled monolayers (SAMs) of thiolates and ditholates to form dimers and avoid aggregation (Fig. 3.1a). The molecules not only could act as the linkers to determine the gap sizes between two nanocubes (Fig. 3.1b, c), but also could alter the opto-electronic properties of such a Ag-SAMs-Ag plasmonic system (Fig. 3.1d).

Figure 3.1 schematically shows the modification process. First, the Ag NPs with cuboidal shapes were dispersed in freshly-distilled ethanol after washing thoroughly with water and acetone in order to get rid of the polymer residue present during NP synthesis. Subsequently, we added the mixed SAM solution to change the dielectric environment of the nanocubes. In a second step, these functionalized NPs were mixed with non-functionalized NPs to form predominantly dimeric structures.

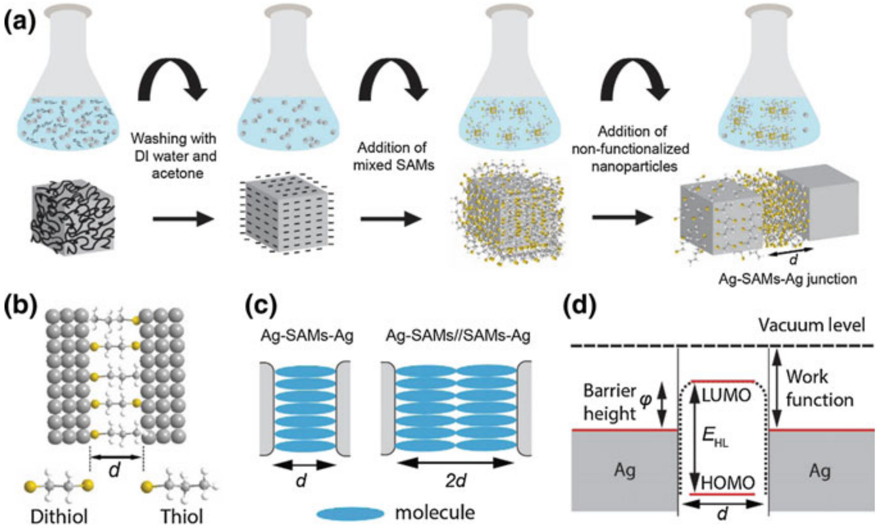

Fig. 3.1 **a** Schematic of the surface modification process. **b** The distance between two adjacent nanoparticles is determined by the thickness of the self-assembled monolayers (SAMs). **c** Two types of junctions are possible in our system. **d** A schematic energy-level diagram of the junctions

3.2.2 Transmission Electron Microscope (TEM) Gap Size Characterization

We characterized the functionalized NPs with TEM. Figure 3.2a shows a TEM overview image of the chemically-synthesized Ag nanocubes that are capped with a thick layer of PVP. The edge length of the nanocubes is about 30–40 nm. Figure 3.2b shows a TEM image and its electron diffraction pattern of a single-crystalline Ag nanocube drop-casted on 30-nm thick SiN_x membrane. The electron diffraction (inset) suggests that the Ag nanocubes were single crystalline and bounded by {100} facets. Figure 3.2c is a representative TEM overview image of the Ag nanocubes after functionalization with mixed SAMs of PT and BDT. We typically obtained 20–30% dimeric structures; the remainders were single particles, or trimeric structures or larger aggregates. Figure 3.2d shows a typical image of a dimer consisting of two Ag nanocubes aligned parallel to each other and the inset shows a high resolution scanning TEM image (STEM) of the gap region, which is about 0.8 nm wide.

To constitute the very small gaps, we performed a functionalization process to the Ag nanocubes with mixed self-assembled monolayers (SAMs) of alkanethiols and alkane/benzenedithiols with different chain lengths so that the silver-thiolate bonds would reduce the size of the nanogaps to sub-nm length scale. We define the

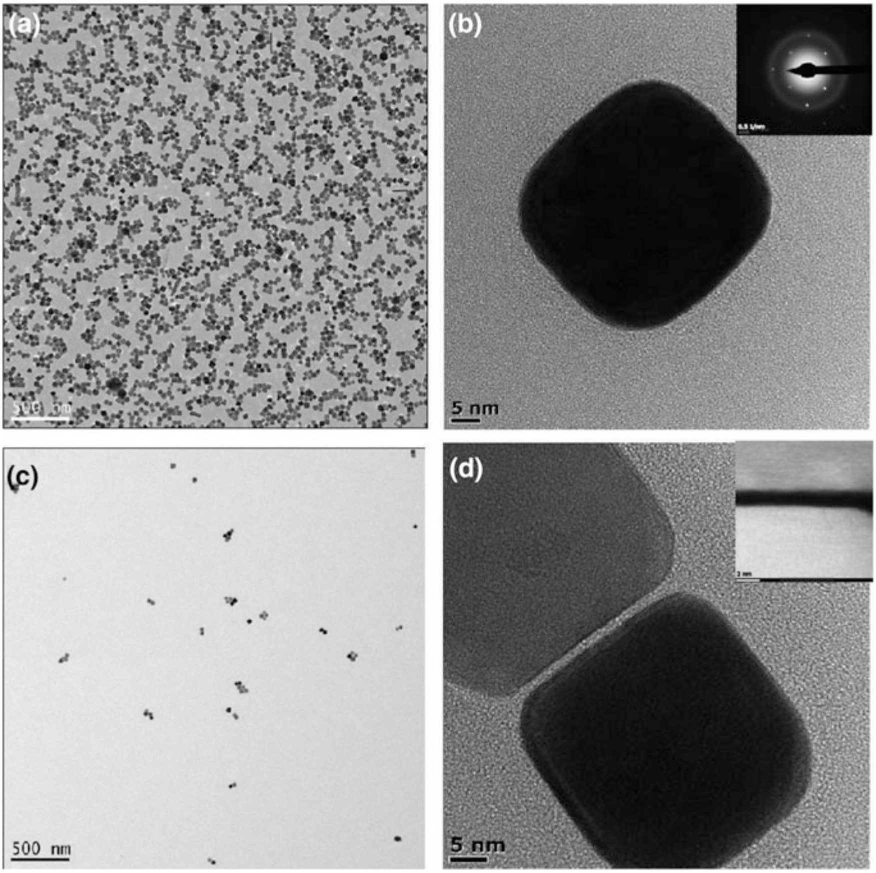

Fig. 3.2 **a** TEM overview image of chemically-synthesized silver (Ag) nanocubes. **b** TEM image and electron diffraction pattern of a single Ag nanocube (inset). **c** Representative TEM overview image of the Ag nanocubes after functionalization with mixed SAMs of PT and BDT. **d** Dimer consisting of two Ag nanocubes aligned parallel to each other and a high resolution scanning TEM image (STEM) of the gap region (inset)

nanogap as the distance between two Ag nanocube surfaces where they are parallel aligned. The length of EDT, HDT, ODT, BDT, BPDT, OPV and NDT are 0.44, 0.93, 1.17, 0.63, 1.03, 1.24 and 0.88 nm, respectively (determined using Chem 3D ultra version 10.0; see Fig. 3.3 for the molecular structures). These values are generated from the built-in parameters on bond lengths, bond angles and dihedral angles without further optimization procedures. Figure 3.3 shows that the gap sizes indeed were controlled by the molecular structure. The histograms we obtained for the nanogap sizes (d_g) show reasonable agreement where the maximum of the

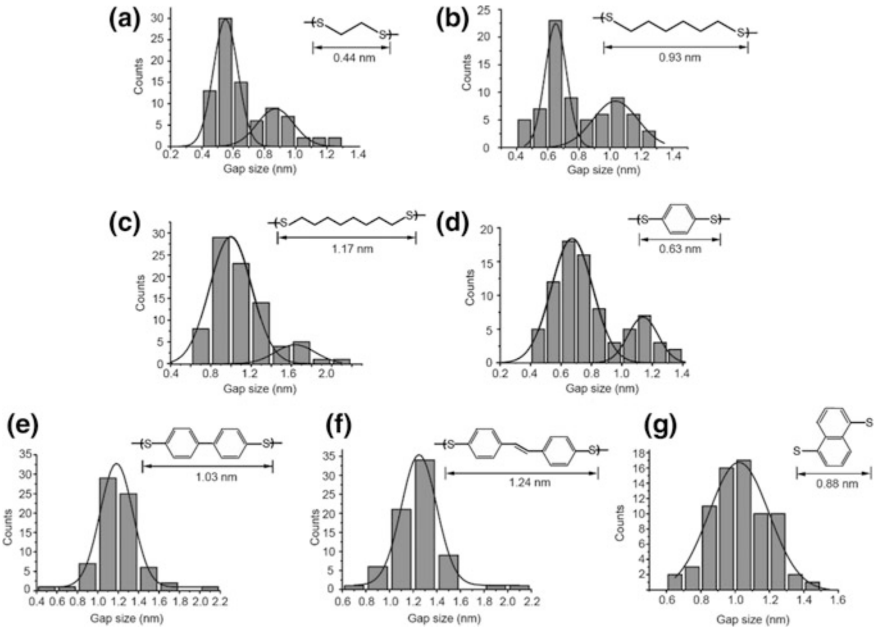

Fig. 3.3 **a** Histograms of the gap sizes between two silver nanocubes with Gaussian fits to these histograms functionalized with mixed SAMs of 1-propanethiol and 1,2-ethanedithiol (EDT), **b** with mixed SAMs of 1-heptanethiol and 1,6-hexanedithiol (HDT), **c** with mixed SAMs of 1-nonanethiol and 1,8-octanedithiol (ODT), **d** with mixed SAMs of 1-propanethiol and 1,4-benzenedithiol (BDT), **e** with SAMs of 1,4-biphenyldithiol (BPDT), **f** with SAMs of 4,4-dimercaptostilbene (OPV), **g** with SAMs of 1,5-napthalenedithiol (NDT)

Gaussian peak lies at 0.6 ± 0.1 nm for EDT, 0.7 ± 0.1 nm for HDT and BDT, 1.0 ± 0.2 nm for ODT, 1.2 ± 0.2 nm for BPDT and OPV, 1.0 ± 0.3 nm for NDT and very close to the estimated molecular lengths (d_1).

For the structures self-assembled with these mixed SAMs, we observed a significant number of dimers where each particle was covered with a SAM, resulting in a value of d that is roughly double of that expected for a junction with only a single SAM. The second peak in these histograms is attributed to dimers with SAMs on both NPs (Ag-SAM//SAM-Ag structures). Double peaks are not observed for SAMs of 1,4-biphenyldithiol (BPDT), 4,4-dimercaptostilbene (OPV) and 1,5-napthalenedithiol (NDT). These three SAMs contain biphenyl moiety which had been proven in literature [11] that the rigid character would result in a molecular dipole moment that affects the adsorption kinetics on metal surfaces. Unlike the SAMs of alkanethiolates which the packing is driven by the interchain van der Waals attraction, biphenyl derivatives molecules possess strong dipole moment, resulting in intermolecular repulsion and instability. Thus, double layers of SAMs are not observed in Fig. 3.3e–g. Figure 3.4 also shows that our experimentally measured gap sizes (aliphatic molecules: black solid squares; aromatic

Fig. 3.4 Experimentally measured gap sizes versus molecular lengths as predicted by the CPK model

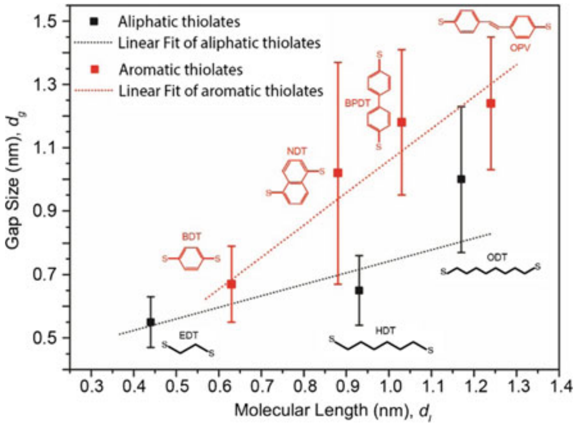

Table 3.1 Summary of Fig. 3.3: number of junctions, interparticle spacing of silver nanocubes assembled with linkers of different molecular length d_l estimated by a CPK model and the gap sizes d_g determined experimentally from TEM images

Linker	Number of junctions	Molecular length (nm), d_l	Gap size (nm), d_g
1,2-ethanedithiol (EDT)	84	0.44	0.55 ± 0.08
1,6-hexanedithiol (HDT)	73	0.93	0.65 ± 0.11
1,8-octanedithiol (ODT)	85	1.17	1.00 ± 0.23
1,4-benzendithiol (BDT)	79	0.63	0.67 ± 0.12
1,5-dimercaptonapthalene (NDT)	73	0.88	1.02 ± 0.35
1,4-biphenyldithiol (BPDT)	73	1.03	1.18 ± 0.23
4,4-dimercaptostilbene (OPV)	76	1.24	1.24 ± 0.21

molecules: red solid squares) are in good correlation with the molecular length predicted by a Corey-Pauling-Koltun (CPK) model (red and black dotted lines) (Table 3.1).

3.2.3 3D Scanning TEM Tomography

To further characterize the high aspect ratio nanogaps, 3D scanning TEM (STEM) tomography was conducted to obtain a 3-dimensional view of these nanogaps. We functionalized the Ag nanocubes with ODT (procedure as shown in the experimental section) and dropcasted ~3 µl of the final solution onto a Si_3N_4 substrate (30 nm thick, from Agar Scientific). The substrate with nanocube dimers was tilted from −50° to +50° with respect to the horizontal axis of the nanocubes dimer and a STEM image was taken at intervals of 1–3°. The series of images were aligned and a 3D volume was reconstructed from a total of 55 STEM images, as shown in Fig. 3.5. Due to the lack of projections from the high tilt angle ranges (beyond ±70°), we suffered from the missing wedge effect [12] which give rises to the volume artifacts that are indicated by the white arrow in Fig. 3.5c. Nonetheless, the reconstructed 3D volume showed clearly that the gap between the nanocubes is free of metal filaments.

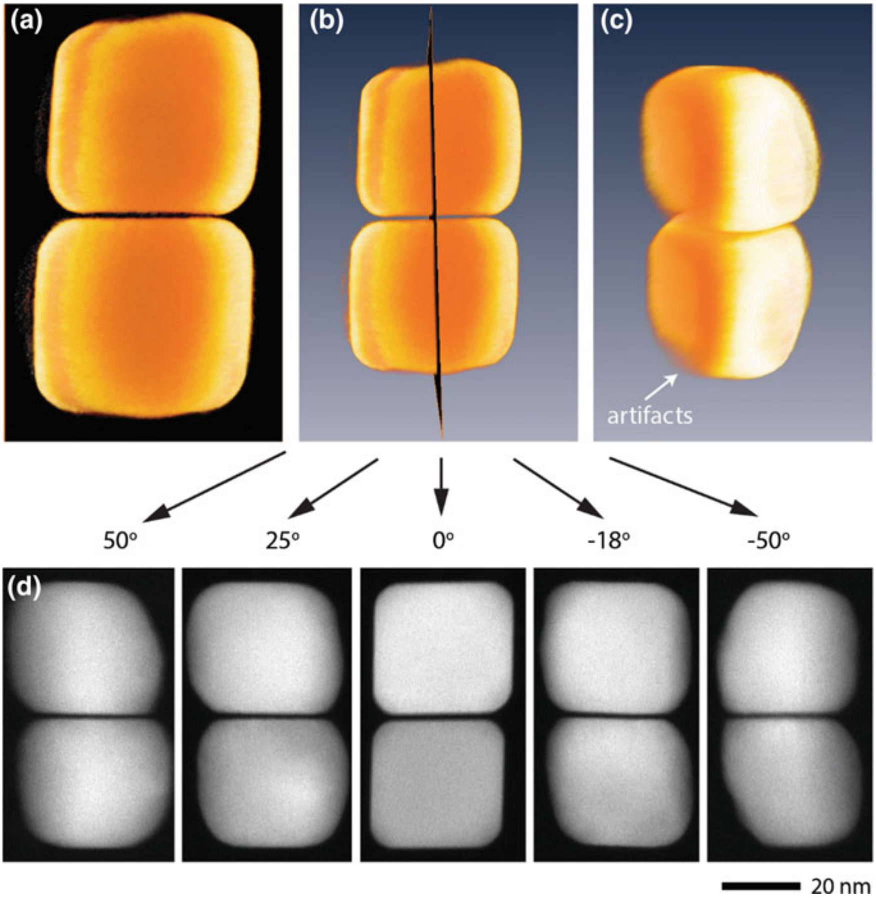

Fig. 3.5 HAADF-STEM tomography images of a dimer of Ag nanocube where the sample was tilted from −50° to +50°. **a** A reconstructed x-y slice extracted from the 3D volume in (**c**). **b** The combination of both. **d** Reconstructed STEM images at different dimer tilts, looking parallel to the gap

3.2.4 UV-Visible (UV-Vis) Spectroscopy

The energy and intensity of the absorption peaks in UV-Vis spectra of plasmonic particles are dependent on the size, shape, and on the dielectric constants of both the metal and surrounding medium [13]. A well-dispersed sample of our Ag nanocubes shows a distinct absorption peak at 429 nm (λ_1) which is same as reported in literature [10]. This peak is equivalent to $\sim$3 eV which is assigned to the plasmon mode of transverse charge oscillation between the cuboid corners. Figure 3.6a,c shows the absorption spectra changes of Ag nanocubes before and after addition of mixed SAMs in ethanol for EDT and BDT, respectively. For systems, upon the addition of mixed SAMs, the peak at 429 nm (I) shifted to the $\sim$440 nm (II) and further shifted to $\sim$450 nm (VIII) within 60 mins. This is due to the change in dielectric constant of the particle environment compared to the PVP coating [14]. The absorbance value dropped significantly after washing with ethanol (EtOH)

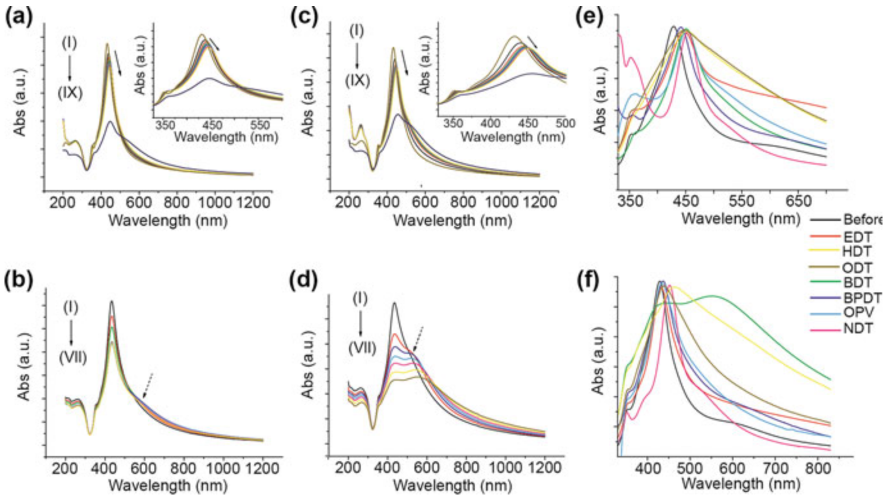

Fig. 3.6 **a** UV-Vis spectra of silver (Ag) nanocubes functionalized with mixed SAMs of 1-propanethiol and 1,2-ethanedithiol or **c** 1,4-benzenedithiol: (I) Ag cubes before addition of mixed self-assembled monolayers (SAMs), (II) 0 min upon addition of mixed SAMs, (III) 10 mins after addition of mixed SAMs, (IV–VIII) each spectrum was recorded in the interval of 10 mins, (IX) Ag nanocubes after addition of mixed SAMs after 60 mins and washed with ethanol (EtOH) (inset). Close up of Fig. (**a**) at 330–500 nm. **b**, **d** UV-Vis spectra of functionalized Ag nanocubes with addition of non-functionalized Ag nanocubes for both EDT and BDT system respectively: (I) Ag nanocubes after addition of mixed SAMs after 60 mins and washed with EtOH. (II) 0 min upon addition of non-functionalized Ag nanocubes, (III) 10 mins after addition of non-functionalized Ag nanocubes, (IV–VIII) each spectrum was recorded in the interval of 10 min. **e** UV-Vis spectra of different SAMs-coated Ag nanocubes after 60 mins. **f** UV-Vis spectra of different SAMs-coated Ag nanocubes after addition of non-functionalized particles after 60 mins

(IX) and the newly formed broad band around 550 nm is prominent after washing with EtOH. After addition of non-functionalized nanocubes, the absorbance value of this newly formed band ~550 nm (λ_2) gradually increases with time. Nanocube assemblies of different lengths exhibit different spectral maxima, but we could only observe a collective response in a broader absorption, without any dominant peak for the EDT system (Fig. 3.6b) [15].

For BDT system, a relatively strong extinction was observed for the band (λ_2) at ~550 nm (Fig. 3.6d). This peak is equivalent to ~2 eV, which is the longitudinal plasmon mode. We attributed this observation to the stronger π-π interaction between the rigid benzene rings than intercalating alkyl chains and $\pi \rightarrow \pi^*$ transitions which results in more linear assemblies than is the case with aliphatic SAMs. Linear dimers and oligomers showed much more pronounced differences in mode energies compared to non-linear arrays [16]. Figure 3.6e,f shows the absorption spectra of Ag nanocubes before and after addition of different SAMs for 60 mins and the addition of non-functionalized particles after 60 min respectively. From these observations we derive three conclusions. (i) Overall, the red-shift of the peak at 429 nm (λ_1) after the addition of SAMs is due to the change in dielectric constant of the environment compared to the PVP coating. (ii) The new peak or band (λ_2) appearing at ~550 nm corresponds to the formation of assemblies after the addition of non-functionalized particles. (iii) The band was not obvious for long alkyl chain assemblies such as HDT and ODT which could be due to the intercalating alkyl chains resulting in severe aggregation. Details of the wavelength shifts between two plasmon resonance modes before and after addition of each linker is tabulated in Table 3.2.

Table 3.2 Summary of Fig. 3.6: the wavelength shift between two plasmon resonance modes after the addition of SAMs and subsequent addition of non-functionalized particles for each linker

Linker	Molecular length (nm), d_l	After addition of SAMs		After addition of non-functionalized Ag nanocubes	
		λ_1 (nm)	$\Delta\lambda = \lambda_1 - \lambda_{before}$ (nm)	λ_2 (nm)	$\Delta\lambda = \lambda_2 - \lambda_1$ (nm)
Before	NA	429	NA	NA	NA
1,2-ethanedithiol (EDT)	0.44	447	18	432	−15
1,6-hexanedithiol (HDT)	0.93	452	23	464	12
1,8-octanedithiol (ODT)	1.17	447	18	440	−7
1,4-benzenedithiol (BDT)	0.63	451	22	434	−17
1,4-biphenyldithiol (BPDT)	0.88	442	13	437	−5
4,4-dimercaptostilbene (OPV)	1.03	452	23	434	−18
1,5-dimercaptonapthalene (NDT)	1.24	454	25	452	−2

3.2.5 X-Ray and Ultraviolet Photoelectron Spectroscopy (XPS and UPS)

The XPS S_{2p} spectra in Fig. 3.7a shows that there was no sulfur signal for Ag nanocubes before functionalization. After addition of mixed SAMs, Ag nanocubes were bonded with mixed SAMs through silver-thiolate (Ag-S) bonds. The two doublet peaks at 162 eV (S1) and 163 eV (S2) were assigned to sulfur bound to the Ag nanocubes [17–19] and free thiol groups respectively [20, 21]. The relative intensities of S1 and S2 were summarized in Table 3.3.

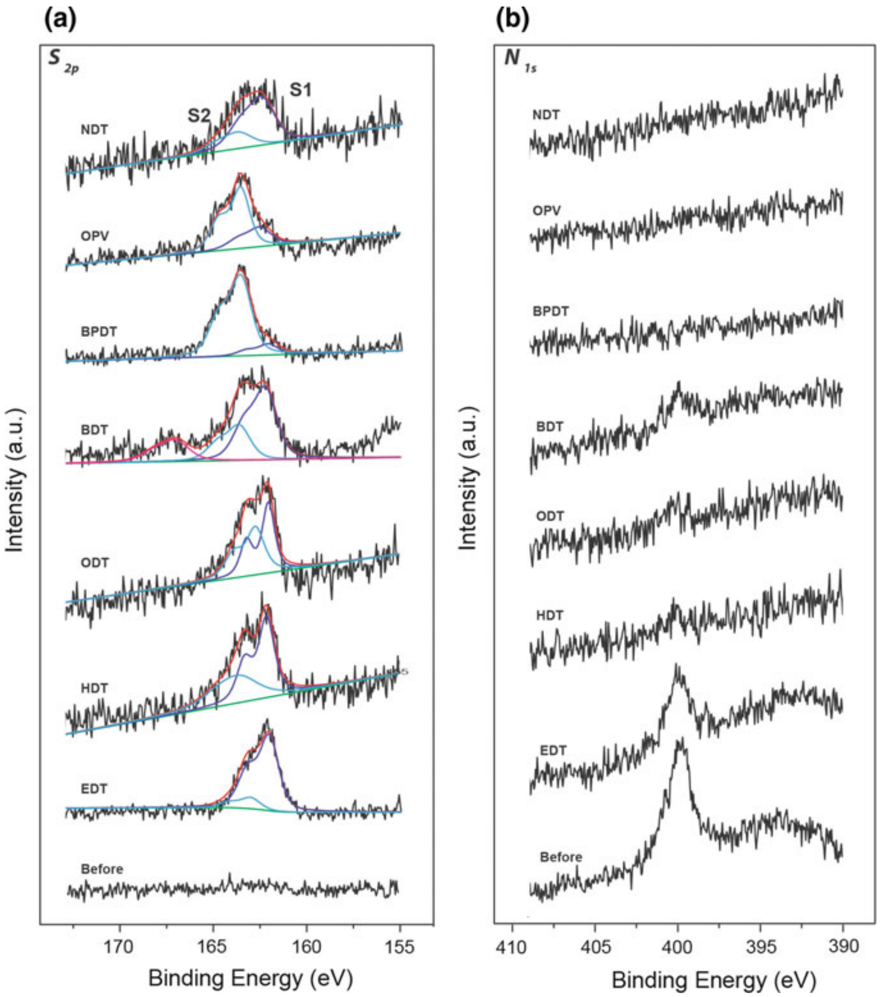

Fig. 3.7 **a**, **b** XPS spectra (S_{2p} and N_{1s} region) of silver nanocubes before (bottom) and after addition of mixed SAMs of thiolates and dithiolates (EDT, HDT, ODT and BDT) or SAMs of dithiolates only (BPDT, OPV, and NDT)

Table 3.3 Summary of Fig. 3.7: relative intensities of peak S1 and S2 for S_{2p} signal and N_{1s} from XPS spectra for each type of junction with different linkers

Linker	S_{2p}		N_{1s}
	S_1 (%)	S_2 (%)	Relative peak area intensity (%)
Before	NA	NA	100
1,2-ethanedithiol (EDT)	87.1	12.9	49.4
1,6-hexanedithiol (HDT)	59.7	40.3	2.3
1,8-octanedithiol (ODT)	51.0	49.0	7.2
1,4-benzendithiol (BDT)	67.2	32.8	20.3
1,5-dimercaptonapthalene (NDT)	73.8	26.2	5.4
1,4-biphenyldithiol (BPDT)	11.4	88.6	0.7
4,4-dimercaptostilbene (OPV)	27.9	72.1	7.7

On the other hand, we attributed the peak at 168 eV for BDT functionalized Ag nanocubes to the presence of oxidized thiols/dithiols molecules. The N_{1s} spectra in Fig. 3.7b also show that the nitrogen signal at 399 eV for Ag nanocubes after functionalization was significantly lower than before functionalization. The nitrogen signal originated from the PVP, the polymer used during synthesis of Ag nanocubes. From the relative intensities as shown in Table 3.3, the N_{1s} signal was significantly lowered by 50.6–99.3% after functionalization. This indicates that the PVP is being replaced by the SAMs. These findings further justify the role of SAMs in controlling the gap sizes between Ag nanocubes.

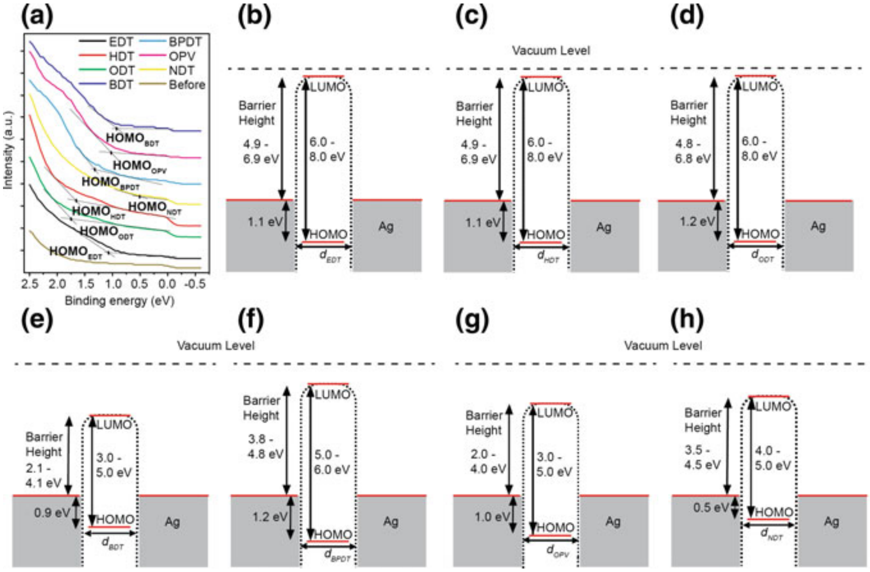

Fig. 3.8 **a** UPS spectra for Ag nanocubes before and after functionalized with mixed SAMs of thiolates and dithiolates (EDT, HDT, ODT and BDT) or SAMs of dithiolates only (BPDT, OPV, and NDT). **b**–**h** are the illustration of energy diagram for all systems

Table 3.4 Summary of Fig. 3.8: HOMO onset values, HOMO-LUMO energy gap values obtained from literature and the estimated barrier height values for each type of junctions with different linkers

Linker	HOMO onset (eV)	HOMO-LUMO gap, E_{HL} (eV)	Barrier height, Φ (eV)
1,2-ethanedithiol (EDT)	1.1	7.0 ± 1.0	4.9 ± 1.0
1,6-hexanedithiol (HDT)	1.6	7.0 ± 1.0	4.4 ± 1.0
1,8-octanedithiol (ODT)	1.7	7.0 ± 1.0	4.3 ± 1.0
1,4-benzendithiol (BDT)	0.9	4.0 ± 1.0	3.1 ± 1.0
1,5-dimercaptonapthalene (NDT)	0.5	4.5 ± 0.5	4.0 ± 0.5
1,4-biphenyldithiol (BPDT)	1.2	5.5 ± 0.5	4.3 ± 0.5
4,4-dimercaptostilbene (OPV)	1.0	4.0 ± 1.0	3.0 ± 1.0

Figure 3.8a shows the UPS spectra for Ag nanocubes functionalized with different SAMs. From the UPS data, we obtained the energy difference between the HOMO onset of the molecule to the Fermi onset of the metal; the data are listed in Table 3.4. The values of the HOMO-LUMO energy gaps were obtained from those reported in the literature [22–26]. By having these two values, we could construct our proposed energy level diagram as shown in Fig. 3.8b–h. The barrier height for junctions bridged by conjugated molecules such as BDT and OPV is lower than those of long and non-conjugated molecules such as EDT. Therefore, by changing the molecules inside the junction, we could not only alter the gap dimension, but also the electronic properties of the junctions. With this, we show the molecular control over the barrier height of the studied system.

3.3 Conclusions

We have demonstrated the use of self-assembled monolayers (SAMs) of molecules to selectively control the gap sizes between two nanostructures down to sub-nanometer scales through self-assembly, assisted by the covalent bonding of anchored sulfur groups. Our experimental approach will be beneficial for connecting nanomaterials into desired arrays and thereby tuning the plasmonic and opto-electronic properties of the nanomaterials which will be important for the future design of plasmonic structures and the development in SERS experiments.

3.4 Experimental Section

3.4.1 General Procedures

The chemicals: poly(vinyl)pyrrolidone (PVP), silver nitrate, 1,2-ethanedithiol (EDT), 1,6-hexanedithiol (HDT), 1,8-octanedithiol (ODT), 1,4-benzenedithiol (BDT), biphenyl-4,4′-dithiol (BPDT), and 4,4-dimercaptostilbene (OPV) were all purchased from Sigma-Aldrich. 1,5-dimercaptonapthalene (NDT) was purchased from Tokyo Chemical Company. Sodium sulfide and ethylene glycol were purchased from J. T. Baker. The glass vials used for synthesis were from Fisher Scientific. Chemicals were used without further purification. Solvents for NP functionalization were freshly distilled prior to use. All stirrer bars were soaked in aqua-regia (mixture of 3:1 volume ratio of nitric acid: hydrochloric acid) for at least 1 hour, washed with deionized water (18.2 MΩ cm) and dried in oven before use. The centrifuges, used for washing NPs, were Rotina (380R) and Profuge (14D). The Transmission Electron Microscopy (TEM) images are recorded on an FEI Titan TEM and a JEOL 2010FEG TEM.

3.4.2 Synthesis of Silver Nanocubes

The polyol method developed by the Xia's group [10] was used to chemically synthesize the single-crystalline Ag nanocubes. 5 ml of ethylene glycol (EG) were injected into each of the four glass vials labeled A, B, C, and D. Then, the stirrer bars were inserted into each vials and pre-heated at 150 °C in an oil bath for at least 1 hour. Then, 70, 80, 90 and 100 µl of sodium sulfide solution (30 mM, Na_2S in EG) were added into the glass vials A, B, C, D respectively. After 8–9 min, 1.5 ml of PVP solution (0.02 g/ml PVP in EG) and 0.5 ml of silver nitrate solution (0.048 g/ml $AgNO_3$ in EG) were added sequentially. The reaction was quenched by removing the glass vials from the oil bath and placing it in an ice water bath once the color of the reaction mixture turned ochre-green. This reaction is highly sensitive to water and the concentration of sodium sulfide and that usually only one out of the four glass vials showed the expected color changes. This reaction was completed within 20 mins. Once the reaction mixture is cooled to room temperature, the Ag nanocubes solution was washed by centrifugation at 2200 rpm (Rotina, 380R) for 30 mins with 25 ml of acetone (AR grade). The supernatant was discarded and the NPs were washed for two times by redispersing them in 2 ml of deionized (DI) water followed by centrifugation (Profuge, 14D) at 10,000 rpm for 10 mins. Finally, the Ag nanocubes solution was transfered into clean glass vials and dispersed them in 4 ml of DI water. The Ag nanocubes solution was wrapped with aluminium foils, sealed with parafilm and kept in dark. Under these conditions, the solutions were stable for two weeks.

3.4.3 Functionalization of Silver Nanocubes with Mixed SAMs

0.1 ml of Ag nanocubes solution was transfered from the glass vial above into a 1.5 ml-centrifuge tube. Centrifugation and redispersion in water was done twice (Profuge, 14D) at 10,000 rpm for 10 mins in order to minimise the concentration of PVP and EG prior to functionalization with mixed self-assembled monolayers (SAMs). Note that too many times of washing (centrifuge and redisperse) will cause the deformation of Ag cubes. Specifically, 5.0 μl of 1-propanethiol ethanolic solution (1×10^{-3} M) and 3.0 μl of 1,2-ethanedithiol ethanolic solution (1×10^{-3} M) were added into 2.36 ml of distilled ethanol. Subsequently, 36 μl of 6–8 nM Ag nanocubes solution was added into the mixture and stirred for 60 min. The reaction mixture was centrifuged with distilled ethanol twice (Profuge, 14D) at 10,000 rpm for 10 mins and re-dispersed in the same solvent. Subsequently, an additional 36 μl of as-prepared non-functionalized Ag nanocubes solution was added quickly into the mixture and incubated for another 60 min. The same procedure was followed for different chain length of thiols and dithiols: 1-heptanethiol and 1,6-hexanedithiol (HDT), 1-nonanethiol and 1,8-octanedithiol (ODT), 1-propanethiol and 1,4-benzenedithiol (BDT). For longer molecules such as biphenyl-4,4′-dithiol (BPDT), 4,4-dimercaptostilbene (OPV) and 1,5-dimercaptonapthalene (NDT), due to their poor solubility in ethanol and binding kinetics, merely dithiol molecules were used instead of mixed SAM of thiols and dithiols. Other than that, the same procedure was repeated for longer molecules except BPDT and OPV solutions, which were prepared in tetrahydrofuran (THF) solvent before adding them into the reaction mixture.

3.4.4 Experimental Techniques

The functionalization process is monitored by UV/VIS/NIR spectroscopy (PerkinElmer Lambda 750). Light transmission was measured through a cuvette of 1 cm light-path. The resulting suspensions ~100 μl of each were spin-coated onto 30 nm-thick gold substrates for XPS characterization. The surface analysis system used for XPS characterization was VG ESCALAB Mark 2. It is equipped with an Omicron (EA125 U7) hemispherical electron spectrometer with 7 channel detection, emission angle of 15 deg, maximum entrance and exit slits. A pass energy of 20 eV was used with a FWHM of 1.0 eV. The X-ray gun used was Omicron Twin Anode X-ray Mg/Al source. Monochromatic Mg K (alpha) radiation at power of 300 W (15 kV × 30 mA) was used for excitation. The peaks fitting were done by using the software of XPSPEAK version 4.1. Characterization of the nanogap sizes and 3D scanning TEM tomography were done with a high-resolution FEI Titan TEM, operated at 200 kV where typically 3 μl of the final suspension was dropcasted onto the silicon nitride membrane (30 nm-thick, S1N1 Agar Scientific).

Gap size measurement was performed on every single TEM image of individual dimer pairs and clusters of particles using the profile function in Gatan software Digital Micrograph version 1.4. The gap size was defined as the interface between two metal surfaces aligned parallel to each other. The histogram in Fig. 3.3 was constructed over 80–100 gap sizes each. The Gaussian peaks fitting were done by using Origin software version 7. The 3D volumes shown in Fig. 3.5 were constructed by using the software Inspect3D.

References

1. Savage KJ, Hawkeye MM, Esteban R, Borisov AG, Aizpurua J, Baumberg JJ. Revealing the quantum regime in tunnelling plasmonics. Nature. 2012;491(7425):574–7.
2. Scholl JA, García-Etxarri A, Koh AL, Dionne JA. Observation of quantum tunneling between two plasmonic nanoparticles. Nano Lett. 2012;13(2):564–9.
3. Tan SF, Wu L, Yang JKW, Bai P, Bosman M, Nijhuis CA. Quantum plasmon resonances controlled by molecular tunnel junctions. Science. 2014;343(6178):1496–9.
4. Camargo PHC, Rycenga M, Au L, Xia Y. Isolating and probing the hot spot formed between two silver nanocubes. Angew Chem Int Ed. 2009;48(12):2180–4.
5. Li W, Camargo PHC, Au L, Zhang Q, Rycenga M, Xia Y. Etching and dimerization: a simple and versatile route to dimers of silver nanospheres with a range of sizes. Angew Chem Int Ed. 2010;49(1):164–8.
6. Broers AN, Molzen WW, Cuomo JJ, Wittels ND. Electron-beam fabrication of 80-Å metal structures. Appl Phys Lett. 1976;29(9):596–8.
7. Cord B, Yang J, Duan H, Joy DC, Klingfus J, Berggren KK. Limiting factors in sub-10 nm scanning-electron-beam lithography. J Vac Sci Technol, B. 2009;27(6):2616–21.
8. Ou FS, Hu M, Naumov I, Kim A, Wu W, Bratkovsky AM, Li X, Williams RS, Li Z. Hot-spot engineering in polygonal nanofinger assemblies for surface enhanced Raman spectroscopy. Nano Lett. 2011;11(6):2538–42.
9. Bosman M, Zhang L, Duan H, Tan SF, Nijhuis CA, Qiu CW, Yang JKW. Encapsulated annealing: enhancing the plasmon quality factor in lithographically–defined nanostructures. Sci Rep. 2014;4.
10. Skrabalak SE, Au L, Li X, Xia Y. Facile synthesis of Ag nanocubes and Au nanocages. Nat Protocols. 2007;2(9):2182–90.
11. Ulman A, Kang JF, Shnidman Y, Liao S, Jordan R, Choi G-Y, Zaccaro J, Myerson AS, Rafailovich M, Sokolov J, Fleischer C. Self-assembled monolayers of rigid thiols. Rev Mol Biotechnol. 2000;74(3):175–88.
12. Lin M, Tan HR, Tan JPY, Boothroyd C, Foo YL, He CB. Transmission electron microscope tomography of nanostructured materials. J Nanoeng Nanomanuf. 2011;1(3):257–64.
13. Eustis S, El-Sayed MA. Why gold nanoparticles are more precious than pretty gold: noble metal surface plasmon resonance and its enhancement of the radiative and nonradiative properties of nanocrystals of different shapes. Chem Soc Rev. 2006;35(3):209–17.
14. Moran CH, Rycenga M, Zhang Q, Xia Y. Replacement of poly(vinylpyrrolidone) by thiols: a systematic study of Ag nanocube functionalization by surface-enhanced Raman scattering. J Phys Chem C. 2011;115(44):21852–7.
15. Thomas KG, Barazzouk S, Ipe BI, Joseph STS, Kamat PV. Uniaxial plasmon coupling through longitudinal self-assembly of gold nanorods. J Phys Chem B. 2004;108(35):13066–8.
16. Quinten M, Kreibig U. Optical properties of aggregates of small metal particles. Surf Sci. 1986;172(3):557–77.

17. Laibinis PE, Whitesides GM, Allara DL, Tao YT, Parikh AN, Nuzzo RG. Comparison of the structures and wetting properties of self-assembled monolayers of n-alkanethiols on the coinage metal surfaces, copper, silver, and gold. J Am Chem Soc. 1991;113(19):7152–67.
18. Heister K, Zharnikov M, Grunze M, Johansson LSO, Ulman A. Characterization of X-ray induced damage in alkanethiolate monolayers by high-resolution photoelectron spectroscopy. Langmuir. 2001;17(1):8–11.
19. Himmelhaus M, Gauss I, Buck M, Eisert F, Wöll C, Grunze M. Adsorption of docosanethiol from solution on polycrystalline silver surfaces: an XPS and NEXAFS study1. J Electron Spectrosc Relat Phenom. 1998;92(1–3):139–49.
20. Full length article. Surf Sci. 1998;405(1):L472–L476.
21. George GA. High resolution XPS of organic polymers—the scienta ESCA 300 data base (G. Beamson and D. Briggs, Wiley, Chichester, 1992, pp. 295, price £65.00). Polymer Int 1994;33(4):439–440. ISBN 0-471-93592-1.
22. Strange M, Rostgaard C, Häkkinen H, Thygesen KS. Self-consistent GW calculations of electronic transport in thiol- and amine-linked molecular junctions. Phys Rev B. 2011;83 (11):115108.
23. Reddy P, Jang S-Y, Segalman RA, Majumdar A. Thermoelectricity in molecular junctions. Science. 2007;315(5818):1568–71.
24. Xiao X, Xu B, Tao NJ. Measurement of single molecule conductance: benzenedithiol and benzenedimethanethiol. Nano Lett. 2004;4(2):267–271.
25. Scheer AM, Gallup GA, Burrow PD. Unoccupied orbital energies of 1,4-benzenedithiol and the HOMO–LUMO gap. Chem Phys Lett. 2008;466(4–6):131–5.
26. Wold DJ, Frisbie CD. Formation of metal–molecule–metal tunnel junctions: microcontacts to alkanethiol monolayers with a conducting AFM tip. J Am Chem Soc. 2000;122(12):2970–1.

Chapter 4
Quantum Plasmon Resonances Controlled by Molecular Tunnel Junction

Abstract Quantum tunneling between two plasmonic resonators links non-linear quantum optics with terahertz nanoelectronics. Direct observation of and control over quantum plasmon resonances at length scales in the range 0.4–1.3 nm across molecular tunnel junctions made of two plasmonic resonators bridged by self-assembled monolayers (SAMs) were demonstrated. The tunnel barrier width and height are controlled by the properties of the molecules. Using electron energy-loss spectroscopy, a plasmon mode, the tunneling charge transfer plasmon, whose frequency (ranging from 140 to 245 THz) is dependent on the molecules bridging the gap was observed.

4.1 Introduction

Quantum mechanical effects in plasmonic structures are believed to become important when two plasmonic resonators are placed so closely that electrons can tunnel across the gap [1–11]. Direct experimental access to the resulting tunneling charge transfer plasmon (tCTP) mode is expected to open up new opportunities in, for instance, nano-scale opto-electronics, single molecule sensing, and non-linear optics [1].

Generally, two types of CTP (Fig. 4.1) have been investigated so far: (1) CTP via conduction and (2) CTP via tunnelling (tCTP). The former has been well-studied by Duan et al. [11]. The low-energy CTP via conduction peak between two gold polycrystalline nanoprisms showed a red-shift in energy loss as a function of the bridge width. However, when the bridge was replaced by a gap of 0.5 nm, the low-energy peak disappeared.

Experimental and theoretical studies so far have concluded that quantum mechanical effects i.e.: the observation of the tCTP mode are important only at length scales below 0.3–0.5 nm, close to the bond length of gold and silver [6, 9–11]. Such structures are technologically inaccessible and therefore it is important to demonstrate the tCTP mode across gaps larger than a nanometer that can be fabricated by state-of-the-art fabrication techniques [11]. Unlike past works that

S. F. Tan, *Molecular Electronic Control Over Tunneling Charge Transfer Plasmons Modes*, Springer Theses, https://doi.org/10.1007/978-981-10-8803-2_4

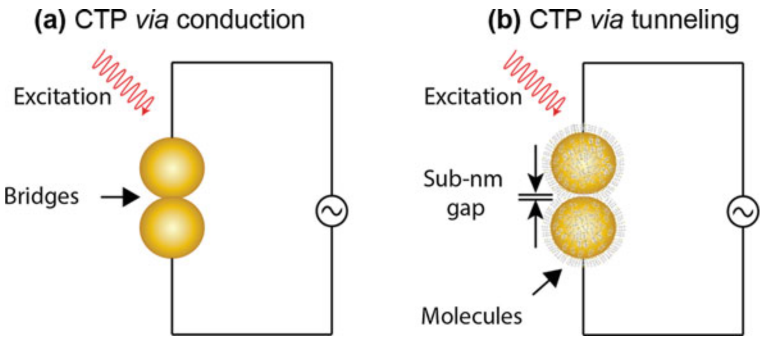

Fig. 4.1 Schematic illustration of quantum tunnelling assisted electrical circuits facilitated by **a** conductive bridges and **b** sub-nanometer gap

investigated tunneling through vacuum [6, 10], we placed the molecules in the gap because tunneling rates across molecules depend on the molecular structure and are much higher than across vacuum.

Routine experimental tunnel junctions on molecular monolayer (Fig. 4.2) has been proven that the low tunnelling decay coefficient of the molecules (β) will give rise to the high tunnelling rates across the junctions. This approach made it possible to directly observe and control tCTPs experimentally in tunneling gaps up to at least 1.3 nm, depending on the type of molecules bridging the gap, and moves quantum plasmonics into the size domain that is accessible via bottom-up or top-down fabrication methods [11].

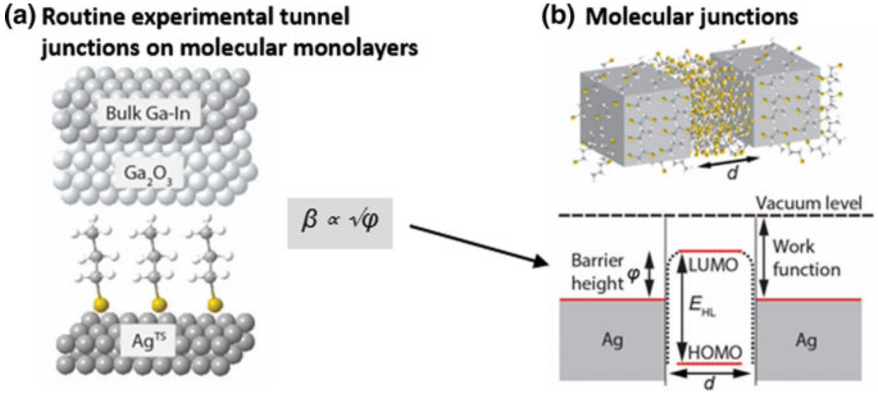

Fig. 4.2 **a** Routine experimental tunnel junctions on molecular monolayers. **b** Schematic illustration of the molecular tunnel junctions made of two silver nanoparticles bridged by SAMs and a schematic energy-level diagram of the junctions. Figure **b** reprinted from Ref. [13], with permission from The American Association for the Advancement of Science, Copyright 2014

Quantum effects have been observed only indirectly as shifts in the bonding dipolar resonance plasmon mode [1, 6, 10]. Our aim was to perform an experiment where the presence of a tunneling barrier can be directly imaged, while the tCTP mode is simultaneously measured spectroscopically. In this Chapter, we study the molecular electronic control over the tCTP mode.

4.2 Results and Discussion

4.2.1 Synthesis and Functionalization of Silver Nanocubes

Refer to Sect. 3.2.2. The experimental details of the synthetic procedures and characterization techniques are reported in the experimental section at end of this Chapter. Here, we only give a brief description.

We introduced two experimental innovations: (1) the cross-sectional area of the tunnel junction was increased from a few nm^2 to roughly 10^3 nm^2 and (2) the tunneling rate across the nano-gaps was increased by tunneling through molecules rather than vacuum.

Cubic silver (Ag) nanoparticles (NPs) were used [12] separated by SAMs with thicknesses of 0.5–0.6 nm forming metal-SAM-metal junction via self-assembly (Fig. 4.3a). The faces of the NPs are atomically flat, which results in a very large cross-sectional area of around 10^3 nm^2, maximizing the number of tunneling events across the junctions. The Ag NPs were functionalized with either saturated, aliphatic 1,2-ethanedithiolates (EDT), or aromatic 1,4-benzenedithiolates (BDT) [13]. The lengths of EDT and BDT are similar, but they have very different highest occupied molecular orbitals-lowest unoccupied molecular orbitals (HOMO-LUMO) gaps of 8 and 5 eV, respectively [14–16]. Therefore, the tunneling rates across junctions with BDT molecules are higher than those junctions with EDT. The interaction between the two NPs was optimized to avoid aggregation or misalignment by diluting the dithiols with 1-propanethiol (PT) [13]. After self-assembly of the dimeric structures, they were deposited on a 30 nm thick, electron transparent silicon nitride membrane.

A simplified form of the Simmons equation (Eq. 4.1) is commonly used to approximate molecular tunnel junctions [17, 18]

$$J = J_0 e^{-\beta d} \quad \text{with} \quad \beta = 2\sqrt{\frac{2m\varphi}{\hbar^2}} \tag{4.1}$$

where β (Å^{-1}) is the tunneling decay coefficient, d (nm) is the width of the tunneling barrier, and the pre-exponential factor J_0 (A/cm^2) is the hypothetical current when $d = 0$; m is the mass of the charge carrier (kg), and $\hbar$ is the reduced Plank's constant. The value of β depends on the barrier height φ (eV). Tunneling rates through molecular bonds, so-called through-bond tunneling, are much higher (β 0.8–0.9 Å^{-1} for saturated molecules and 0.1–0.3 Å^{-1} for unsaturated molecules) than through vacuum (β = 2.9 Å^{-1}) [19]. Figure 4.2b shows the energy level

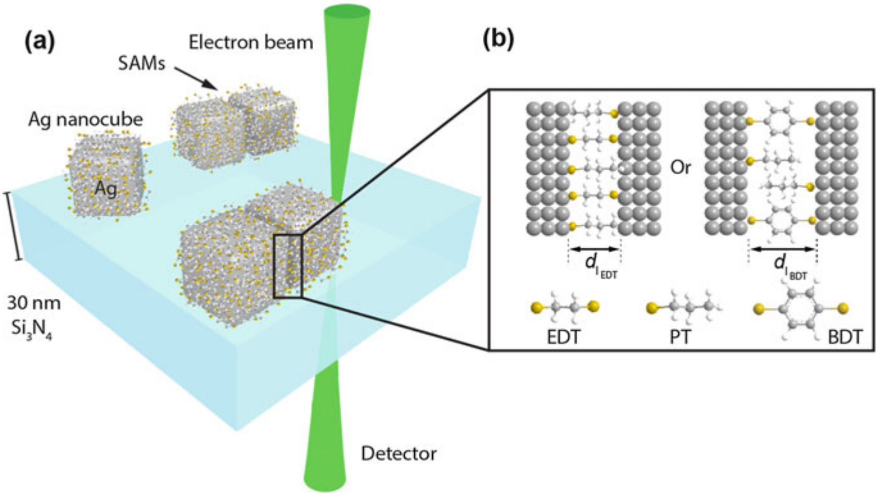

Fig. 4.3 Quantum plasmonic tunnel junctions. **a** Schematic illustration of the molecular tunnel junctions made of two silver nanoparticles bridged by a SAM on an electron transparent silicon nitride membrane. The contactless electron nano-probe was placed near the functionalized silver nanoparticles to excite and measure the surface plasmons of individual dimers. **b** The distance between two adjacent nanoparticles is determined by the thickness of the SAMs of EDT or BDT. Figure reprinted from Ref. [13], with permission from The American Association for the Advancement of Science, Copyright 2014

diagram of the metal-SAM-metal junctions schematically. As indicated in Fig. 4.2b, in molecular electronics d is defined by the length of the molecule, d_l (nm), and φ by the offset between the Fermi-levels of the metal and the energy level of the molecular frontier orbitals. In contrast, when the through-space tunneling is the dominant mechanism of charge transport, the barrier height equals the work function of the electrode materials and d equals the gap, d_g (nm), between the two electrodes, i.e., the distance between the NPs [20].

4.2.2 Electron Energy-Loss Spectroscopy (EELS)

Instead of bringing the dimer NPs in contact with electrical probes that will perturb the plasmon resonances, we used in our experiment a focused beam of energetic electrons in a scanning transmission electron microscope (STEM) as a contactless nanoprobe to excite and analyze the surface plasmon resonances in individual dimers. We positioned the electron probe opposite the gap at the long axis of a silver NP dimer, as illustrated in Fig. 4.3a, to excite longitudinal plasmon modes—similar to lateral plane wave illumination of the dimer [13]. During the plasmon excitation, the tunnel junction was therefore not exposed to the electron beam to minimize irradiation damage [13]. The excitation of plasmon resonances results in an energy transfer from the electron beam to the NP system, which we analyzed with monochromated electron energy-loss spectroscopy (EELS) [21–23]. The junctions were imaged before and after acquiring the EELS spectra to ensure that none of these junctions formed conductive metal filaments during the experiment [13]. Thus, in all of our experiments we could discriminate between the tunneling and conduction through metal filaments—CTP modes conclusively.

4.2.3 Molecular Control Over the Gap Sizes

Figure 4.4a shows the representative TEM overview image after the functionalization process. From this image, it can be seen that dimers, as well as single particles and larger clusters are present on our samples. Figure 4.4c shows atomic-resolution TEM images of a Ag NP dimer. The first peak in the histograms of values of d_g estimated from TEM images on a series of dimers are centred at 0.55 ± 0.08 nm for EDT (Fig. 4.4d) and 0.67 ± 0.12 nm for BDT (Fig. 4.4e)

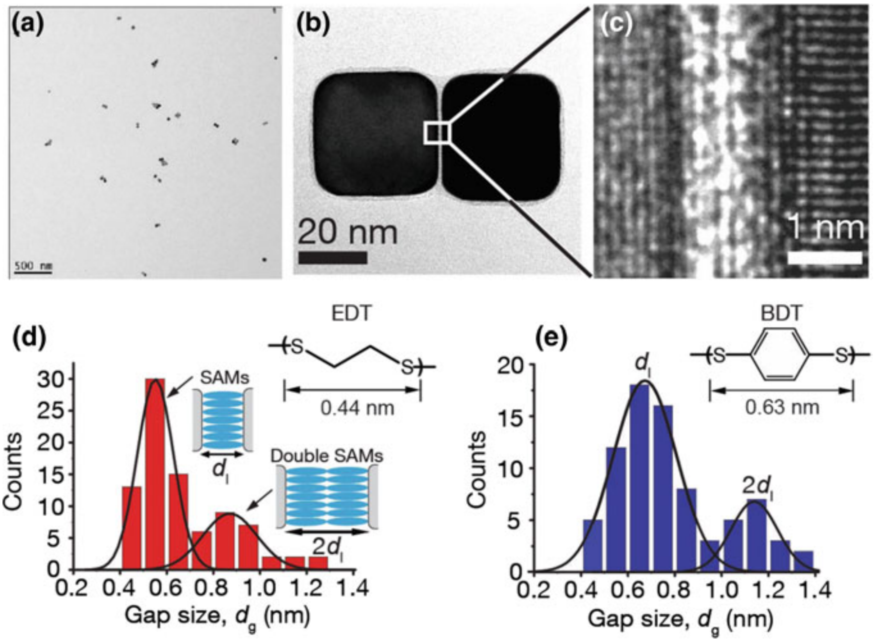

Fig. 4.4 **a** Representative TEM overview image of the Ag nanocubes after functionalization with mixed SAMs of PT and BDT. **b** High resolution TEM image of a dimer with 0.8 nm separation. **c** Atomic resolution TEM image of the high aspect ratio gap (0.8 × 30 × 30 nm^3). Histogram of gap sizes for **d** EDT and **e** BDT molecular junctions. Figure reprinted from Ref. [13], with permission from The American Association for the Advancement of Science, Copyright 2014

which are close to d_l as expected for Ag-SAM-Ag structures. The second peak in these histograms is attributed to dimers with SAMs on both NPs (Ag-SAM//SAM-Ag structures). Intercalating SAMs or not completely removed polymer that was used in the NP synthesis may result in smaller and larger gap sizes than expected from the molecular lengths, as indicated schematically in Fig. 4.8a.

4.2.4 Molecular Control Over the Barrier Heights

From the UPS data, we obtained the energy difference between HOMO onset of the molecule to the Fermi onset of the metal. The HOMO onset values were determined by linear extrapolation of the lower binding energy side of the HOMO peak intercepted with the linear extrapolation of the base line as denoted by the black lines and solid vertical bars in Fig. 4.5a. The value of HOMO-LUMO energy gap were obtained from those reported in single-molecule spectroscopy [24–28]. By having these two values, we could construct our proposed energy level diagram as shown in Fig. 4.5b. Barrier height for junctions bridged by conjugated molecules such as BDT is lower than the non-conjugated molecules such as EDT by 2.7 eV. By changing the molecules inside the junction, we could not only alter the gap dimension, but also the electronic properties of the junctions. With this, we show the molecular control over the barrier height of the studied system.

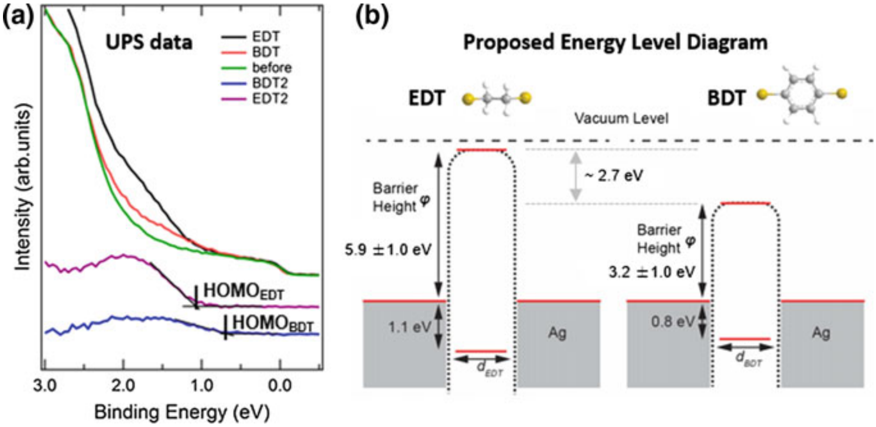

Fig. 4.5 **a** UPS spectra for Ag nanocubes before and after functionalized with mixed SAMs of thiolates and dithiolates (EDT and BDT). **b** Proposed energy level diagram for the EDT and BDT system

4.2.5 *Experimental Evidence of Tunneling CTP Peak*

Figure 4.6a, b show EELS spectra recorded from junctions with SAMs of EDT and BDT. Three main plasmon peaks were observed around 2.2, 3.2 and 3.6 eV, which we assigned to the bonding dipolar plasmon mode (II), the transverse corner mode (III), and the transverse edge mode (IV), respectively, in agreement with the finite-element-model (FEM) simulations (Fig. 4.6c) [13, 20]. A new low-energy plasmon mode is observed at 0.60 ± 0.04 eV for EDT and 1.01 ± 0.01 eV for BDT.

We assigned this plasmon mode to the tCTP based on our calculations that show the transfer of net charge between the cubes (Fig. 4.6c, mode I). The plasmon resonances of the Ag-SAM-Ag system were simulated using a quantum-corrected FEM optical simulation model [13, 20]. Briefly, the optical properties of the junctions are calculated through a quantum mechanical approach and then used to simulate the plasmon resonances of the Ag-SAM-Ag system. The model predicts that the tCTP mode strongly depends on φ, d, and gap field, E_{gap} (V/m). The value of φ is modeled analytically as $\varphi = \alpha\ E_{\mathrm{HL}}$, where $0 < \alpha < 1$ relates to the energy-level alignment, and E_{HL} is the HOMO-LUMO gap, which was obtained

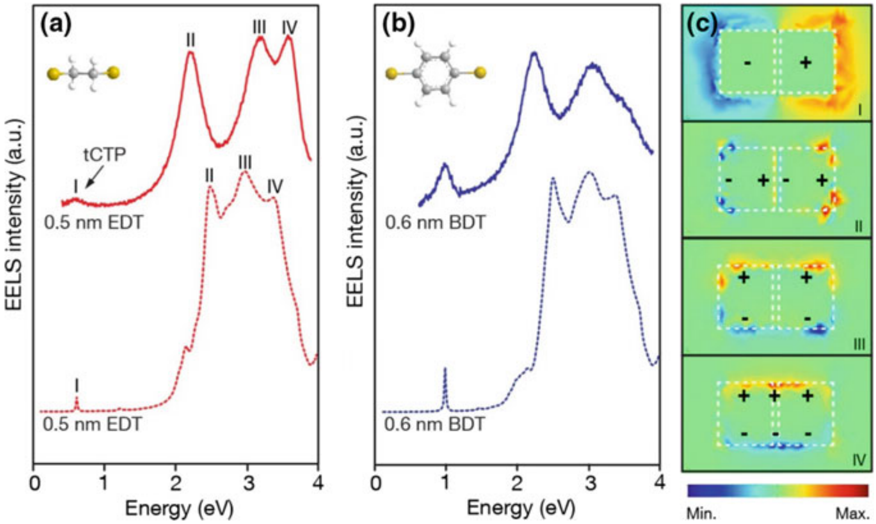

Fig. 4.6 Direct observation of quantum tunneling between plasmon resonators. Two examples of measured EELS spectra with the occurrence of quantum tunneling directly observed *via* the tCTP peak and quantum-corrected simulations of the extinction spectra, confirming the identification of the peaks. Experimentally measured EELS spectra (solid line) and theoretical calculated spectra (dotted line) for dimers functionalized with **a** EDT and **b** BDT respectively. **c** Simulated maps of the electrical-field distributions for the plasmon modes I–IV, corresponding with the spectral peaks. Figure reprinted from Ref. [13], with permission from The American Association for the Advancement of Science, Copyright 2014

from single molecule experiments [14–16]. We assume $E_{\mathrm{gap}} = 7 \times 10^{8}$ V/m throughout the calculations based on previously-reported work [13, 20].

Through Bond *Versus* Through Space Tunneling

There are two possible tunneling processes in our molecular tunnel junction: (1) through-space tunneling and (2) through-bond tunneling. For junctions with either tilted SAMs or well-aligned SAMs (Fig. 4.7) both types of mechanisms may apply. In through-space tunneling, the tunneling path is defined by the gap size d_{g} between the two electrodes; and for through-bond tunneling, the electrons will tunnel through the molecule with the tunneling path defined by the molecular length d_{l}. In case that through-bond tunneling dominates over through-space tunneling, we expect the tCTP to be only dependent on d_{l} and not on d_{g}.

In calculating through-space tunneling process, the gap size d_{g} was used, which is defined by the distance between the two electrodes. For different dimers with the same monolayer SAM, although the SAMs are the same length, the measured d_{g} could be different due to the orientation of SAMs (Figs. 4.4d, 4.7 and 4.8a). In the calculations, the measured gap sizes are used. On the other hand, for the through-bond tunneling process, the molecular length defines the tunnel length, so we used d_{l} for all the monolayer samples in the quantum-tunneling calculations. It

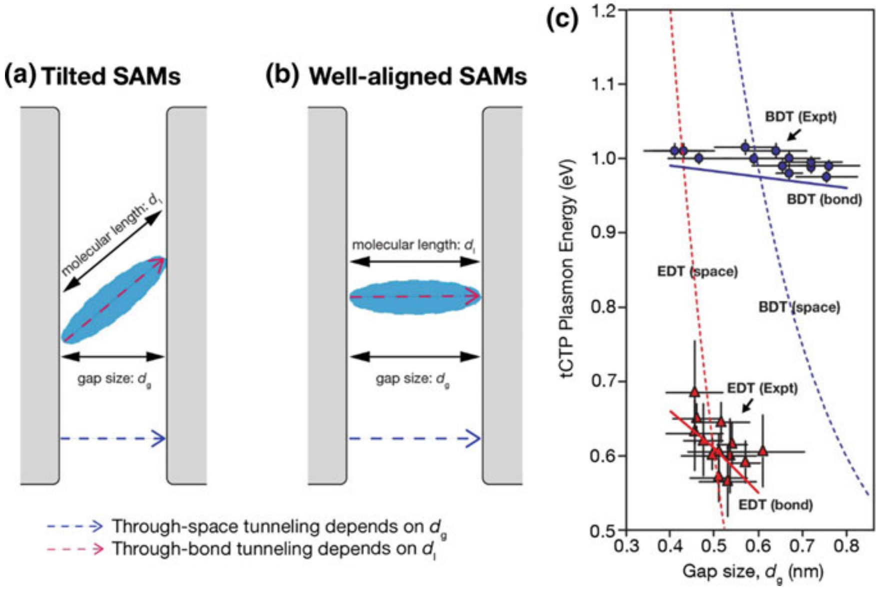

Fig. 4.7 Schematic of molecular orientation in the dimer gap, and its effect on the tunneling process. **a** Tilted SAMs and **b** well-aligned SAMs. **c** Experimentally measured plasmon energy as a function of gap size for dimers functionalized with monomers of BDT (filled circle) and EDT (filled triangle). Theoretical calculations for through-space and through-bond tunneling are shown as dotted lines and solid lines respectively for the two SAMs. Figure **c** reprinted from Ref. [13], with permission from The American Association for the Advancement of Science, Copyright 2014

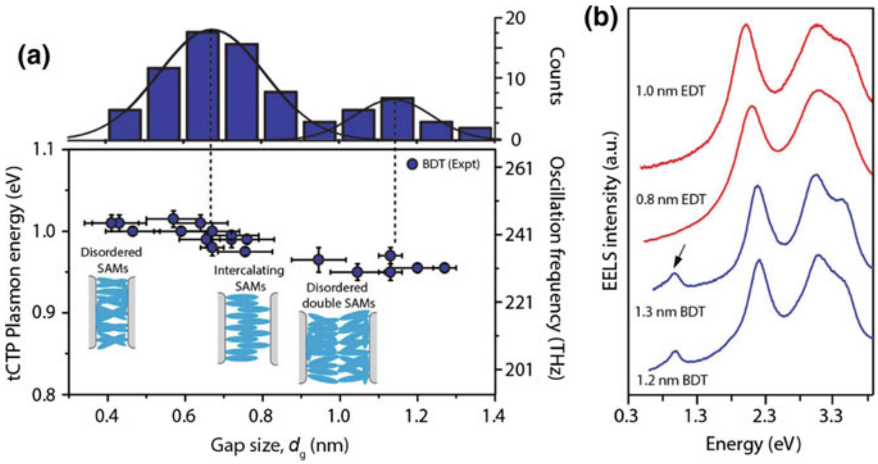

Fig. 4.8 Quantum plasmon resonances as a function of tunneling distance. **a** Experimentally measured plasmon energy as a function of gap size for BDT-(filled circle) functionalized dimers. The gap size varies between individual dimers because of structural disorder in the SAMs. **b** Measured EELS spectra for double SAMs of EDT (red) and BDT (blue). Tunneling was observed for the double layer BDT but not in the double layer EDT. Figure reprinted from Ref. [13], with permission from The American Association for the Advancement of Science, Copyright 2014

should be noted that our model is a simplified physical model, which does not consider any microscopic details of the SAM. These effects can for example be taken into consideration by changing the barrier height $\varphi = \alpha E_{\mathrm{HL}}$. To take into the account the molecular orientations, the barrier height φ (or the energy alignment parameter α) is varied: φ = 3.3–3.5 eV for EDT and φ = 1.0–1.5 eV for BDT.

In addition to the two possible tunneling mechanisms, if by any chance our SAM layer is damaged or ionized during our experiment, we may have the third possibility: ionic conduction and/or hopping (which are slow relative to optical time scales). If this is the case, the conductivity of SAM will be (nearly) independent of spacing (either d_g or d_l). The nature of the charge transport—through-space or through-bond tunneling—was determined from EELS measurements on 32 junctions, for which the energy of the tCTP mode was plotted as a function of d_g (Fig. 4.7c). This graph shows that the tCTP depends only weakly on the value of d_g. The dotted lines in Fig. 4.5c shows simulations of the tCTP energy shifts if through-space tunneling would dominate, with $d = d_g$ [13]. The solid lines are simulations for through-bond tunneling with $d = d_l$, where the through-bond tunneling distance depends on the length of the molecule and can be different from d_g when the molecules are not perfectly aligned in the gap. Figure 4.7c shows that through-bond tunneling has a much weaker dependence on gap size than through-space tunneling. The good agreement with the experimental results indicates that coherent through-bond tunneling is the dominant mechanism of charge transport [13].

4.2.6 *Tunneling Is Possible for Gap Size > 1 nm*

Through-bond tunneling could allow us to explore tCTP across a large gap as the tunneling is less dependent on the gap size. EELS spectra were recorded on Ag-SAM//SAM-Ag junctions to study whether the tCTP mode could be observed over larger length scales up to 1.3 nm. Figure 4.8 shows that a tCTP mode for the structures with BDT appears at 0.975–1.015 eV. The tCTP peak energy only weakly depends on d_g, which confirms that though-bond tunneling is the dominant mechanism of charge transport. The marginal difference in energy of the tCTP mode for single and double SAMs is likely due to strong π–π coupling between the BDT SAMs [29]. For Ag-SAM//SAM-Ag structures with EDT, the tCTP mode was not observed because of the low β value and that no π–π coupling occurs between aliphatic molecules, we expected its peak—if any—to be at very low energies beyond the detection limit of our instrument.

4.3 Conclusions

By combining atomic-resolution imaging, single-particle spectroscopy, and monolayer molecular control, we have demonstrated quantum-mechanical electron tunneling at optical frequencies between plasmon resonators. By varying the self-assembled molecular monolayers in the junctions, the plasmon-induced tunneling frequencies could be controlled from 1.01 ± 0.01 eV, or 244 ± 3 THz, for a monolayer of BDT molecules, to 0.60 ± 0.04 eV, or 145 ± 10 THz, for a monolayer of EDT molecules. The mechanism of charge transport was coherent through-bond tunneling which is only weakly dependent on the gap size. The relatively large distance of up to 1.3 nm over which the tunneling takes place in Ag-BDT//BDT-Ag junctions, may provide potential for molecular control over quantum plasmonic systems through longer molecules to perhaps 4–5 nm [30], i.e., gap sizes that are currently accessible by top-down fabrication techniques. Our results show that tunneling can reconcile molecular electronics with plasmonics, opening up a whole new, interdisciplinary field of exploration.

4.4 Experimental Section

4.4.1 *General Procedures*

For the silver nanocubes, the chemicals poly(vinyl)pyrrolidone (PVP), silver nitrate, 1,2-ethanedithiol (EDT), 1,4-benzenedithiol (BDT) were all purchased from Sigma-Aldrich and used without further purification. Sodium sulfide and ethylene glycol were purchased from J. T. Baker. The glass vials used for synthesis were obtained from Fisher Scientific. Solvents for NPs functionalization were freshly distilled prior to use. All stirrer bars were soaked in aqua-regia (mixture of 1:3 volume ratio of nitric acid: hydrochloric acid) for at least 1 hour, washed with deionized water (18.2 Ω cm) and dried in an oven before use. NPs were washed in Rotina (model 380R) and Profuge (model 14D) centrifuges.

4.4.2 *Synthesis of Silver Nanocubes*

Refer to Sect. 3.4.

4.4.3 *Functionalization of Silver Nanocubes with Mixed SAMs*

Refer to Sect. 3.4.

4.4.4 *EELS Measurements*

Plasmon characterization on individual pairs of Ag nanocubes is carried out in scanning TEM (STEM) mode using an FEI Titan TEM with Schottky electron source, operated at 80 kV. The diameter of the used electron probe is about 1 nm, and a 13 mrad convergence semiangle was used. For EELS spectroscopy, electrons within a solid semiangle of 13 mrad were collected, using a Gatan Tridiem ER EELS detector. It is worth noting here that during the EELS measurements, the STEM probe was positioned outside the tunnel junction. The SAMs were therefore not exposed to the electron beam when the spectra were acquired. This proved critical, as we also tried EELS mapping, but here the whole dimer had to be irradiated during the acquisition, including the tunnel junction. The long (minutes) total exposure of the SAMs during these mapping attempts proved too destructive and the tCTP mode disappeared. For tCTP measurements, it is therefore important to minimize the electron beam exposure of the SAMs, as we did during our EELS measurements without irradiating the dimer gaps.

A Wien-type monochromator dispersed the electron beam in energy, and a narrow energy-selecting slit formed a monochrome electron beam with typical full-width at half-maximum values of 70–80 meV. EELS spectra were acquired with a modified binned gain averaging routine [22]. Each individual spectrum was acquired fast, with illumination periods around 40 ms, using 16 times on-chip binning for detector CCD readout. Spectra shown are typically summations of 2000 individual, aligned spectra. The spectra were all normalized at their maximum, the top of the zero-loss peak. All spectra were acquired 1–2 nm off the edge on the long dimer axis. The background signal was corrected by fitting and subtracting a high-quality background spectrum that was measured at a clean area of the same sample without particles nearby.

4.4.5 Simulation Methods

The simulation work is developed in collaboration with Dr. Wu Lin and Dr. Bai Ping from Institute of High Performance Computing (IHPC). A quantum-corrected finite-element-method (FEM) optical simulation model [9, 20] is employed to study the plasmon resonances of the Ag-SAM-Ag system. The quantum-tunneling process in the molecular tunnel junction is modeled by first determining the tunneling barrier profile of the Ag-SAM-Ag [20] via: (1) the intrinsic barrier height φ at the interface of Ag and SAM, (2) the image charge potential, which is gap size d_g dependent and is essential for the sub-nanometer gaps, (3) the electric field E_{gap} in the gap (4), the tunneling electron self-induced space charge field, and (5) the quantum exchange-correlation field. Then the Schrödinger equation and the Poisson equation are solved iteratively using a WKB-type approximation technique for the tunneling barrier profile and the tunneling electron density (n) which can be used to obtain the optical conductivity of the tunneling junction $\sigma(\omega)$ [20].

The difference here for our Ag-SAM-Ag system is the intrinsic barrier height φ, which is no longer the work function of the Ag electrode. Instead, the barrier height φ is the energy level alignment of the molecular frontier orbitals of the SAMs and the Fermi-levels of the Ag electrode, which is rather difficult to predict theoretically. We used a simple formula to model the intrinsic barrier height $\varphi = \alpha E_{\mathrm{HL}}$ (where $0 < \alpha < 1$), which is determined by two factors. The first is the type of SAM in the tunneling junction, which is modeled by E_{HL} (i.e., the energy difference between HOMO and LUMO). The values of E_{HL} used in our calculation are obtained by single molecule experiments [14–16, 19] and ab initio calculations [31]. The second factor is the energy level alignment of the molecular frontier orbitals with respect to the Fermi-levels of the Ag electrode, which is modeled by α with $0 < \alpha < 1$. Simply changing the parameter α allows us to study the effect of the energy alignment on the plasmonic response. The value of α used in the calculations is determined by experimental results, for example, $\alpha = 0.425$ for EDT and $\alpha = 0.25$ for BDT.

The gap field E_{gap} at the Ag/SAM interface generated during the EELS excitation is difficult to be obtained experimentally. To find the E_{gap}, we first conducted theoretical calculations using previously published method [20] and found that the E_{gap} is $\sim 7 \times 10^8$ V/m for the Ag/EDT/Ag system to excite a tCTP mode at 0.6 eV. To further confirm the calculation result, we estimated the average field in the SAM layer with a capacitance model based on our EELS measurements. The capacitance of a gap is defined as $C = \varepsilon_r \varepsilon_0 \frac{A}{d_g}$, where A is the area of overlap of the two plates, ε_r is the relative static permittivity of the material between the plates, ε_0

is the electric constant ($\varepsilon_0 \approx 8.854 \times 10^{-12}$ F m^{-1}), and d_g is the separation between the plates. Taking the energy stored in the capacitor is the plasmon energy E_{plasmon}, then $E_{plasmon} = 1/2CV^2$, where V gives the voltage between the plates. Therefore the average field in the gap is $\overline{E}_{gap} = \frac{V}{d_g} = \sqrt{\frac{2E_{plasmon}}{d_g A \varepsilon_r \varepsilon_0}}$. For the case of EDT [$\varepsilon_r = (1.558)^2$], a gap size of 0.5 nm and cross sectional area of 37 × 37 nm^2, the CTP plasmon energy is about 0.6 eV. This gives an average field of 1.142×10^8 V/m. The field distribution within the SAM layer shows a non-uniform profile which has the strongest field at the edge of Ag/SAM. It is this edge field at the interface of Ag/SAM that plays the major role in the tunneling process. Taking into account the fact that edge field is much larger than the average field, the theoretically estimated gap field $E_{\text{gap}} = 7 \times 10^8$ V/m. This value of E_{gap} was then used throughout the calculations to predict the trends in the frequency of tCTP peak as a function of d_g, d_l, and the tunnel barrier height, (as shown in Figs. 4.7 and 4.8) which are in excellent agreement with the experimental results.

After obtaining the optical properties of the molecular tunnel junction, the plasmon resonances of the Ag-SAM-Ag system can be simulated from classical electromagnetic calculations, more specifically, a finite-element-method (FEM) optical simulation model is used. Here the two identical Ag cubes are assumed to have a square cross section with side length w = 37 nm, and the length of each Ag cube is L = 35 nm based on the TEM images. The Ag's dielectric function is taken from Palik's handbook [32]. Between the two Ag cubes, a tunneling path (filled with the tunneling electrons) is assumed to have a square cross section with area $A = 37 \times 37$ nm^2, and the length of the tunneling path is determined either by the gap size d_g or the molecular length d_l (discussed in next section). This tunneling path is modeled using $\varepsilon(\omega) = 1 + i\frac{\sigma(\omega)}{\omega\varepsilon_0}$ as described above. In addition, to account for the fact that species may be added during our experiment, each Ag cube is assumed to be coated with a 0.5-nm-thick self-assembled monolayer (SAM), with a refractive index of 1.558 (EDT) or 1.665 (BDT) [33]. For simplicity, the 30 nm Si_3N_4 substrate is neglected in our optical simulations. As the effect of the thin substrate is small for low-energy plasmon modes, this simplification has little effects on the simulations of the low-energy tCTP mode [34].

Scattered-field formulation in COMSOL finite element method is used to solve the three-dimensional Maxwell's equations. The spectra of absorption, scattering and their sum (i.e., extinction) cross sections of the Ag-SAM-Ag system can be calculated. Simulations are performed using plane-wave excitation for two polarization conditions: the incident light is polarized along the longitudinal axis (i.e., long axis) or along the transverse axis (i.e., short axis). Longitudinal and transverse mode components (dash lines in Fig. 4.9) are obtained separately. The final simulated extinction spectrum (the black solid line in Fig. 4.9) to be compared with EELS measurement is an algebraic summation of the longitudinal and transverse mode components.

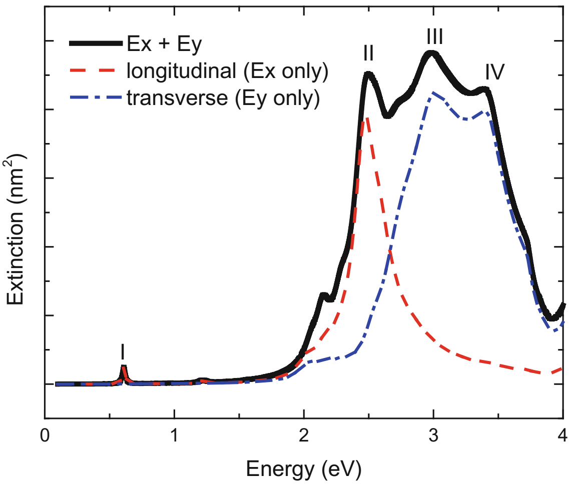

Fig. 4.9 Simulated EELS spectra for an Ag-EDT-Ag dimer system under longitudinal polarization (in the dimer's length direction; red dashed line), or transverse polarization (perpendicular to the dimer's length axis; blue dash-dotted line), and their summation (black line)

As shown in Fig. 4.7, our quantum corrected classical model indeed fits our experimental data well. This good agreement makes it possible to estimate the molecular conductance of individual EDT and BDT at their tCTP resonance crudely. In our simulations, we used an electric field of 7 × 10^8 V/m resulting in a conductance of 3238 G_0 for EDT and 7321 G_0 for BDT, where the molecular length is 0.5 nm for EDT and 0.6 nm for BDT, the cross sectional area of the both SAM layers are 37 × 37 nm^2, and G_0 is the quantum conductance. We estimate that 16,000 molecules are present in the junction based on a previously reported

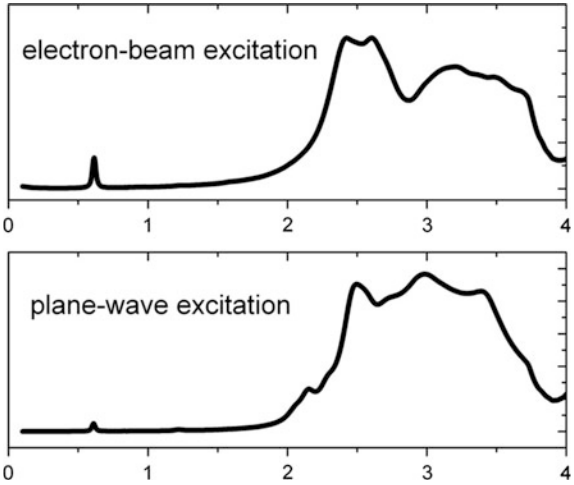

Fig. 4.10 Simulated EELS spectra for an Ag-EDT-Ag dimer system using an optical approach for electron-beam excitation (top panel) and plane-wave excitation (bottom panel, as shown in Fig. 4.6)

surfaces coverage of 8.0×10^{-10} mol/cm^2 for these molecules on Ag surfaces [35, 36]. Therefore, the conductance per EDT or BDT molecule is roughly 0.20 G_0 and 0.46 G_0 at the tCTP resonance respectively. These single molecule conductance values are in good agreement with those literature reported for break junction measurements [37, 38].

We have also performed electron-beam excitation simulations, which produce similar results as our plane-wave excitation simulations as shown in Fig. 4.10. The electron-beam excitation is modelled as a small electron beam ($\sim$1 nm^2) which carries current in the incident direction and creates an electromagnetic field background, and then the optical extinction spectra of the particle system are collected.

The reason why we choose the present plane-wave excitation is mainly due to its simpler physics and less free-tuning parameters in simulation which makes the simulation results more reliable. Compared to the well-established plane-wave excitation modelling, using an optical approach to model electron-beam excitation is still a relatively new research area [39, 40] and more efforts will be made toward this direction.

References

1. Tame MS, McEnery KR, Ozdemir SK, Lee J, Maier SA, Kim MS. Quantum plasmonics. Nat Phys. 2013;9(6):329–40.
2. Brongersma ML, Shalaev VM. The case for plasmonics. Science. 2010;328(5977):440–1.
3. Romero I, Aizpurua J, Bryant GW, García De Abajo FJ. Plasmons in nearly touching metallic nanoparticles: singular response in the limit of touching dimers. Opt Express. 2006;14(21):9988–99.
4. Zuloaga J, Prodan E, Nordlander P. Quantum description of the plasmon resonances of a nanoparticle dimer. Nano Lett. 2009;9(2):887–91.
5. Marinica DC, Kazansky AK, Nordlander P, Aizpurua J, Borisov AG. Quantum plasmonics: nonlinear effects in the field enhancement of a plasmonic nanoparticle dimer. Nano Lett. 2012;12(3):1333–9.
6. Savage KJ, Hawkeye MM, Esteban R, Borisov AG, Aizpurua J, Baumberg JJ. Revealing the quantum regime in tunnelling plasmonics. Nature. 2012;491(7425):574–7.
7. Song P, Nordlander P, Gao S. Quantum mechanical study of the coupling of plasmon excitations to atomic-scale electron transport. J Chem Phys. 2011;134(7).
8. Kern J, Großmann S, Tarakina NV, Häckel T, Emmerling M, Kamp M, Huang J-S, Biagioni P, Prangsma JC, Hecht B. Atomic-scale confinement of resonant optical fields. Nano Lett. 2012;12(11):5504–9.
9. Esteban R, Borisov AG, Nordlander P, Aizpurua J. Bridging quantum and classical plasmonics with a quantum-corrected model. Nat Commun. 2012;3:825.
10. Scholl JA, García-Etxarri A, Koh AL, Dionne JA. Observation of quantum tunneling between two plasmonic nanoparticles. Nano Lett. 2012;13(2):564–9.
11. Duan H, Fernández-Domínguez AI, Bosman M, Maier SA, Yang JKW. Nanoplasmonics: classical down to the nanometer scale. Nano Lett. 2012;12(3):1683–9.
12. Henzie J, Andrews SC, Ling XY, Li Z, Yang P. Oriented assembly of polyhedral plasmonic nanoparticle clusters. Proc Natl Acad Sci. 2013;110(17):6640–5.
13. Tan SF, Wu L, Yang JKW, Bai P, Bosman M, Nijhuis CA. Quantum plasmon resonances controlled by molecular tunnel junctions. Science. 2014;343(6178):1496–9.

14. Salomon A, Cahen D, Lindsay S, Tomfohr J, Engelkes VB, Frisbie CD. Comparison of electronic transport measurements on organic molecules. Adv Mater. 2003;15(22):1881–90.
15. Reed MA, Zhou C, Muller CJ, Burgin TP, Tour JM. Conductance of a molecular junction. Science. 1997;278(5336):252–4.
16. Cui XD, Primak A, Zarate X, Tomfohr J, Sankey OF, Moore AL, Moore TA, Gust D, Nagahara LA, Lindsay SM. Changes in the electronic properties of a molecule when it is wired into a circuit. J Phys Chem B. 2002;106(34):8609–14.
17. Nijhuis CA, Reus WF, Barber JR, Whitesides GM. Comparison of SAM-based junctions with Ga2O3/EGaIn top electrodes to other large-area tunneling junctions. J Phys Chem C. 2012;116(26):14139–50.
18. Joachim C, Ratner MA. Molecular electronics: some views on transport junctions and beyond. Proc Natl Acad Sci USA. 2005;102(25):8801–8.
19. McCreery RL. Molecular electronic junctions. Chem Mater. 2004;16(23):4477–96.
20. Wu L, Duan H, Bai P, Bosman M, Yang JKW, Li E. Fowler-Nordheim tunneling induced charge transfer plasmons between nearly touching nanoparticles. ACS Nano. 2012;7(1):707–16.
21. Nelayah J, Kociak M, Stephan O, Garcia de Abajo FJ, Tence M, Henrard L, Taverna D, Pastoriza-Santos I, Liz-Marzan LM, Colliex C. Mapping surface plasmons on a single metallic nanoparticle. Nat Phys. 2007;3(5):348–53.
22. Michel B, Vicki JK, Masashi W, Abbas IM, Michael BC. Mapping surface plasmons at the nanometre scale with an electron beam. Nanotechnology. 2007;18(16):165505.
23. Bosman M, Ye E, Tan SF, Nijhuis CA, Yang JKW, Marty R, Mlayah A, Arbouet A, Girard C, Han M-Y. Surface plasmon damping quantified with an electron nanoprobe. Sci Rep. 2013;3.
24. Strange M, Rostgaard C, Häkkinen H, Thygesen KS. Self-consistent GW calculations of electronic transport in thiol- and amine-linked molecular junctions. Phys Rev B. 2011;83 (11):115108.
25. Reddy P, Jang S-Y, Segalman RA, Majumdar A. Thermoelectricity in molecular junctions. Science. 2007;315(5818):1568–71.
26. Xiao X, Xu B, Tao NJ. Measurement of single molecule conductance: benzenedithiol and benzenedimethanethiol. Nano Lett . 004;4(2):267–71.
27. Scheer AM, Gallup GA, Burrow PD. Unoccupied orbital energies of 1,4-benzenedithiol and the HOMO–LUMO gap. Chem Phys Lett. 2008;466(4–6):131–5.
28. Wold DJ, Frisbie CD. Formation of metal–molecule–metal tunnel junctions: microcontacts to alkanethiol monolayers with a conducting AFM tip. J Am Chem Soc. 2000;122(12):2970–1.
29. Wu S, Gonzalez MT, Huber R, Grunder S, Mayor M, Schonenberger C, Calame M. Molecular junctions based on aromatic coupling. Nat Nano. 2008;3(9):569–74.
30. Ho Choi S, Kim B, Frisbie CD. Electrical resistance of long conjugated molecular wires. Science. 2008;320(5882):1482–6.
31. Pontes RB, Rocha AR, Sanvito S, Fazzio A, da Silva AJR. Ab initio calculations of structural evolution and conductance of benzene-1,4-dithiol on gold leads. ACS Nano. 2011;5(2):795–804.
32. Palik ED. Handbook of optical constants of solids. San Diego, California: Academic; 1991.
33. Haynes WM. CRC handbook of chemistry and physics. 94th ed. Taylor and Francis; 2013.
34. Bosman M, Zhang L, Duan H, Tan SF, Nijhuis CA, Qiu CW, Yang JKW. Encapsulated annealing: enhancing the plasmon quality factor in lithographically–defined nanostructures. Sci Rep. 2014; 4.
35. Sellers H, Ulman A, Shnidman Y, Eilers JE. Structure and binding of alkanethiolates on gold and silver surfaces: implications for self-assembled monolayers. J Am Chem Soc. 1993;115 (21):9389–401.
36. Cox EG, Cruickshank DWJ, Smith JAS. The crystal structure of benzene at −3 °C. Proc Royal Soc Lon Ser A Math Phys Sci. 1958;247(1248):1–21.
37. Kiguchi MSN, Murakoshi K. In-situ preparation of a single molecular junction with mechanically controllable break junctions in vacuum. J Phys Conf Ser. 2008;100:052–059.

38. Kim Y, Pietsch T, Erbe A, Belzig W, Scheer E. Benzenedithiol: a broad-range single-channel molecular conductor. Nano Lett. 2011;11(9):3734–8.
39. García de Abajo FJ. Optical excitations in electron microscopy. Rev Mod Phys. 2010;82 (1):209–275.
40. Bigelow NW, Vaschillo A, Iberi V, Camden JP, Masiello DJ. Characterization of the electron- and photon-driven plasmonic excitations of metal nanorods. ACS Nano. 2012;6(8):7497–504.

Chapter 5
Stability of Silver and Gold Nanoparticles Under Electron Beam Irradiation

Abstract The STEM-EELS experiments that have been introduced in Chap. 4 were performed on closely-spaced gold nanocuboids as well. However, the high aspect ratio gaps degraded in many cases as a result of filament formation during electron beam irradiation. In this Chapter, a detailed study on the degradation mechanisms and preventive approaches is given, focusing in particular on the nanoparticle coatings that could act as a protective barrier for minimizing the electron beam induced damage on passivated gold and silver nanoparticles.

5.1 Introduction

Nanoparticles (NPs) with tunable surface properties are used in many applications, ranging from nanostructured catalysis, (quantum) plasmonics, to surface-enhanced Raman spectroscopy. The characterization of NPs often involves the utilization of transmission electron microscope (TEM) or scanning electron microscope (SEM) based techniques, but these techniques rely on high-energy electron beams which cause (un)wanted changes to the specimen such as degradation, radiolysis of surface molecules, contamination build-up, electron beam-induced atomic displacements, or heating. NPs have limited stability under these conditions and the mechanisms of electron beam-induced damages are poorly understood.

Passivated NPs are potential building blocks of novel devices and materials [1–4], so a better understanding of NP stability under analysis conditions would be useful to avoid drawing faulty conclusions from experimental observations. Here, an investigation is presented on whether different types of coatings on gold (Au) and silver (Ag) nanocuboids could prevent, or significantly reduce electron beam radiation damage [5]. These noble metal NPs are meta-stable and their morphology is usually stabilized by an organic monolayer such as cetyl trimethyl ammonium bromide (CTAB), self-assembled monolayers (SAMs) of thiolates or a polymer such as poly(vinylpyrrolidone) (PVP), ethylene glycol, etc. [5].

S. F. Tan, *Molecular Electronic Control Over Tunneling Charge Transfer Plasmons Modes*, Springer Theses, https://doi.org/10.1007/978-981-10-8803-2_5

Electron beam-induced damages and the preventive approaches reported in literature to minimize the effects were discussed in Chap. 2. Among the effects mentioned above, the knock-on damage and the ionization damage are critical for organic monolayer-coated inorganic NPs. Knock-on effects usually occur in conducting inorganic specimens [6] where the accelerating voltage of the incident electron beam is higher than the displacement energy of the material or when the electron dose exceeds 1000 C cm^{-2}. On the other hand, ionization damage is predominant for insulators, such as organic monolayer molecules in our study, at all incident energies (10–300 keV).

5.2 Results and Discussion

5.2.1 *Synthesis and Functionalization of Silver and Gold Nanocuboids*

We refer to Sect. 3.2.2, for the synthesis and functionalization of Ag nanocuboids. The experimental details of the synthetic procedures and characterization techniques are reported in the experimental section at end of Chap. 3.

Besides Ag, we shall also look at Au nanocuboids in this Chapter. For these, we followed the seed-mediated method developed by Sun et al. [7]. The experimental details of the synthetic procedures and characterization techniques are reported in the experimental section at end of this Chapter. Here, only a brief description is given.

The synthesis of Au nanocuboids was performed by a two-step method. First, a Au seed solution was prepared by rapid reduction of the Au precursor i.e.: chloroauric acid with a strong reducing agent sodium borohydride in the presence of surfactant CTAB. The seed solution contained quasi-spherical Au NPs of size less than 5 nm. In the second step, the seed was added into the growth solution which consisted of Au precursor, a mild reducing agent, i.e. ascorbic acid and a chemical additive: copper sulfate. Carefully controlling the concentration of each component enables the formation of Au nanocuboids stabilized with {100} facets.

The Ag and Au nanocuboids were functionalized with mixed SAMs of thiolates and ditholates and the polymer PVP, following the method described previously in Chap. 3.

5.2.2 *Tunneling CTP Between Gold Nanocuboids*

We performed monochromated STEM-EELS experiments (introduced in Chap. 4) on Au cuboids, with PDT as the SAM in the gap. Au is much more susceptible to

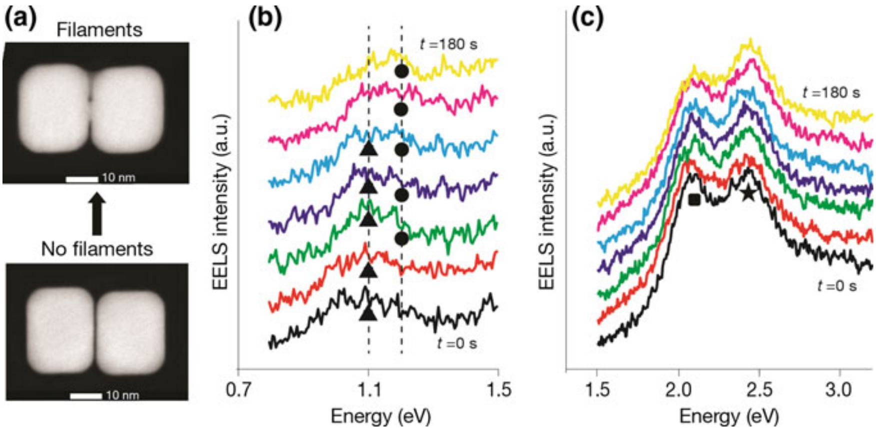

Fig. 5.1 **a** STEM images of the dimer recorded before and after EELS measurements. **b** Transition from the tunneling charge transfer (tCTP) mode at 1.05 eV (with a clean gap, labeled with filled triangle) to the conventional, non-tunneling CTP mode at 1.18 eV (when filaments are formed in the gap, labeled with filled circle), acquired over a 180 s time interval. **c** EELS spectra for the same data in the energy range of 1.5–3.0 eV. The ratio of the higher-energy peaks (labeled with filled square and filled star) changed from 1:0.9 to 1:1.6. The widening of the filament reduces the charge reflection at the gap and therefore lowers the bonding dipolar mode

electron beam-induced changes to the morphology, so imaging had to be performed in low-dose STEM mode. We could not obtain TEM images without inducing morphological changes to the Au in the gap due to the high dose exposure during TEM imaging.

Figure 5.1 shows a series of EELS measurements that were taken during the formation of filaments in the dimer gap. Before starting the monochromated EELS measurements, a low-dose STEM image was taken (at 200 kV, with a 0.2 nm probe) of the Au dimer; no filaments were observed in the 0.5–0.7 nm gap. Monochromated EELS was subsequently performed, starting with the black EELS spectrum in panel (b), and finishing 180 s later with the yellow spectrum.

Without further illuminating the dimer, another STEM image was taken at 200 kV (Fig. 5.1a, top panel), showing Au filaments that were formed in the gap. A close look at the low-energy peaks in panel (b) shows that there is a transition from the tCTP mode (filled triangle) to a conventional (non-tunneling) CTP (filled circle) mode during the cause of the EELS measurements when the filaments formed.

5.2.3 Filament Formation Between Closely-Spaced Gold Nanocuboids

To investigate the filament formation in more detail, a time-lapse series of TEM images (Fig. 5.2) was recorded where filament formation is observed between two Au nanocubes upon electron beam irradiation. The imaging is done on the mixed SAMs-coated Au nanocubes with 200 kV electrons, using electron doses ranging from 2000 to 2500 e/Å^2 s for 32 min.

Filament formation between two Au nanocubes was observed, in the following order. (1) Tiny filaments ($\sim$2–3 nm) form between the corners of each nanocube. (2) The filaments grow and fill up the whole gap gradually. (3) Two nanocubes are completely connected when the filaments have filled the whole gap.

In an attempt to avoid the filament formation, we functionalized the Au cuboids with the polymer PVP. PVP is a commonly used capping agents in NP synthesis because it selectively interacts with {100} facets and prevents the NP suspension to aggregate via steric repulsion resulting in kinetically (i.e., not thermodynamically) stable monocrystalline Ag nanocubes [8, 9]. It is worth noting that kinetic stability occurs in colloidal suspension, however, the situation for dried particles will likely to be different. Previous studies [9] suggested that as the layer of PVP was dried, it is likely that the polymer collapsed due to the removal of hydrogen bonding with water, causing the carbonyl groups to lay parallel to the metal surface. Here, we irradiated PVP and SAMs-coated Au nanocuboids with 200 kV electrons, with doses ranging from 100 to 1300 e/Å^2 s for 24 and 42 min, respectively, as shown in Fig. 5.3. We observed the filament formation between two thiolates-SAMs - coated Au nanocube dimer but not for the one with PVP coatings. Many studies [10–13] report that sintering of two NPs separated by 1–2 nm occurs when the atoms in the material diffuse across the surfaces of the particles, fusing the particles together to constitute one solid piece. Two sintering mechanisms are reported [14]:

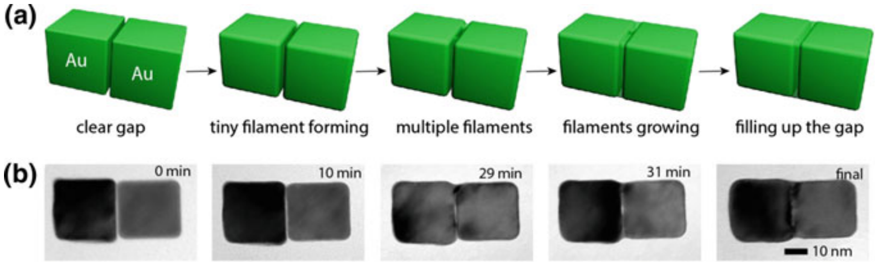

Fig. 5.2 **a** Schematic the filament formation between gold nanocubes coated with SAMs of thiolates under electron beam irradiation. (electron dose: 2000–2500 e/Å^2 s). **b** A time-lapse series of TEM images where filaments form and grow between two closely-spaced monocrystalline Au nanocuboids coated with SAMs on a copper grid. Eventually, the gap is filled completely and the two particles are merged. Figure reprinted from Ref. [5], with permission from American Chemical Society, Copyright 2017

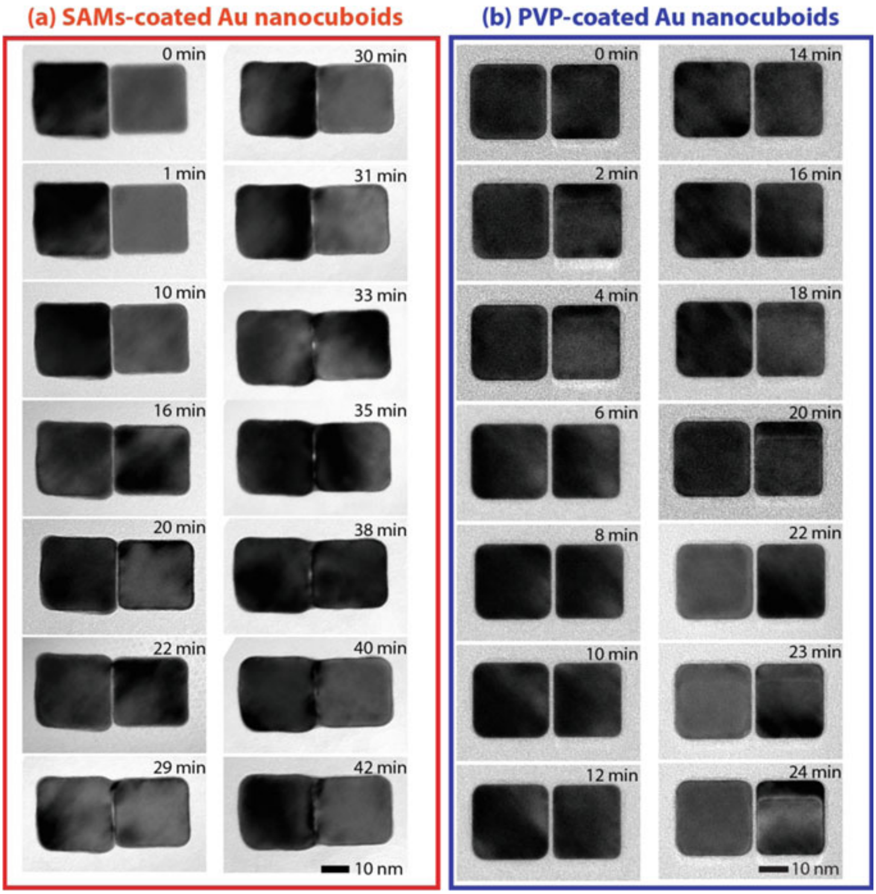

Fig. 5.3 **a**, **b** The sequence of high resolution transmission electron microscopy (TEM) images of filament formation of single-crystalline gold cube dimer coated with SAMs (electron dose: 2000–2500 e/Å^2 s) and PVP (electron dose for the first 20 min: 100–120 e/Å^2 s, after 20 min: 1100–1300 e/Å^2 s) on copper grid under electron beam irradiation

(1) Ostwald Ripening (2) Surface diffusion. Since the particles are not in solution, we suggest the latter case is dominant for the filament formation in this study.

However, this problem still persists even though we performed the same experiment at liquid nitrogen temperature by using a special cooling holder. It has been proposed that lowering the temperature would help in reducing the sensitivity of an organic species to structural damage and mass loss, even though it does not change the inelastic cross-section [15]. In this case, lowering the temperature does not help to slow down the subsequent diffusion processes but coating with long chain polymer does. Surprisingly, the polymer PVP acts as a diffusion barrier that could significantly minimize the possibility of the surface diffusion driven filament formation. It is well-known that the ring-containing chemical species (PVP) would be more resistant than the aliphatic molecules (alkanethiolate SAMs) towards electron beam induced damage since the irreversible bond scissions will require higher energy [16]. This shows that the ligands stability is crucial in protecting the metal NPs against the electron beam.

5.2.4 The Role of Ligands

We now replace Au nanocuboids with Ag nanocubes. It is well-known that Ag is harder than Au (Vickers hardness Ag = 251 MN/m^2, Au = 216 MN/m^2). However, the displacement (E_d) and sputtering (E_s) threshold energies of Ag (E_d and E_s are 28 and 7–14 eV respectively) are lower than those of Au (E_d and E_s are 36 and 9–18 eV respectively) [17].

Figure 5.4a schematically illustrates the deformation of a Ag nanocube coated with a mixed SAM of 1-propanethiolate and 1,2-ethanedithiolate (volume ratio of 5:3) with a thickness of 0.5 nm while irradiated on a SiN$_x$ membrane with an electron beam of 200 kV with electron doses ranging from 100 to 3000 e/Å^2 s. Figure 5.4b shows the sequence of TEM acquired images, along with the corresponding fast Fourier Transforms, of a single Ag nanocube recorded at intervals of 2 min over a period of 27 min (after which the experiment was stopped).

During the first 6 min, the particle morphology did not change noticeably, but at t = 6 min protrusions formed at the faces of the nanocube (indicated by red triangles). These protrusions have lower contrast than the rest of the particle and therefore they are probably thinner than the cubic NP. The monocrystalline FCC crystal structure of the original particle remains visible up to t = 22 min, but the final state is a quasi-spherical, polycrystalline FCC Ag NP.

The degradation started from the top or bottom faces of the nanocube where we observed a contrast change (green triangles), subsequently the newly-formed protrusions (red triangle) emerged at the corners and edges. At the same time, the size of the Ag nanocube shrank and its corners became more and more truncated.

After 10 min, we observed a new lattice reflection spot emerged which arising from the (111) reflection originated from FCC Ag protrusions. From this experiment, we conclude that mixed SAMs do not stabilize the Ag nanocube under high e-beam irradiation.

A similar experiment was performed by drop-casting the as-synthesized, PVP-coated Ag nanocubes onto the 30 nm thick silicon nitride (SiN$_x$) membrane. To investigate whether PVP also stabilizes the NPs during a typical TEM experiment, we irradiated PVP-coated Ag nanocubes with 200 kV electrons, with doses ranging from 1100 to 2000 e/Å^2 s for 20 min.

Figure 5.5 shows a sequence of TEM images of a single Ag nanocube coated with PVP. At t = 0, the particle had a PVP layer of 2.8 nm thickness, appearing in the images as a slight change in contrast around the nanocube. During the entire course of the experiment, the Ag particle remained stable and no obvious changes

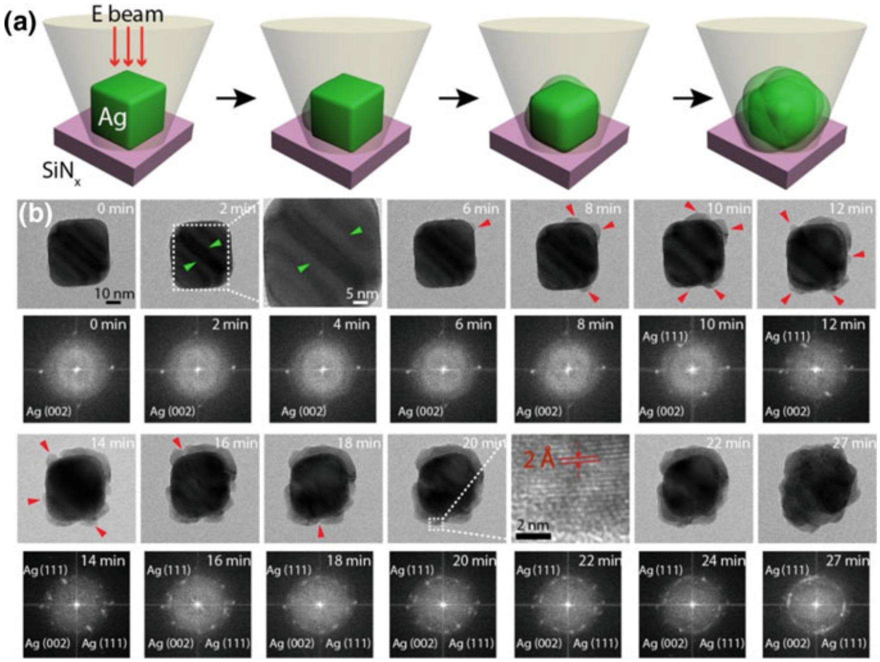

Fig. 5.4 **a** Schematic the deformation of silver nanocube coated with SAMs of thiolates under electron beam irradiation. **b** Sequence of high resolution transmission electron microscopy (TEM) and the corresponding Fast Fourier Transforms of a single-crystalline silver cube coated with SAMs on SiN$_x$ membrane, during electron beam irradiation (electron dose: 1500–2000 e/Å^2 s), where a cube-shaped particle evolves to an irregular quasi-spherical particle. Figure reprinted from Ref. [5], with permission from American Chemical Society, Copyright 2017

in shape or phase were observed, but the organic layer surrounding the particle increased in thickness from 2.8 to 6.1 nm.

We attribute this increase in the thickness to the electron-beam-induced build-up of organic contamination. Contamination in electron microscopy often refers to the electron beam induced deposition (EBID) where there is an interaction between the electron beam and organic matter [18, 19], i.e., PVP in our case. The PVP tends to crosslink and form structures on the sample that are clearly visible in TEM images [20] as seen in Fig. 5.5. Muller et al. [21] also reported that the non-conducting electron beam-induced carbon contamination layers can possibly act as both diffusion and sputtering barrier, thereby preventing structural damage. From this experiment, we conclude that a thin PVP coating, unlike SAMs, stabilizes the Ag nanocubes during electron-beam irradiation. This is probably due to the stability of the molecules against electron beam irradiation and, hence, we conclude that monolayers of thiolates can easily suffer from ionization damage but polymers like PVP which are thicker than the monolayer thiolates tend to be stable against ionization damage induced by the electron beam.

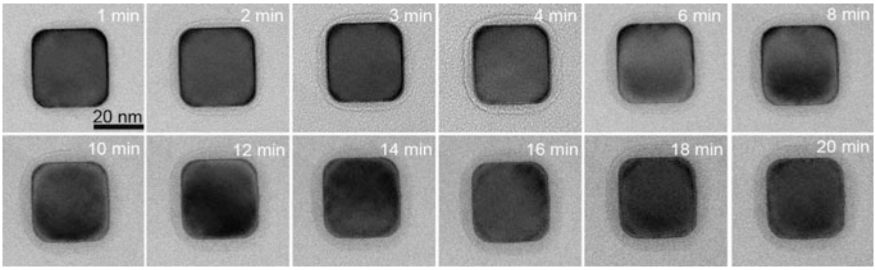

Fig. 5.5 Sequence of TEM images of a monocrystalline silver cube coated with polymer (polyvinylpyrrolidone) on a SiN_x membrane, during electron beam irradiation (electron dose: 1100–2000 e/$Å^2$ s). The cubical-shaped was maintained throughout the whole illumination period. Figure reprinted from Ref. [5], with permission from American Chemical Society, Copyright 2017

From experiments above, we infer that PVP-coated Ag nanocubes are stable against electron beam irradiation but mixed SAMs- coated ones are not. To further understand the degradation mechanism, we performed the same experiment on dimers with the two types of coatings. Figure 5.6 shows the effect of electron beam irradiation on a dimer of Ag nanocubes coated with SAMs of thiolates (Fig. 5.6a) and with PVP (Fig. 5.6b).

We make the following three observations for the dimer coated with SAMs. (1) During electron beam irradiation, the degradation starts from the centre of the cube (green triangles) where we observe a contrast change. (2) Subsequently, newly-formed protrusions emerge at the corners and edges. (3) At the same time, the Ag nanocubes become more and more truncated and finally turn into rounded nanocubes. The observed phenomena for the Ag nanocubes dimers are similar to those of single silver nanocubes functionalized with thiolated-SAMs. In other words, when we observe degradation of single particles, they will also occur on dimers, and when single particles are stable, so are dimers.

Chen et al. [14] reported that the sintering behavior of NPs is dependent on the stability of the molecules against electron beam damage. Thus, the extent of electron beam-induced damage depends on the ability of the molecules to stabilize the surface atoms even while they are being bombarded by fast electrons. Here, we observed the degradation, i.e., formation of Ag protrusions between two NPs for the case of thiolates-coated nanocube dimers while the NPs coated with PVP still maintained their good square shape. The interaction between PVP and Ag NPs is thought to occur between the Ag atoms and the carbonyl group located on the pyrrolidone ring [22] (Fig. 5.7c–d) while the monolayer of thiolates molecules bind to the Ag NPs via an Ag-S covalent bond [23] (Fig. 5.7a–b). It is well-known that energy transferred during inelastic scattering would cause heating within the specimen and the temperature rise in an organic specimen can reach a few hundred degrees for a stationary probe [24]. We speculate that the heating caused by the

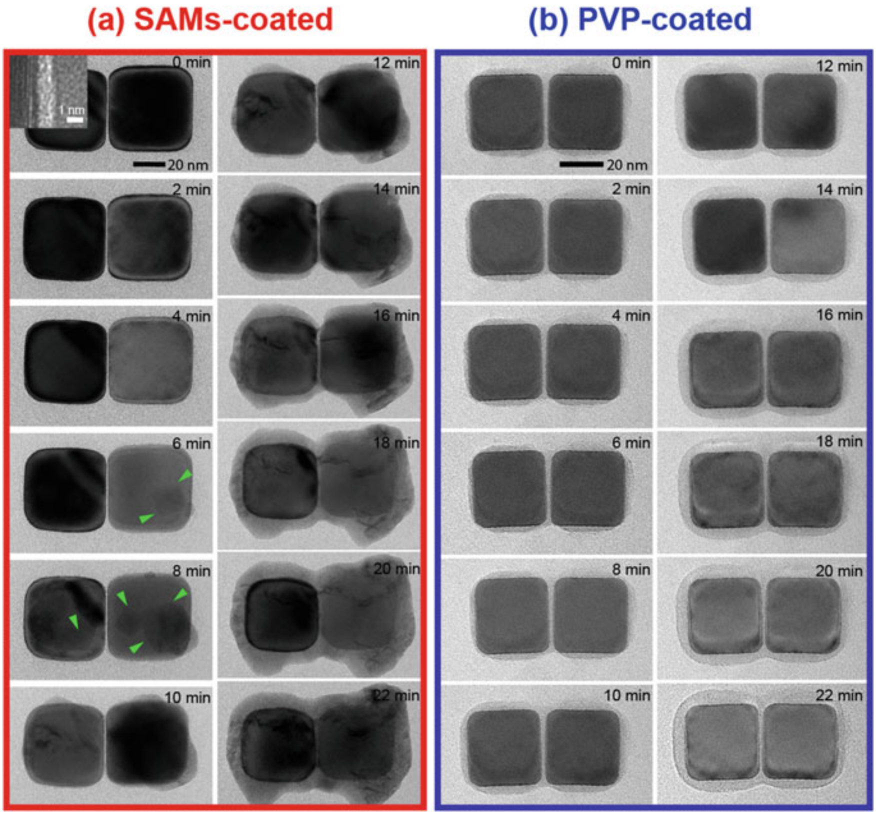

Fig. 5.6 **a**, **b** A comparison between SAMs-coated and polymer-coated silver nanocubes dimers. Two sequences of TEM images are shown with monocrystalline silver cube dimers, coated with either SAMs (thiolates) or with a polymer (PVP) on a SiN_x membrane under electron beam irradiation (electron dose: 1500–2000 e/Å^2 s). Figure reprinted from Ref. [5], with permission from American Chemical Society, Copyright 2017

electron beam degrades both the ligands (SAMs and the PVP molecules) in different ways. Our observations show that thiolated SAMs lead to a more rapid growth of the protrusions (Fig. 5.6a), especially along the interface with the SiN_x membrane. In effect, the particle is 'bleeding away' surface atoms that spread-out over the SiN_x membrane.

On the other hand, thermal degradation of PVP is accompanied by the release of pyrrolidone rings as reported before [22, 25, 26]. This surprisingly results in pyrrolidone rings that bind in a bridging, side-on fashion, more strongly absorbed on the NP surface than units that are only singly coordinated. A schematic of this bidentate ligand is shown in Fig. 5.7e–f. Although the bond strength of metal-sulfur (Ag-S) covalent bond is stronger than the singly coordination bond [9, 23], the bidentate coordination bond formation as a result of interface heating caused by

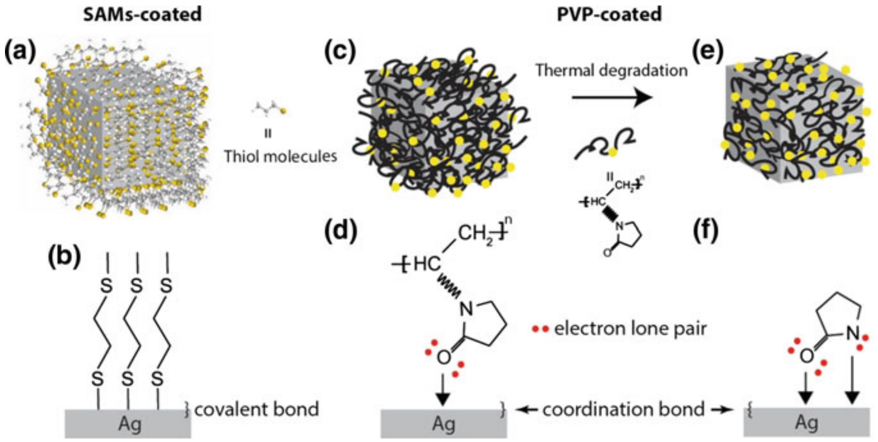

Fig. 5.7 Illustration of **a** thiolated SAMs and **b** bonding to the metal nanoparticles. Schematic of the PVP coating at the nanoparticle surface and the bonding to Ag nanocubes **c**, **d** before (monodentate ligand) and **e**, **f** (bidentate ligand) after thermal degradation (model adapted from Borodko et al. [22])

electron beam irradition may be the reason for PVP-coated particles to be well-protected against electron beam irradiation. Even though the exact mechanism is not elucidated here, the results were reproducible and practically useful enough to include PVP coating to stabilize our NPs in TEM experiments.

5.3 Conclusions

In short, surface diffusion driven filament formation is an important factor to consider for the TEM study of passivated Au NPs. For passivated Ag nanoparticle on the other hand, electron beam-induced heating at metal-ligand interface appears to be the main degradation mechanism. We have demonstrated the important role of ligands in maintaining the shape of Au and Ag nanocubes under TEM electron beam irradiation.

SAMs of thiolates molecules have very low stability in protecting NPs against electron beam damage while coating the particles with polymers such as PVP may evolve as a new method for stabilization in order to improve the lifetime of plasmonic devices and materials under characterization conditions.

5.4 Experimental Section

5.4.1 General Procedures

For the Ag nanocubes, the chemicals poly(vinyl)pyrrolidone (PVP), silver nitrate, 1,2-ethanedithiol (EDT), 1,4-benzenedithiol (BDT) were all purchased from Sigma-Aldrich and used without further purification. Sodium sulfide and ethylene glycol were purchased from J. T. Baker. For the nanocuboids, the chemicals 1-butanethiol (BT), 1,3-propanedithiol (PDT), gold (ɪɪɪ) chloride trihydrate, sodium borohydride, cetyltrimethylammonium bromide (CTAB), copper sulfate, L-ascorbic acid were all purchased from Sigma-Aldrich and used without further purification. The glass vials used for synthesis were obtained from Fisher Scientific. Solvents for NPs functionalization were freshly distilled prior to use. All stirrer bars were soaked in aqua-regia (mixture of 1:3 volume ratio of nitric acid: hydrochloric acid) for at least 1 h, washed with deionized water (18.2 Ω cm) and dried in an oven before use. NPs were washed in Rotina (model 380R) and Profuge (model 14D) centrifuges.

5.4.2 Synthesis of Silver Nanocubes

Refer to Sect. 3.4.

5.4.3 Functionalization of Silver Nanocubes with Mixed SAMs

Refer to Sect. 3.4.

5.4.4 Synthesis of Gold Nanocubes

We followed the seed-mediated method [7] developed by Sun et al. A gold seed solution was prepared by reducing 6.25 ml of $HAuCl_4 \cdot 3H_2O$ (1.0 mM) with 0.15 ml of ice-cold sodium borohydride aqueous solution ($NaBH_4$, 0.1 M) in the presence of 18.75 ml of cetyltrimethylammonium bromide aqueous solution (CTAB, 0.1 M). The $NaBH_4$ solution was added at once to a solution containing CTAB and Au precursor. We left the reaction mixture to stir for 4 h at room temperature before proceeding to the next step. For the growth solution of Au nanocuboids, 20.0 ml of CTAB (0.02 M) was added to a clean polypropylene tube, followed by the addition of 5.0 ml of $HAuCl_4 \cdot 3H_2O$ (2.0 mM) aqueous solution. Then we added 50 µl of copper sulfate ($CuSO_4$, 0.01 M) aqueous solution, 3.0 ml of L-ascorbic acid (L-AA, 0.1 M) and 5.0 µl of Au seed solution sequentially. The solution was gently mixed by inversion of the test tube after the addition of each component.

5.4.5 Functionalization of Gold Nanocubes with Mixed SAMs

The Au nanocuboids solution was subjected to three times of washing treatment by centrifugation and re-dispersion in order to minimize the concentration of CTAB surfactant molecules before functionalization. Specifically, 1.5 µl of 1-butanethiol (BT) solution (1.0 mM in CH_3CN:H_2O mixture of 4:1) and 1.5 µl of 1,3-propanedithiol (PDT) solution (1.0 µM in CH_3CN:H_2O mixture of 4:1) was added into 2.0 ml of CH_3CN:H_2O mixture of 4:1. Subsequently, 0.38 ml of 0.12 nM Au nanocuboids solution was added into the mixture and stirred for 30 min. The reaction mixture was washed with CH_3CN:H_2O mixture of 4:1 once and re-dispersed in the same solvent mixture. Finally, 3.0 µl of the mixture was drop-cast onto a SiN_x membrane (30 nm-thick, S1N1 Agar Scientific) and copper grid.

5.4.6 Functionalization of Gold Nanocubes with PVP

The Au nanocuboids solution was subjected to three times of washing treatment by centrifugation and re-dispersion in order to minimize the concentration of CTAB surfactant molecules before functionalization. Then, 30 mg/ml of aqueous PVP solution was added into the as-washed nanocubes solution for 2 h at room temperature. Finally, 3.0 µl of the mixture was drop-casted onto a silicon nitride membrane SiN_x (30 nm-thick, S1N1 Agar Scientific) and copper grid.

5.4.7 EELS Measurements

Refer to Sect. 4.2.2.

5.4.8 Imaging Techniques

The time-lapse TEM images were acquired with high-resolution FEI Titan and JEOL2010FEG transmission electron microscopes operating at 200 kV with electron doses ranging from 100 to 3000 e/Å^2 s. We imaged at a rate of 10–25 frames per second for the Au nanocubes experiments, 1–2 frames per minute for the Ag nanocubes experiments with ORIUS SC200 (Gatan, Inc.) CCD camera.

References

1. Wang Y, Zhou Y, Sokolov J, Rigas B, Levon K, Rafailovich M. A potentiometric protein sensor built with surface molecular imprinting method. Biosens Bioelectron. 2008;24(1):162–6.
2. Chen H, Heng CK, Puiu PD, Zhou XD, Lee AC, Lim TM, Tan SN. Detection of Saccharomyces cerevisiae immobilized on self-assembled monolayer (SAM) of alkanethiolate using electrochemical impedance spectroscopy. Anal Chim Acta. 2005;554(1–2):52–9.
3. Huang TJ, Brough B, Ho C-M, Liu Y, Flood AH, Bonvallet PA, Tseng H-R, Stoddart JF, Baller M, Magonov S. A nanomechanical device based on linear molecular motors. Appl Phys Lett. 2004;85(22):5391–3.
4. Barfidokht A, Ciampi S, Luais E, Darwish N, Gooding JJ. Distance-dependent electron transfer at passivated electrodes decorated by gold nanoparticles. Anal Chem. 2013;85(2):1073–80.
5. Tan SF, Bosman M, Nijhuis CA. Molecular coatings for stabilizing silver and gold nanocubes under electron beam irradiation. Langmuir. 2017;33(5):1189–96.
6. Egerton RF. Mechanisms of radiation damage in beam-sensitive specimens, for TEM accelerating voltages between 10 and 300 kV. Microsc Res Tech. 2012;75(11):1550–6.
7. Sun J, Guan M, Shang T, Gao C, Xu Z, Zhu J. Selective synthesis of gold cuboid and decahedral nanoparticles regulated and controlled by Cu^{2+} Ions. Cryst Growth Des. 2008;8(3):906–10.
8. Skrabalak SE, Au L, Li X, Xia Y. Facile synthesis of Ag nanocubes and Au nanocages. Nat Protocols. 2007;2(9):2182–90.
9. Moran CH, Rycenga M, Zhang Q, Xia Y. Replacement of poly(vinyl pyrrolidone) by thiols: a systematic study of Ag nanocube functionalization by surface-enhanced Raman scattering. J Phys Chem C. 2011;115(44):21852–7.
10. Scholl JA, García-Etxarri A, Koh AL, Dionne JA. Observation of quantum tunneling between two plasmonic nanoparticles. Nano Lett. 2012;13(2):564–9.
11. Surrey A, Pohl D, Schultz L, Rellinghaus B. Quantitative measurement of the surface self-diffusion on Au nanoparticles by aberration-corrected transmission electron microscopy. Nano Lett. 2012;12(12):6071–7.
12. Flüeli M, Buffat PA, Borel JP. Real time observation by high resolution electron microscopy (HREM) of the coalescence of small gold particles in the electron beam. Surf Sci. 1988;202(1–2):343–53.
13. Lim TH, McCarthy D, Hendy SC, Stevens KJ, Brown SA, Tilley RD. Real-time TEM and kinetic Monte Carlo studies of the coalescence of decahedral gold nanoparticles. ACS Nano. 2009;3(11):3809–13.
14. Chen Y, Palmer RE, Wilcoxon JP. Sintering of passivated gold nanoparticles under the electron beam. Langmuir. 2006;22(6):2851–5.
15. Cryoprotection in electron microscopy. J Microsc. 1986;141(3):385–91.

16. Hadermann J. High-resolution electron microscopy (John C. H. Spence, Oxford University Press, 2013, p. 406. Price [pound sign] 75). Acta Crystallograp Sect B. 2014;70(4):778. ISBN: 978-0-19-966863-2.
17. Williams DBCCB. Transmission electron microscopy: a textbook for materials science. 2nd ed. USA: Springer, US; 2009.
18. Randolph SJ, Fowlkes JD, Rack PD. Focused, nanoscale electron-beam-induced deposition and etching. Crit Rev Solid State Mater Sci. 2006;31(3):55–89.
19. Soong C, Woo P, Hoyle D. Contamination cleaning of TEM/SEM samples with the ZONE cleaner. Microsc Today. 2012;20(06):44–8.
20. Egerton RF, Li P, Malac M. Radiation damage in the TEM and SEM. Micron. 2004;35 (6):399–409.
21. Muller DA, Silcox J. Radiation damage of Ni_3Al by 100 keV electrons. Philos Mag A. 1995;71(6):1375–87.
22. Borodko Y, Humphrey SM, Tilley TD, Frei H, Somorjai GA. Charge-transfer interaction of poly(vinylpyrrolidone) with platinum and rhodium nanoparticles. J Phys Chem C. 2007;111 (17):6288–95.
23. Love JC, Estroff LA, Kriebel JK, Nuzzo RG, Whitesides GM. Self-assembled monolayers of thiolates on metals as a form of nanotechnology. Chem Rev. 2005;105(4):1103–70.
24. Li P. Electron irradiation damage to organic light-emitting materials. Canada: University of Alberta; 2003.
25. Borodko Y, Habas SE, Koebel M, Yang P, Frei H, Somorjai GA. Probing the interaction of poly(vinylpyrrolidone) with platinum nanocrystals by UV–Raman and FTIR. J Phys Chem B. 2006;110(46):23052–9.
26. Peniche C, Zaldívar D, Pazos M, Páz S, Bulay A, Román JS. Study of the thermal degradation of poly(*N*-vinyl-2-pyrrolidone) by thermogravimetry—FTIR. J Appl Polym Sci. 1993;50 (3):485–93.

Chapter 6
Real-Time Imaging of Chemical Reactions Between Silver and Gold Nanoparticles

Abstract In this Chapter, a study on the galvanic replacement reaction of silver nanocubes in dilute, aqueous ethylenediaminetetraacetic acid (EDTA)-capped gold aurate solutions using *in situ* liquid-cell electron microscopy will be demonstrated. Au/Ag etched nanostructures with concave faces are formed via (1) etching that starts from the faces of the nanocubes followed by (2) the deposition of a gold layer as a result of galvanic replacement, and (3) gold deposition via particle coalescence where small nanoparticles are formed during the reaction as a result of radiolysis. Analysis of the silver removal rate and gold deposition rate provides a quantitative picture of the growth process and shows that the morphology and composition of the final product are dependent on the stoichiometric ratio between gold and silver.

6.1 Introduction

The formation and reaction dynamics during chemical synthesis or transformation of nanoparticles (NPs) in solution have been widely studied using *ex situ* methods. A popular method is the so-called 'quench-and-look' approach, where the reaction is stopped at various stages, after which the intermediate reaction products are imaged with transmission electron microscopy (TEM). This approach yields detailed information regarding the structure of the (intermediate) reaction products, but early stages of the reaction or fast reactions cannot be tracked. Also unknown is the way in which the sample preparation, i.e., quenching, drop-casting, drying, etc., affects the reaction. These limitations complicate mechanistic studies of NP structural evolution and related reactions including galvanic replacement, core-shell particle, or the formation of particles with well-defined shapes.

Using *in situ* imaging in liquid-cell mounted inside a TEM, we directly follow in real-time the galvanic replacement reaction between silver (Ag) nanocubes and chloroauric acid in aqueous medium [1]. We found that this reaction is fast and is completed within minutes, faster than the sample preparation and loading time of ~5 mins, preventing the observation of the early stages of the reaction. Adding the chelating ligand ethylenediaminetetraacetic acid (EDTA) to the reaction mixture

S. F. Tan, *Molecular Electronic Control Over Tunneling Charge Transfer Plasmons Modes*, Springer Theses, https://doi.org/10.1007/978-981-10-8803-2_6

prior to the addition of the Ag nanocubes made it possible to follow the reaction over a longer (7–10 mins) period of time because EDTA is able to form complexes with gold ions [1].

In this Chapter, we show a new mechanistic pathway where the aurate etched the Ag nanocubes' faces, making them bowl-shaped, while simultaneously a layer of gold (Au) was deposited onto the Ag nanocube as a result of galvanic replacement. In parallel, gold was also deposited via coalescence and monomer attachment as small Au nanoparticles formed during the reaction as a result of radiolysis. These results help to understand the mechanisms of NP growth by galvanic replacement reactions, where the morphology and composition are governed by a subtle change in local stoichiometry, which is useful for field of material engineering and metallic microscopic corrosion.

Galvanic replacement reactions are based on the principle that metal ions with higher oxidation potentials undergo reduction by oxidizing the metal present on the NPs [2–6]. In this study, we focus on the galvanic replacement between Ag nanocubes and aurate for which the following mechanism has been proposed by Sun et al. [2]. The standard reduction potential of $AuCl_4^-/Au$ (0.99 V vs. standard hydrogen electrode, SHE) and $AuCl_2^-/Au$ (1.11 V vs. SHE) is higher than that of Ag^+/Ag (0.80 V vs. SHE) and consequently, the galvanic replacement of Ag by Au (Eqs. 6.1 and 6.2) is thermodynamically favorable and spontaneous.

$$3\mathrm{Ag}\ (\mathrm{s}) + \mathrm{AuCl}_4^-\ (\mathrm{aq}) \rightarrow \mathrm{Au}\ (\mathrm{s}) + 3\mathrm{AgCl}\ (\mathrm{s}) + \mathrm{Cl}^-\ (\mathrm{aq}) \tag{6.1}$$

$$\mathrm{Ag}\ (\mathrm{s}) + \mathrm{AuCl}_2^-\ (\mathrm{aq}) \rightarrow \mathrm{Au}\ (\mathrm{s}) + \mathrm{AgCl}\ (\mathrm{s}) + \mathrm{Cl}^-\ (\mathrm{aq}) \tag{6.2}$$

Sun et al. [2] identified three distinct steps in the reaction of Ag nanostructures with chloroauric acid ($HAuCl_4$) by *ex situ* TEM imaging: first, pinholes form in the Ag nanocubes via etching of the Ag by the gold aurate, then the Ag nanocubes dissolve and an Au–Ag alloy forms on the walls of the nanocubes. Finally, the particles de-alloy followed by growth of the Au layer at the expense of the Ag till finally the hollow Au structures are formed (i.e., hollow nanocages). Moreover, Au et al. [7] investigated the effect of the reaction stoichiometric ratio by replacing the $AuCl_4^-$ with $AuCl_2^-$. They reported that Ag nanocubes reacting with $AuCl_2^-$ at an early stage produce nanoboxes and eventually form nanoframes without the dealloying step. They observed a molar ratio of 1:1 between generated Au and consumed Ag, i.e., more Au was deposited per oxidized Ag atom in the reaction with $AuCl_2^-$ than in the reaction with $AuCl_4^-$.

In order to understand the dynamic processes of galvanic replacement, high-resolution imaging and quantitatively analyzing the morphological and structural changes of the Ag nanocubes in this galvanic replacement reaction are needed.

6.2 Results and Discussion

6.2.1 The Attempt to Slow Down the Reactions

Refer to Sect. 3.2.2 for synthesis of the Ag nanocubes used in this Chapter. The experimental detail of the synthetic procedures is reported in the experimental section at end of Chap. 3.

To investigate the mechanism of the galvanic replacement reaction of Ag by aurate, we used a combination of *in situ* TEM imaging and *ex situ* characterization techniques such as post-mortem TEM imaging, energy-dispersive X-ray spectroscopy (EDX), scanning TEM (STEM)-tomography, etc., to study the structure, morphology and composition variation of the nanostructures in detail [1]. For the *ex situ* measurements, we typically added 5 μl of 10 mM $HAuCl_4$ at once to react with a 1 ml ~ 0.7 nM Ag nanocube suspension, following the reaction kinetics by UV-Vis spectroscopy. The absorbance value of the Ag nanocube suspension at a wavelength of 419 nm dropped by 80% of its initial value within 1 min. Since the time required to inject the reaction mixture into the liquid-cell, mount the liquid-cell into the TEM, and start imaging is ~5 min, we could not observe the early stages of the reaction. To lower the reaction rate, we added the chelating ligand EDTA that readily binds to metal cations [8]. At the same volume ratio of $HAuCl_4$ and Ag nanocubes as stated above, the reaction was slowed down in the presence of 10 mM EDTA where the absorbance value of the Ag nanocube suspension decreased merely 20% of its initial value within one minute.

Figure 6.1a shows the UV-vis spectra of Ag nanocubes solution before (green curve) and after interacting with gold ions solution with EDTA (red curve) and without EDTA (black curve) while Fig. 6.1b shows the plot of intensities *versus* time. In the absence of EDTA, the absorbance value at 419 nm dropped to ~20%

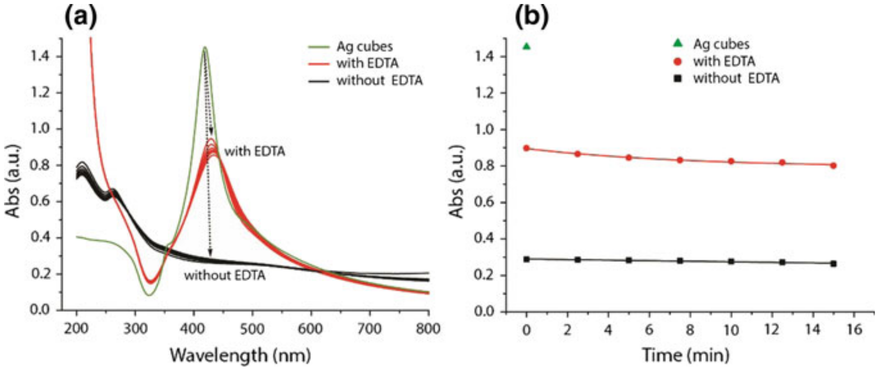

Fig. 6.1 **a** UV-vis spectra of Ag nanocubes solution before (green curve) and after interacting with gold ions solution with EDTA (red curve) and without EDTA (black curve). **b** The plot of absorbance intensities *versus* time. Each spectrum was recorded every 2 mins

of its initial value within 2 mins. With EDTA, absorbance value at 419 nm dropped to ~80% of its initial value within 2 mins. This proves that EDTA plays a role in slowing down the reaction rate between Ag nanocubes and gold ions.

6.2.2 In Situ Observation of Galvanic Replacement Reactions

Figure 6.2a shows a time (t, in s) series of TEM images from a single Ag nanocube reacting with the gold aurate solution inside a liquid-cell. The EDTA-capped gold ions etch the faces of the Ag nanocube, resulting in bowl-shaped faces. Figure 6.2b illustrates this process schematically. At $t = 0$ s, the Ag nanocubes and small particles (encircled in red) are visible. As the small NPs were repelled from the electron beam too fast for analysis at the dry state, we were not able to measure their chemical composition but we suggest that these are small Au that formed via radiolysis (i.e., reduction of Au^{3+} by solvated electrons). The image recorded at $t = 4.7$ s, and the subsequent images, show that one of these nanoparticles slowly disappears. We propose that the small Au NPs disappear and that the Au is deposited on Ag cubes via particle coalescence and a monomer attachment process. In addition, these images show that the volume of the nanocube increases during the reaction (indicated by the red and green arrows).

Figure 6.2c,d shows the evolution of the particle volume V (in nm^3) which is associated with the removal of Ag and deposition of Au for five particles as a function of the reaction time (see Sect. 6.4 for volume estimation details). We observe two time domains with distinct reaction kinetics: from $t = 0$ s to $t = 6$ s (blue colour region) and from $t = 7$ s to $t = 14$ s (red colour region), we fitted all five curves to an exponential function, with the volume depletion or growth equal to Eq. 6.3.

$$V = V_0 e^{-kt}, \tag{6.3}$$

where V_0 is the initial volume of the nanocube (nm^3) and k is the rate constant (s^{-1}). The dotted lines represent fits to Eq. 6.3. For all five data sets from $t = 0$ s to $t = 6$ s (blue color region), simple exponential regression estimates k to be $-0.02 \pm 0.01\ s^{-1}$ for Ag removal and $0.12 \pm 0.09\ s^{-1}$ for Au deposition. The indicated errors represent the standard deviation from five independent measurements.

The order of the reaction tells us how the rate of the reaction varies with respect to the reactant concentration. Overall, the reaction order is two (first order with respect to Ag nanocubes and gold aurate). For both regions, the rate of removal of Ag and deposition of Au show linearly dependent on the Ag nanocube and aurate concentration respectively. Although the removal rate of Ag is expected to be faster

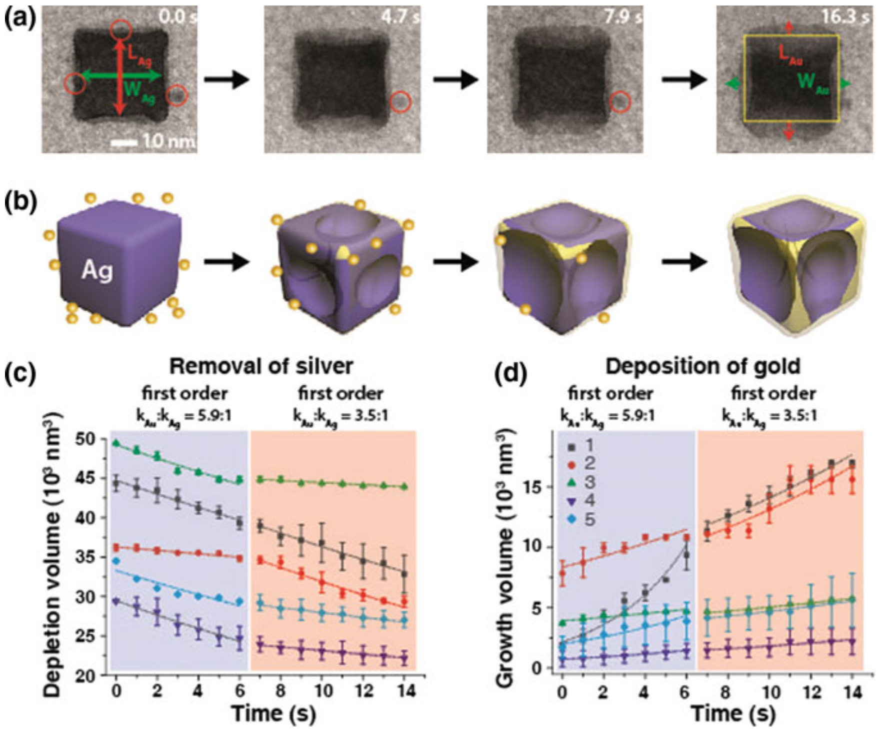

Fig. 6.2 **a** Time-lapse TEM images showing a silver nanocube interacting with the gold aurate solution inside a liquid-cell. **b** Schematic of the galvanic replacement reaction between silver nanocubes and EDTA-capped gold ions solution. Evolution of the particle volume depletion/growth rate as a function of time: **c** removal of silver and **d** deposition of gold. Blue color region indicates faster initial reaction kinetics in comparison with the later red color region. Figure reprinted from Ref. [1], with permission from American Chemical Society, Copyright 2016

than the deposition rate of Au since the estimated molar ratio of Au deposition *versus* Ag removal, M_{Ag}:M_{Au} would be 3:1, according to Eq. 6.1, three equivalents of Ag atoms are required to reduce one equivalent of Au^{3+} to metallic Au. However, our results show that the rate constant ratio of Ag:Au is 1:5.9 where the deposition rate of Au is faster than the depletion rate of Ag. This also explains in our experiments the absence of pinholes which serve as a pit for Ag removal, as reported elsewhere [7]. In our experiment, the Ag removal is much slower than the Au deposition due to three factors: the electron beam, the presence of EDTA and the presence of Ag atoms in the galvanic replacement reaction. For the time domain $t = 7$ s to $t = 14$ s (red coloured region), k is calculated to be -0.015 ± 0.01 s^{-1} for Ag removal and 0.05 ± 0.01 s^{-1} for Au deposition. Our results show that the rate constant ratio of Ag:Au is 1:3.5 where the deposition rate of Au is faster than the depletion rate of Ag, similar to the first time interval.

We attribute this discrepancy in molar ratio to the two reactions that happen in parallel: galvanic replacement and growth of a Au layer via particle coalescence and monomer attachment process. We believe that the excessive Au deposition results in the formation of Au NPs via reduction of $AuCl_4^-$ to Au^0 through radiolysis [9]. This hypothesis also explains the formation of the small Au NPs shown in Fig. 6.2a as described above. In addition, the solvated electrons readily reduce Au^{3+} to Au^+, thereby changing the stoichiometric ratio in Eqs. 6.1 and 6.2.

6.2.3 The Role of EDTA Ligands

The TEM images in Fig. 6.3a, c shows the control experiments of Ag nanocubes performed with and without EDTA-capped gold ions solution respectively. The Ag nanocubes were transformed into porous (*alloy*) nanocages without the presence of EDTA. In the presence of EDTA, the Ag nanocubes were etched from the edges, a layer of Au was deposited surrounding the nanocube during the galvanic replacement reaction as shown in Fig. 6.3c. Without the presence of chloroauric acid, EDTA itself is unable to induce any chemical reaction, therefore the nanocubes still maintain its shape as shown in Fig. 6.3b.

In order to investigate the role of EDTA in this gold-silver galvanic replacement reaction, the EDTA and chloroauric solutions were mixed for 5, 8, and 10 mins, before subsequent addition of Ag nanocubes solution. Different extent of *etching* of Ag nanocube was observed for different reaction times of EDTA with gold ions as shown in Fig. 6.3d–f. The extent of etching is the less when the reaction time between EDTA and gold ions is longer and vice versa. From this observation, we conclude that the chelating behavior of EDTA to gold ions is significant.

We prepared the SEM samples by spinning down the Ag NPs suspension with centrifuge after reacting with EDTA-capped gold ions aqueous solution for 30 mins, and subsequently spin-coated them onto a silicon wafer substrate. Unlike the previously reported isolation method [3] where they treated the suspension with NaCl in order to get rid of AgCl before centrifugation. However, due to the limitation of SEM technique, we are not able to resolve those etched particles.

6.2.4 Energy-Dispersive X-Ray Spectroscopy

To study the structure of the NP before and after galvanic replacement reaction, we drop-casted NP suspensions onto the TEM grids. The low magnification TEM images in Fig. 6.4 shows the structure of the Ag nanocubes before (a) and after (b) reacting with EDTA-capped gold ions solution. Figure 6.4c, d shows the TEM images of a single Ag nanocube before and after interacting with EDTA-capped

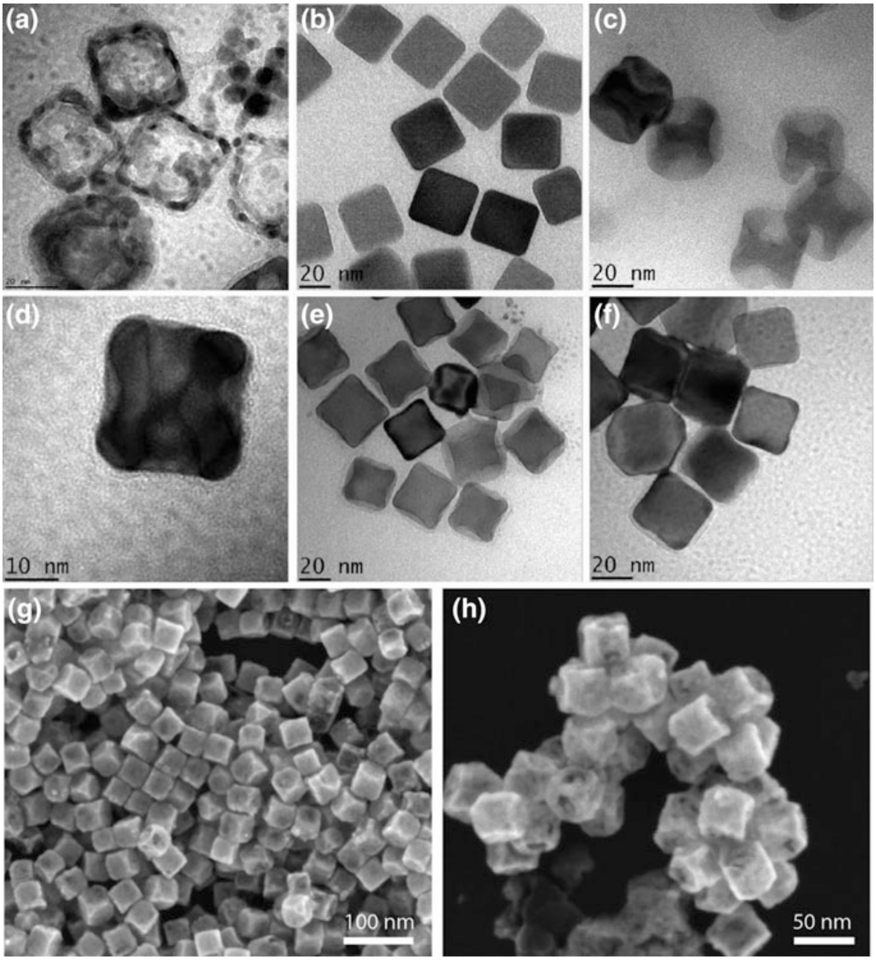

Fig. 6.3 TEM images of silver nanocubes after reacting with **a** $HAuCl_4$ gold precursor solution. **b** EDTA aqueous solution. **c** EDTA-capped gold ions solution for 8 min, while **c**–**f** show the nanostructures where EDTA capped gold ions for different reaction times: **d** 5 min, **e** 8 min and **f** 10 min respectively. **g**, **h** SEM images of silver nanocubes after reacting with EDTA-capped gold ions solution for 8 min

gold ions solution respectively, and the insets show the electron diffraction patterns of those individual nanostructures. Figure 6.4e shows a high resolution TEM image of the particle. The electron diffraction patterns suggest that the Ag nanocubes are single crystals with {100} faces before interacting with the EDTA-capped gold ions solution, similar to what has been reported by Sun et al. [2]. The crystallinity of the nanocubes is preserved after interacting with EDTA-capped gold ions solution.

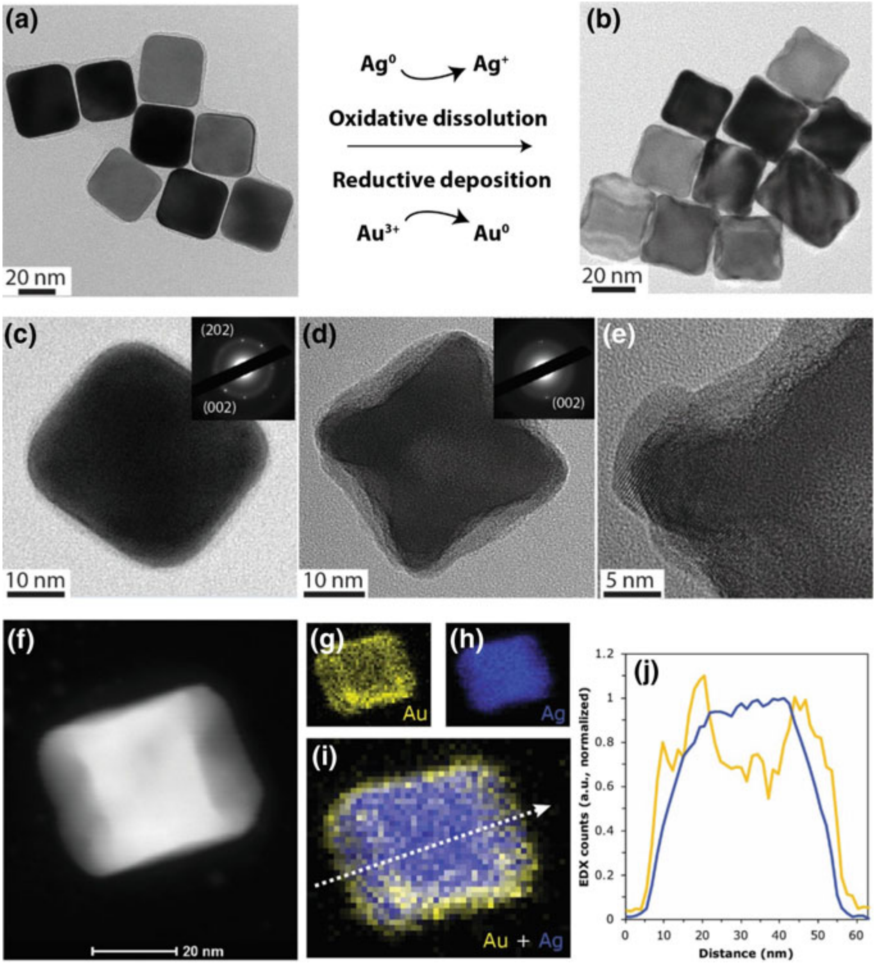

Fig. 6.4 Low magnification TEM images of Ag nanocubes **a** before and **b** after reacting with EDTA-capped $HAuCl_4$ aqueous solution. HRTEM images of an Ag nanocube **c** before and **d**, **e** after reacting with EDTA-capped $HAuCl_4$ aqueous solution. The insets show the corresponding diffraction pattern. **f** HAADF-STEM image and **g**–**i** the corresponding STEM-EDX maps of an individual Ag/Au nanostructure. Note that **g**, **h** show the EDX signal for Ag and Au respectively, while **i** displays the signal for Au and Ag simultaneously. **j** EDX line-scan profiles of the same structure. The yellow line plots the relative counts for Au (yellow) and Ag (blue) along the white arrow in panel (**i**). **j** EDX line-scan profiles of the same structure. The yellow line plots the relative counts for Au (yellow) and Ag (blue) along the white arrow in panel (**i**). Figure reprinted from Ref. [1], with permission from American Chemical Society, Copyright 2016

To discriminate between the Au and Ag, we used STEM-EDX for the following reason. The lattice parameters of Au and Ag are nearly identical resulting in indistinguishable diffraction patterns. In contrast, EDX is element specific and readily allowed us to map the elemental composition of the NP using STEM-EDX [10]. Figure 6.4f–i shows a STEM image and the corresponding EDX maps from a single particle. The results indicate that the final nanostructure consists of Ag and inhomogeneously distributed Au. The EDX line-scan in Fig. 6.4j suggests that the Au is mainly deposited at the edges of the structures, covered like a shell on the etched nanocubes. The atomic percentages of Ag and Au that extracted from the EDX map are 97 ± 1 and 3 ± 1%.

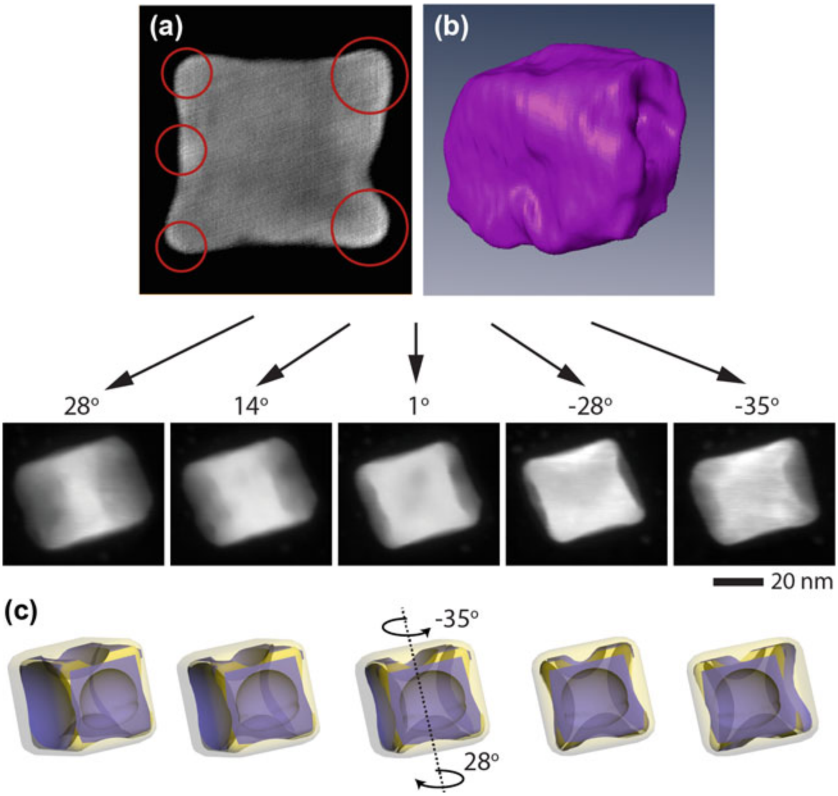

Fig. 6.5 HAADF-STEM tomography images of an individual nanostructure where the substrate was tilted from −70° to +70°. **a** A reconstructed x-y slice extracted from the 3D volume in (**b**). **c** Schematic illustration showing the top and side view of the above structure. Figure reprinted from Ref. [1], with permission from American Chemical Society, Copyright 2016

6.2.5 3D STEM Tomography

To further characterize the final structure of the etched nanocube, 3D STEM tomography was conducted, providing a 3-dimensional view of this structure [11]. We tilted the substrate with the etched nanocube from −70° to +70° with respect to the horizontal axis of the nanocube. We brought the series of images to one rotation axis by aligning all images accurately and reconstructed a 3D volume over 58 STEM images. The reconstructed 3D volume in Fig. 6.5b shows concave faces on the Ag nanocube, while the whole structure remains solid.

In addition, the x-y slice extracted from the 3D volume in Fig. 6.5a reveals that the edges and part of the faces appear brighter (having higher intensities), as indicated by red circles. It is known that the intensity in HAADF-STEM images scales with the atomic number of the elements present in the sample: Ag (47) and Au (79) [12]. This is consistent with our EDX observation in Fig. 6.4i where the Au layer was deposited at the edges and surfaces of the Ag nanocube.

6.3 Conclusions

We observed a different mechanistic pathway where an etching process starts from the faces of the nanocubes followed by Au deposition together with particle coalescence and monomer attachment process, finally lead to a bowl-shaped etched Au/Ag nanostructure. The use of chelating ligands EDTA makes it possible to quantitatively analyze the chemical reactions while they happen. We extracted all the reaction kinetics from the dynamics that we observed inside the *in situ* TEM liquid-cell and the final structure shows good agreement with the *ex situ* characterization techniques such as EDX and 3D STEM Tomography. By using TEM liquid-cell, we are able to conduct a quantitative analysis on single particle dynamics which offer us a way to determine the rate of Ag removal and Au deposition at the nanoscale.

Our results will provide insights into the field of metallic microscopic corrosion and NP growth by galvanic replacement reaction, where a subtle change in stoichiometric ratio could lead to a huge difference in morphology and composition, thereby tuning the structural properties of the nanomaterials which will be important for material engineering in nanofabrication.

6.4 Experimental Section

6.4.1 General Procedures

We purchased the chemicals: poly(vinyl)pyrrolidone, silver nitrate, gold (ɪɪɪ) chloride trihydrate ($HAuCl_4$) and ethylenediaminetetraacetic acid disodium salt dihydrate (EDTA) from Sigma-Aldrich, sodium sulfide and ethylene glycol from J. T. Baker, all chemicals were used without further purification with glass vials from Fisher Scientific. We soaked all the stirrer bars in aqua-regia (mixture of 3:1 volume ratio of nitric acid: hydrochloric acid) for at least 1 hr, washed with deionized water (18.2 MΩ cm), and dried them in an oven at 80–120 °C before use. We washed the NPs with centrifuges of the brand Rotina (380R) and Profuge (14D). The UV-Vis spectra were recorded on a UV/VIS/NIR spectroscope (PerkinElmer Lambda 750), measuring the light transmission through a cuvette of 1 cm light-path.

6.4.2 Synthesis of Silver Nanocubes

Refer to Sect. 3.4.

6.4.3 In Situ Imaging Techniques

We pre-mixed the 5 μl of 10 mM $HAuCl_4$ aqueous solution with 900 μl of 10 mM EDTA aqueous solution for 8 mins. Subsequently, we added 100 μl of as-prepared Ag nanocubes solution into the mixture. We loaded approximately 400 nL of the resulting solution into a liquid-cell, which is comprised of two ultrathin (~ 14 nm) electron translucent SiN_x membranes separated by ~ 200 nm with spacers. Prior to solution loading, these liquid-cells were oxygen plasma treated to make their SiN_x membrane surfaces hydrophilic. Each liquid-cell, sealed with a copper gasket, is inserted into the TEM using a specimen holder. We used a JEOL 2010FEG TEM operated at 200 kV for *in situ* imaging with electron doses ranging from 2000 to 5000 e/$Å^2$ s. We imaged at a rate of 10–25 frames per second with ORIUS SC200 (Gatan, Inc.) CCD camera.

6.4.4 Volume Estimation (Particle in Fig. 6.2)

Edge length of cube = 33.88 nm.

Volume of a spherical cap:

$$V = \frac{\pi h}{6}\left(3a^2 + h^2\right)$$

$$a = \frac{33.88\ \text{nm}}{2} = 16.94\ \text{nm}$$

$$h1 = \frac{(3.85 + 8.74)\ \text{nm}}{2} = 6.30\ \text{nm}$$

$$V1 = \frac{\pi h1}{6}\left(3a^2 + h1^2\right)$$

$$V1 = \frac{\pi(6.30\ \text{nm})}{6}\left[3(16.94\ \text{nm})^2 + (6.30\ \text{nm})^2\right] = 2970.72\ \text{nm}^3$$

$$V_{\text{Ag}} = 6(V1) = 17824.32\ \text{nm}^3$$

$$V2 = \left[\frac{(42.16 + 45.33)}{2}\right]^3 - \left[\frac{(34.28 + 33.48)}{2}\right]^3 = 44821.10\ \text{nm}^3$$

$$V_{\text{Au}} = (V2) = 44821.10\ \text{nm}^3$$

References

1. Tan SF, Lin G, Bosman M, Mirsaidov U, Nijhuis CA. Real-time dynamics of galvanic replacement reactions of silver nanocubes and Au studied by liquid-cell transmission electron microscopy. ACS Nano. 2016;10(8):7689–95.
2. Sun Y, Xia Y. Shape-controlled synthesis of gold and silver nanoparticles. Science. 2002;298 (5601):2176–9.
3. Skrabalak SE, Au L, Li X, Xia Y. Facile synthesis of Ag nanocubes and Au nanocages. Nat Protocols. 2007;2(9):2182–90.
4. Chen J, Wiley B, McLellan J, Xiong Y, Li Z-Y, Xia Y. Optical properties of Pd–Ag and Pt–Ag nanoboxes synthesized via galvanic replacement reactions. Nano Lett. 2005;5(10):2058–62.
5. Sun Y, Xia Y. Mechanistic study on the replacement reaction between silver nanostructures and chloroauric acid in aqueous medium. J Am Chem Soc. 2004;126(12):3892–901.
6. Xia X, Wang Y, Ruditskiy A, Xia Y. 25th anniversary article: galvanic replacement: a simple and versatile route to hollow nanostructures with tunable and well-controlled properties. Adv Mater. 2013;25(44):6313–33.
7. Au L, Lu X, Xia Y. A comparative study of galvanic replacement reactions involving Ag nanocubes and AuCl^{2-} or AuCl^{4-}. Adv Mater. 2008;20(13):2517–22.
8. de Namor AFD, Alfredo Pacheco Tanaka D. Thermodynamics of protonation and complexation of EDTA derivatives and metal cations in water. J Chem Soc Faraday Trans. 1998;94(20):3105–110.
9. Sutter EA, Sutter PW. Determination of redox reaction rates and orders by in situ liquid cell electron microscopy of Pd and Au solution growth. J Am Chem Soc. 2014;136(48):16865–70.
10. Shahjamali MM, Salvador M, Bosman M, Ginger DS, Xue C. Edge-gold-coated silver nanoprisms: enhanced stability and applications in organic photovoltaics and chemical sensing. J Phys Chemi C. 2014;118(23):12459–68.

11. Goris B, Polavarapu L, Bals S, Van Tendeloo G, Liz-Marzán LM. Monitoring galvanic replacement through three-dimensional morphological and chemical mapping. Nano Lett. 2014;14(6):3220–6.
12. Pennycook SJ, Jesson DE. High-resolution Z-contrast imaging of crystals. Ultramicroscopy. 1991;37(1):14–38.

Chapter 7
Real-Time Imaging of Au–Ag Core-Shell Nanoparticles Formation

Abstract In this Chapter, we studied the overgrowth process of silver on gold nanocubes in dilute, aqueous silver nitrate solution in the presence of reducing agent, ascorbic acid using *in situ* liquid-cell electron microscopy. Au–Ag core-shell nanostructures were formed via two mechanistic pathways: (1) nuclei coalescence where the silver nanoparticles absorbed onto the gold nanocubes and (2) monomer attachment where the silver atoms epitaxially deposited onto the gold nanocubes. Both pathways lead to the same Au–Ag core-shell nanostructures. Analysis of the silver deposition rate reveals the growth modes of this process and show that this reaction is chemically-mediated by the reducing agent, ascorbic acid.

7.1 Introduction

Core-shell nanoparticles (NPs) are highly functionalized NPs with distinctive properties that originate from different materials. The properties of the core-shell NPs can be tuned by either the constituting materials or the core to shell ratio [1]. This tunability makes it possible to manipulate the surface properties so as to meet the requirements for a range of applications, including biomedical [2], pharmaceutical [3], catalysis [4], electronics [5], enhancing photoluminescence [6, 7], etc. The advantages of coating on the core particle over surface modification of NPs are many-fold and core-shell NPs have improved functionality, stability, dispersibillity, than the surface modified particles. Furthermore, core-shell NPs are also used in applications requiring controlled released of the core to form hollow nanostructures, reduction in consumption of precious materials [8].

The fabrication of core-shell NPs with different morphology and composition can be accomplished by various chemicals means such as solution phase reduction [9, 10] and physical methods such as wire electrical explosion followed by the ultrasonic irradiation [11]. Fine-tuning of the surface structure, i.e., the dominant crystalline facets and surface composition, is important for applications such as catalysis and can be accomplished with the addition of different chemical additives [12]. For instance, whether {111} or {100} facets dominate on the silver (Ag) shells

S. F. Tan, *Molecular Electronic Control Over Tunneling Charge Transfer Plasmons Modes*, Springer Theses, https://doi.org/10.1007/978-981-10-8803-2_7

is determined by the presence of chemical additives poly(vinyl)pyrrolidone (PVP), *N*,*N*-dimethylformamide (DMF) and ethylene glycol (EG) [12]. In general, the synthesis parameters are derived empirically and the final NP morphology is confirmed with the so-called 'quench-and-look' approach, where the reaction is stopped at various stages, after which the intermediate reaction products are imaged with techniques such as transmission electron microscopy (TEM). However, early stages of the reactions and intermediate structures cannot be investigated this way. As such, the interplay of different chemical additives, such as surfactants and reducing agents, remain largely unresolved. Clarification of these questions is important to understand how processes such as atom deposition and surface diffusion in dictating the evolution of a seed into nanocrystals of various shapes.

For chemically-synthesized Au–Ag cubic core-shell NPs, Xia and co-workers [13] reported that the gold (Au) cubes tend to nucleate and grow homogeneously on six low-index (100) planes of the cubic seeds when a strong reducing agent, ascorbic acid (AA) was used. They attributed the observation to fast reducing kinetics by ascorbic acid (AA) which promote the formation of {100} in the presence of bromide ions from the surfactants, cetyltrimethylammonium bromide (CTAB). There are also studies suggested that the overgrowth is promoted by the Br^- ions [9, 10, 14]. Previously reported studies [9, 12, 13, 15, 16] have suggested the size of the shell is dependent on the ratio of precursor, reducing agent and size of the core. Under conditions of increased precursor and reducing agent, the Ag prefers to continue growing on the Ag overgrowth rather than to homonucleate in the solution as heterogeneous nucleation and growth is generally more favorable than homogeneous nucleation as a result of lowered free energy barrier [17].

Moreover, Xia et al. [18] has also proposed the final product of the overgrowth reaction is determined by the ratio between the rates of atom deposition ($V_{\text{deposition}}$) and surface diffusion ($V_{\text{diffusion}}$). The stable shape of the resultant nanostructure will depend on the presence of capping agents to stabilize the enlarged high energy facets, the lack of which will lead to the nanostructure adopting the thermodynamically favoured shape. However, it is still ambiguous how the atoms get deposited onto the surface of a seed and migrated to other sites of the surface, leading to the formation of diversified shape of the shell. Moreover, there is little experimental verification of these overgrowth mechanisms due to the difficulties in probing the early stages of growth as mentioned in the previous paragraph.

In this Chapter, we studied the formation of Au–Ag core-shell nanocubes, which had been shown to possess excellent and tunable plasmonic properties [9, 10, 16], using liquid-cell TEM [19]. We used a synthesis recipe which is similar to the cited work to fabricate these nanostructures with the following differences. (1) The Au seeds are subjected to washing procedure in order to minimizing the surfactants concentration before introducing into the liquid-cell. (2) The Au seeds are drop-casted on one half of the liquid-cell prior to assembly and silver nitrate solution introduced via the flow tubing after loading the holder into the TEM. (3) The experiments are carried out at room temperature. The *in situ* results are also compared against nanocubes that we synthesized on the laboratory bench

(Sect. 7.2.3 for details). Surprisingly, we found that our initial strategy of using the electron beam as substitute for a reducing agent did not work for the growth of the Au–Ag core-shell nanocubes [19].

7.2 Results and Discussion

7.2.1 The Reducing Agent: Electron Beam

In situ electron microscopy with liquid-cell is an emerging technique for elucidating the mechanisms of nanostructure formation [20–22]. It is also well-known that the electron beam itself can act as a reducing agent and reduce metal ions into atoms through the action of solvated electrons (from radiolysis of water). This effect has been exploited for dynamical studies of Ag [23, 24] NP nucleation directly from solution. Recently, Jungjohann et al. [15] and Wu et al. [16] demonstrated the use of *in situ* liquid-cell microscopy to study the solution growth of Au–Pd and Pt–Au core-shell NPs, respectively. In both studies, the electron beam replaces the reducing agent, leading to metal deposition.

Figure 7.1 shows typical structures that were formed when silver nitrate was introduced to Au cubes in the absence of L-ascorbic acid (using electron beam as reducing agent). We did not observe the well-defined Au–Ag core-shell nanostructures formation under electron beam irradiation. When Ag clusters attach to the Au cuboids, they attach randomly and develop into ramified structures. They did not merge into a conformal layer but tend to have dendritic growth (red arrows).

7.2.2 The Role of Chemical Additives: Ascorbic Acid

In subsequent experiments, we reverted back to conventional recipe by pre-mixing the Au nanocubes with a reducing agent of L-ascorbic acid before introducing the

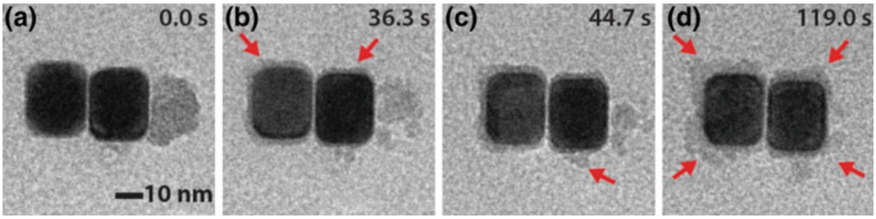

Fig. 7.1 **a**–**d** Time-lapse TEM images showing two gold nanocubes interacting with the silver nitrate aqueous solution in the absence of L-ascorbic acid inside a liquid flow cell. Figure reprinted from Ref. [19], with permission from American Chemical Society, Copyright 2016

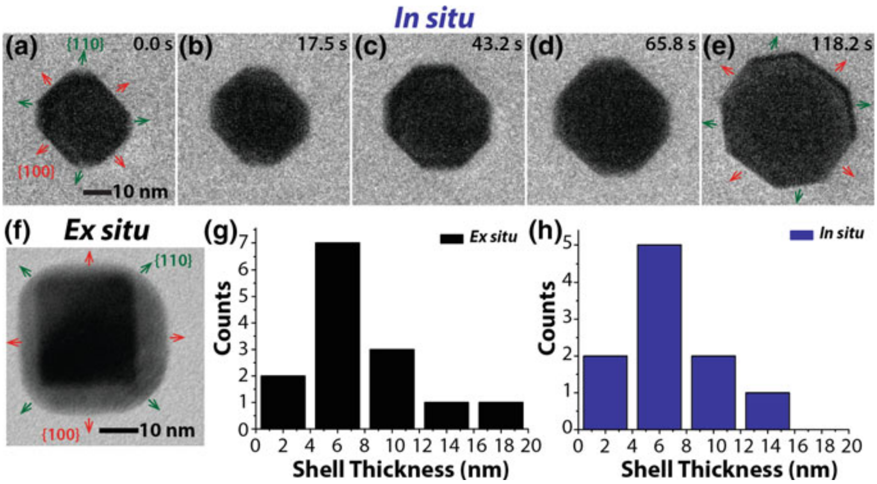

Fig. 7.2 **a**–**e** Time-lapse TEM images showing a gold nanocube interacting with the silver nitrate aqueous solution in the presence of L-ascorbic acid inside a liquid flow cell. **f** TEM image of *ex situ* prepared Au–Ag core-shell nanostructures with addition of ascorbic acid. Histograms of Au–Ag core shell nanoparticles that are prepared by **g** *ex situ* **h** *in situ* methods respectively. Figure reprinted from Ref. [19], with permission from American Chemical Society, Copyright 2016

Ag precursor solution into the mixture. Figure 7.2a–e shows time-lapse TEM images of Au–Ag core-shell nanocubes that were observed *in situ*. In this case, the shell formation is conformal and homogeneous instead of randomly attachment as seen in Fig. 7.1. Moreover, these core-shell nanostructures are similar in terms of morphology to those prepared *ex situ* (Fig. 7.2f). *In situ* observations and *ex situ* TEM diffraction result also show that growth of the Ag layer results in the development of {110} facets (Fig. 7.2a), in agreement with core-shell NPs synthesized on the laboratory bench. The measured shell thicknesses are indistinguishable for the Au–Ag nanostructures prepared by *in situ* (7 ± 3 nm) and *ex situ* (7 ± 3 nm) methods as shown in the histogram. Due to the similarities, we believe that while the electron beam can reduce silver nitrate and it does not promote the overgrowth reaction.

Furthermore, our results do not agree with overgrowth model promoted by the halide ions as mentioned in the introduction. The Au nanocubes that were used in our experiments have been washed and there should be little residual CTAB left in solution. The lack of available CTAB is also evidenced by the Au nanocubes gradually changing their shapes with time after washing (Fig. 7.3). Therefore, initial formation of the Ag layer is due to the presence of ascorbic acid. Given that there was also no overgrowth when the electron beam was used as a reducing agent, we suggest that ascorbic acid plays a previously unknown role of guiding the overgrowth of Ag.

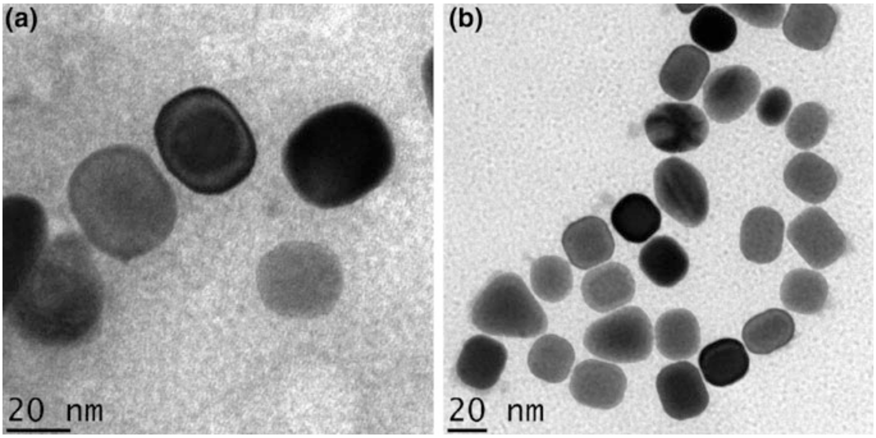

Fig. 7.3 TEM images of aged nanocubes at room temperature, ~2 hours after the washing procedure

Figure 7.3 shows the TEM images of the aged Au nanocubes (aging time: ~2 hours) after the washing procedure. The corners of the nanocubes start to turn round, and eventually become quasi-spherical Au NPs.

7.2.3 Ex Situ *Characterization*

Figure 7.4 show the TEM images of the *in situ* prepared Au/Ag nanostructures after reacting with silver nitrate solution without (a) and with (b) ascorbic acid. As mentioned above, we observed the inhomogeneous coating of the Ag onto the Au cubes without the presence of the ascorbic acid. In addition, we merely observed ramified structures. With the addition of ascorbic acid, we observe the formation of Au–Ag core-shell nanostructures via *ex situ* characterization techniques, such as UV-Vis spectroscopy, EDX, 3D STEM Tomography and TEM diffraction.

7.2.3.1 UV-Vis Spectroscopy

Figure 7.5 shows the low magnification TEM images of the *ex situ* prepared Au nanocubes before (a) and after (c) reacting with the silver nitrate aqueous solution. The UV-Vis spectra in Fig. 7.5b indicates that this reduction reaction happened within 1 min (the spectra was collected right after the addition of silver nitrate solution), the color of the solution changed instantly from purple to red color.

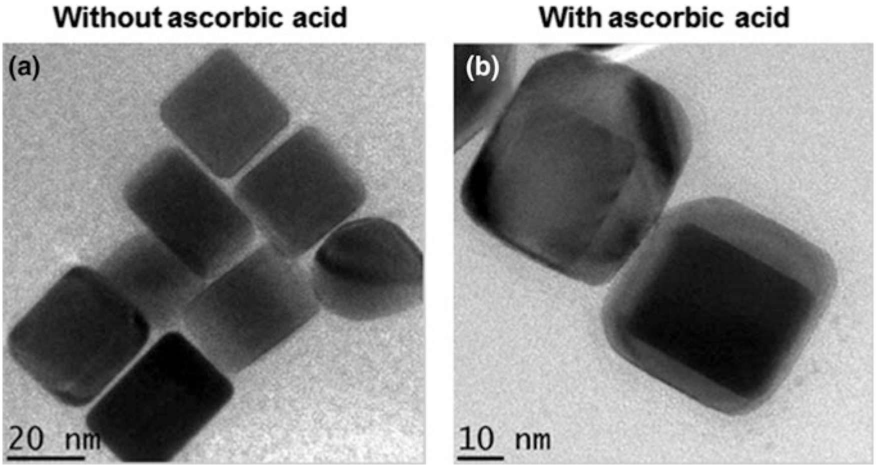

Fig. 7.4 TEM images of gold nanocubes after reacting with **a** silver nitrate solution without ascorbic acid **b** silver nitrate solution with ascorbic acid.

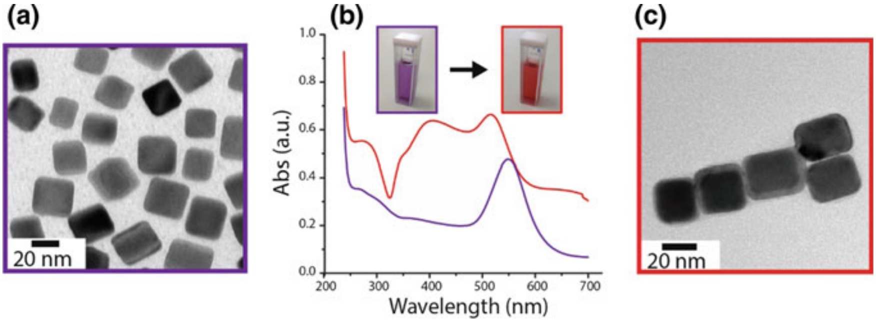

Fig. 7.5 Low magnification TEM images of *ex situ* prepared gold nanocuboids **a** before and **c** after reacting with silver nitrate aqueous solution (**b**) UV-vis spectra of the solution before (purple) and after (red) adding the silver nitrate aqueous solution. The insets show the corresponding photographs of the solutions

7.2.3.2 TEM Imaging Characterization

In addition, we found out that the Ag shell transformed from a cubic shape into a truncated cubic/octahedral shape, the assymmetric growth of Ag on Au becomes more and more symmetric (Fig. 7.6a–c) upon increasing the concentration of the reducing agent. The *ex situ* prepared Au–Ag core-shell nanostructures show that the growth of the Ag layer results in the development of {100} facets changing to {110} facets as the reduction proceeds. It is also worth noting that the thickness of

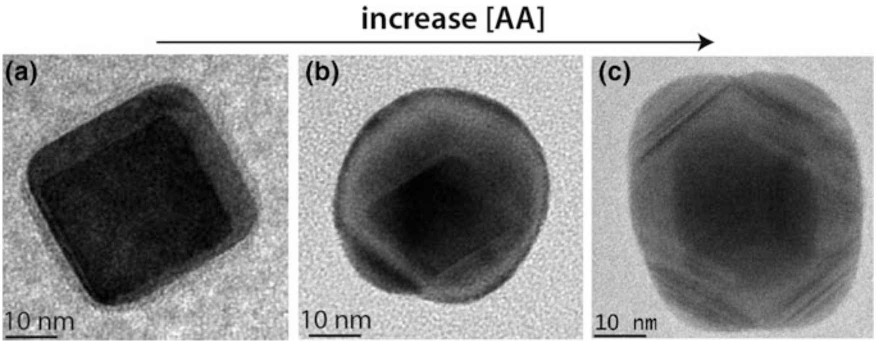

Fig. 7.6 TEM images of gold nanocubes after reacting with fixed amount of 20 µl of 10 mM silver nitrate solution and 10 mM of ascorbic acid of **a** 10 µl, **b** 50 µl, **c** 200 µl

the shells (see Fig. 7.2 for histograms) are similar for both *ex situ* and *in situ* observation. These explain our *in situ* results where the Ag layer grows and develops into {110} facets when an additional reduction source—the electron beam—is present.

7.2.3.3 TEM Diffraction

Figure 7.7a, c shows the TEM images of the individual nanostructure and the corresponding electron diffraction patterns before and after reacting with the Ag precursor solution. The electron patterns suggest that the Au nanocubes are single crystals with {100} facets before reacting with the silver nitrate solution. The Au–Ag core-shell nanostructure show a diffraction patterns with {110} and {111} facets. The nanostructure in Fig. 7.7f shows the cubohedron enclosed by a mix of {111} and {110}. It must be noted that the lattice parameters of Au and Ag are nearly identical, so we are not able to distiguish between Au and Ag diffraction spots directly, but STEM-EDX (Sect. 7.2.3.4) can make this distinction.

7.2.3.4 Energy-Dispersive X-Ray Spectroscopy (EDX)

Figure 7.8 shows (a and c) STEM images and the corresponding EDX line scans (b and d) from a single Au–Ag core-shell nanostructure. The line scans suggest that the shell is consisted of Ag while the core remains as Au. Moreover, the shell thickness is not uniformly covered over the nanocube. The intensity in the HAADF-STEM images scales with the atomic number of the elements present in the sample: Ag (47) and Au (79) [25].

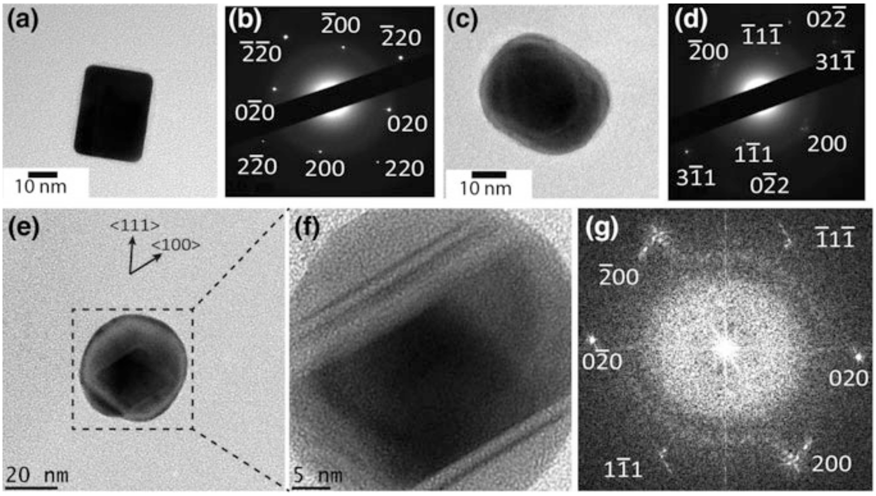

Fig. 7.7 TEM images of a gold nanocube **a** before and **c** after reacting with silver nitrate aqueous solution in the presence of ascorbic acid and their corresponding diffraction patterns (**b**, **d**) respectively. **e**, **f** showing the high resolution TEM images of a Au–Ag core-shell nanostructure and its corresponding FFT (**g**)

7.2.3.5 3D HAADF-STEM Tomography

We conducted HAADF-STEM tomography which is able to provide a 3-dimensional view to further characterize the Au–Ag core-shell nanostructures [26]. We tilted the substrate with the etched nanocube from −65° to +65° with respect to the horizontal axis of the nanocube. We brought the series of images to one rotation axis by aligning all images accurately and reconstructed a 3D volume over 57 STEM images eventually. The reconstructed 3D volume showed clearly a truncated cube/octahedron Ag shell coated on the Au nanocube. In addition, the HADDF-STEM images in Fig. 7.9c reveal that the core of the structure appears to be brighter (higher intensities) which were indicated by red dotted lines. The intensity in the HAADF-STEM images scales with the atomic number of the elements present in the sample: Ag (47) and Au (79) [25]. This is consistent with our EDX observation in Fig. 7.8 where the Ag layer was deposited onto the Au nanocube.

7.2.4 In Situ *Observation: Mechanistic Pathways for Core-Shell Nanoparticles Formation*

Furthermore, our results show that two mechanistic pathways in which the overgrowth occurs. (1) Pre-nucleated Ag NPs approach and absorb onto the Au nanocubes, followed by coalescence to form a layer of Ag on the Au nanocube.

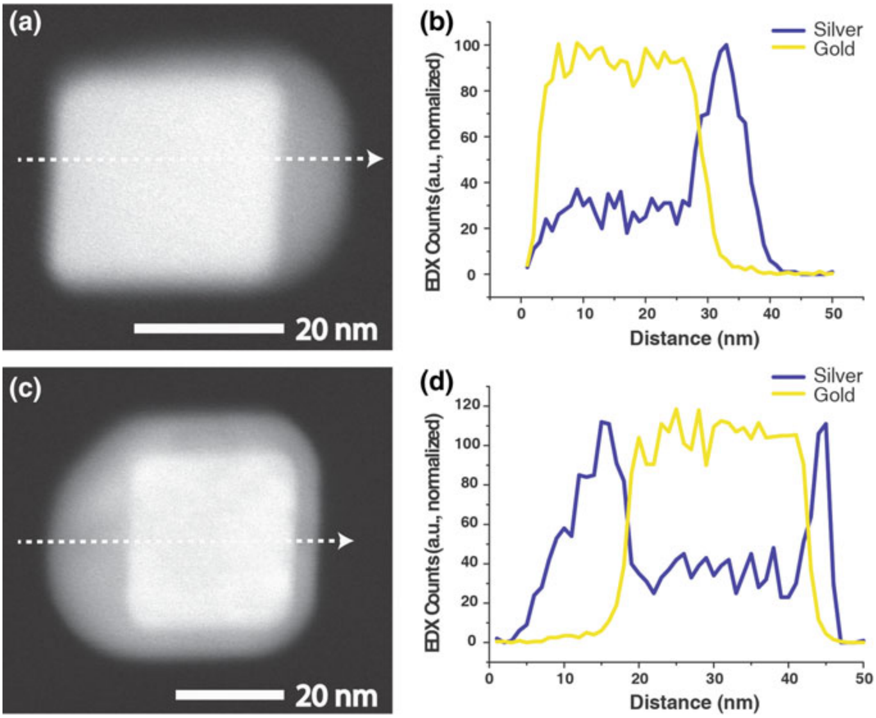

Fig. 7.8 **a**, **c** HAADF-STEM images of two Ag/Au core-shell nanostructures while **b**, **d** EDX line-scan profiles of the same structure respectively. The yellow line plots the gold counts; the blue line the silver counts from the location of the white arrow in panel (**a**, **c**) respectively

(2) The Au nanocubes undergo deposition of Ag through monomer attachment. Figure 7.10a, c shows two time series of TEM images from single Au nanocube reacting with the silver nitrate aqueous solution inside a liquid flow cell *via* the two pathways resulting in the Au–Ag core-shell NP formation. Figure 7.10b, d illustrate these two processes schematically.

For the first pathway, we observed the formation of small particles of diameter ~3 nm (encircled in red) at $t = 4.7$ s. We believe these small Ag particles are formed when the silver nitrate solution is brought in contact with the (1) L-ascorbic acid solution inside the liquid-cell or (2) through radiolysis (i.e., reduction of the Ag^+ ions by solvated electrons). The image recorded at $t = 17.8$ s and the subsequent images show that the small Ag NPs attach onto the surface of the Au nanocube and then merge into a continuous layer. In addition, the shell thickness at the edge (E) and corner (D) in Fig. 7.10e shows a non-linear growth as a result of the small particles dissolution. The measurement of thickness is done over three real-time movies of three different particles. For the second pathway, there is no small particles formation throughout the whole growth process. We observed a conformal growth (homogeneous coating) of the Ag shell as a function of time.

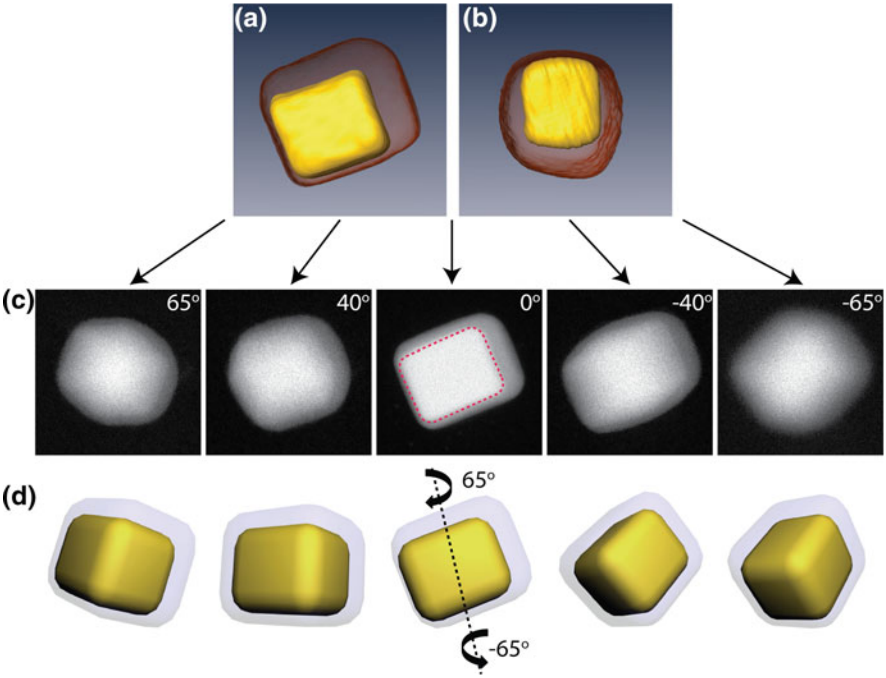

Fig. 7.9 Surface-rendered visualization of the Au–Ag core-shell nanostructure morphology reconstructed by HAADF-STEM tomography, viewed along the **a** [100] and **b** [001] axes. **c** HAADF-STEM tomography images of an individual nanostructure where the substrate was tilted from −65° to +65°. **d** Schematic illustration showing the top view of the above structure

Both pathways will eventually lead to the same final product: the Au–Ag core-shell nanostructure.

Similarly limited growth also has been reported in previous studies [9, 10, 12, 13, 16]. Electron beam depletion of the precursor solution can be one reason causing the termination of further shell growth in the *in situ* experiments, but we also observe Ag NPs formation outside the field of view due to electron beam reduction. Furthermore, it does not explain why the growth seems to be size-controlled in the *ex situ* experiments (Fig. 7.6a–c).

In addition, we also observed the shapes of our final product majority are cuboctahedrons (Fig. 7.10a, c) and enlarged cubes with truncated corners (Fig. 7.2a–e) occasionally. This suggests that thermodynamic control is responsible for the exquisite tunability of the overgrowth layers in these nanostructures [27]. In this route, surface diffusion is faster than the atom deposition where the adatoms tend to migrate from the corners to the edges and side faces. If surface diffusion is much faster than the deposition rate (i.e., the ratio is much less than 1), growth is promoted along ⟨100⟩ and ⟨110⟩ directions, leading to the formation of cubohedral shells (Fig. 7.11a). In the other case where the ratio between atom deposition and surface diffusion is less than but close to 1, conformal growth is expected

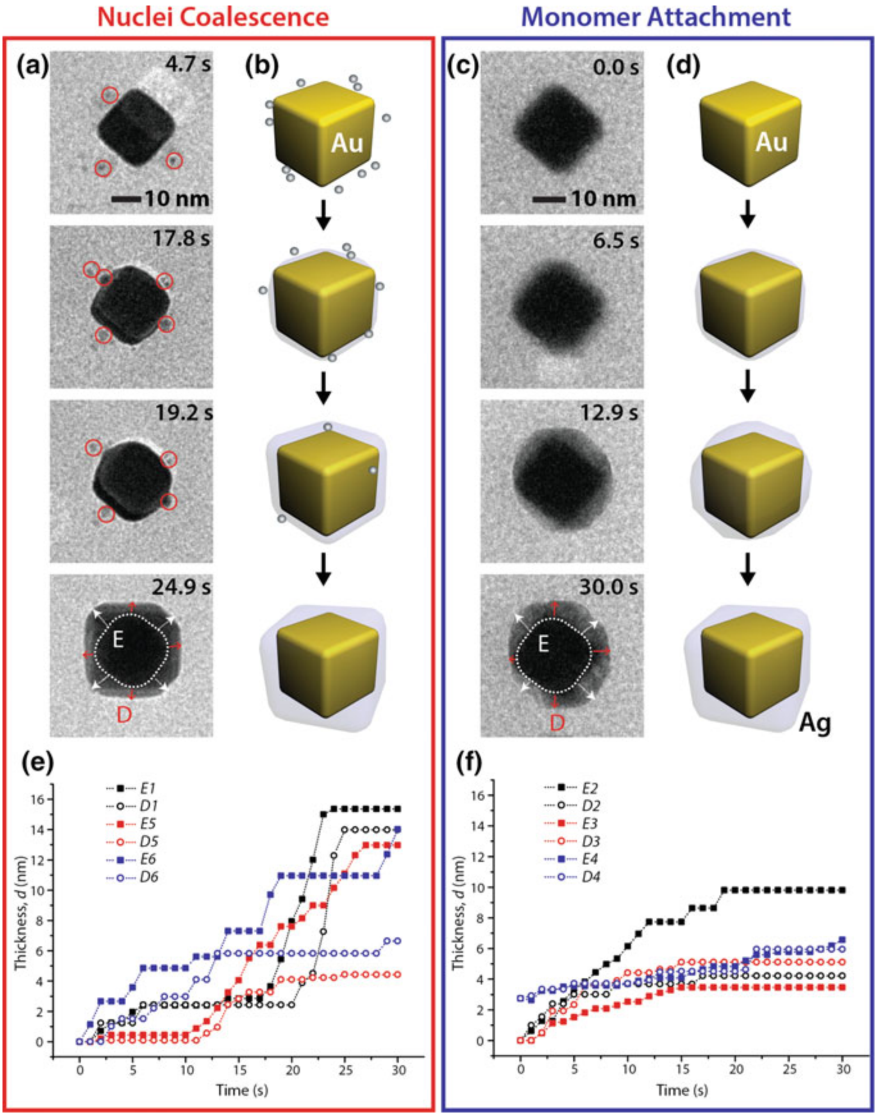

Fig. 7.10 Time-lapse TEM images showing a gold nanocube interacting with the silver nitrate aqueous solution inside a liquid flow cell via **a** Ostwald ripening process and **c** monomer attachment. The schematic of the reaction between gold nanocubes and silver nitrate aqueous solution for both pathways: (**b**, **d**). The measured thickness of edge (E, solid squares) and corner (D, hollow circles) of the Au–Ag core-shell particle as a function of time for both pathways: (**e**, **f**). Figure reprinted from Ref. [19], with permission from American Chemical Society, Copyright 2016

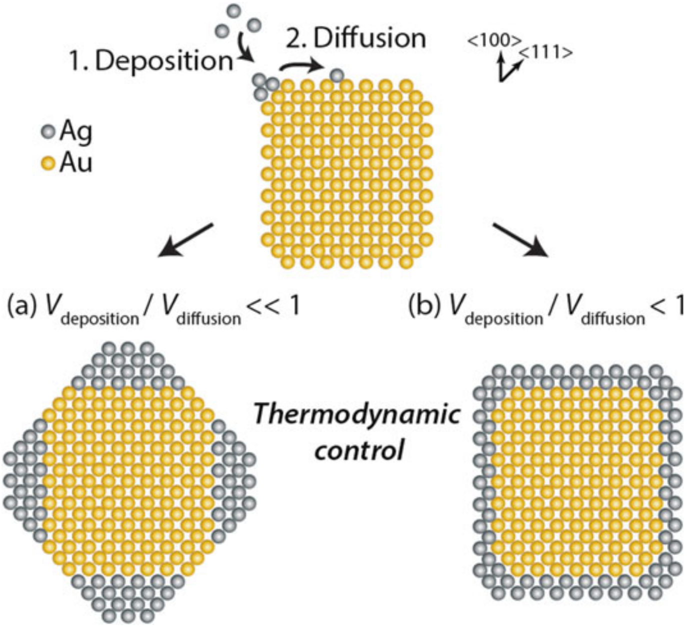

Fig. 7.11 Schematic illustrations showing the shape evolution of a cubic seed under thermodynamic control for two kinetic conditions: **a** $V_{\text{deposition}}/V_{\text{diffusion}} \ll 1$, **b** $V_{\text{deposition}}/V_{\text{diffusion}} < 1$. This model is adapted from Xia et al. [27]. Figure reprinted from Ref. [19], with permission from American Chemical Society, Copyright 2016

(Fig. 7.11b). We propose that our experiment is an example of the latter for three reasons. (1) As described earlier, the capping agents would have been washed out prior to the Ag introduction. (2) Our experiments were conducted at room temperature (in contrast to the synthesis temperatures of 60 °C reported by Xia et al. [18] and Tsuji et al. [12], making it unlikely that surface diffusion will be fast). (3) The *in situ* experiments show that the growth starts off in a conformal manner.

Therefore, the development of {110} facets in both *in situ* and *ex situ* results (Fig. 7.9) leads to the final cuboctahedron shape of the nanostructures and would indicate the growth mechanism is thermodynamically controlled with the absence or low coverage of capping agents. Furthermore, the *in situ* results also indicate that atomic deposition is not the only mechanisms by which the Ag layer grows. The coalescence and integration of pre-existing nuclei into a growing shell implies that the growth can also take place via attachment-based growth [28, 29]. Attachment-based refers to a non-classical growth mechanism where crystals grow via attachment, re-orientation and coalescence of smaller nanocrystals. The main driving force here is the reduction in surface energy.

7.3 Conclusions

We studied the overgrowth process of Ag on Au nanocubes with addition of chemical reducing agent ascorbic acid. First, we show that the initial overgrowth is chemically-mediated by ascorbic acid and not CTAB, which contradicts conventional understanding. Second, we observe two different mechanistic pathways. (1) The Ag NPs approach and absorb onto the Au nanocubes, while simultaneously a layer of Ag was deposited onto the Au nanocube as a result of coalescence. (2) The Au nanocubes undergo epitaxial deposition of Ag through monomer attachment. Both mechanistic pathways lead to the same final products. This all round growth could be due to poor coverage of the capping agents. Absence of overgrowth when only the electron beam was used to reduce the Ag precursor and comparison with *ex situ* synthesized nanostructures suggest that the observed reaction may be insensitive to the electron beam. This study shows that not only allow us to study growth mechanisms with *in situ* TEM, the technique can also be used to elucidate the role of the chemical additives, which would be useful for material engineering in nanofabrication.

7.4 Experimental Section

7.4.1 General Procedures

For the Au nanocuboids, the chemicals: gold (ɪɪɪ) chloride trihydrate, sodium borohydride, cetyltrimethylammonium bromide, copper sulfate, L-ascorbic acid were all purchased from Sigma-Aldrich and used without further purification. The glass vials used for synthesis were obtained from Fisher Scientific. Solvents for NPs functionalization were freshly distilled prior to use. All stirrer bars were soaked in aqua-regia (mixture of 1:3 volume ratio of nitric acid:hydrochloric acid) for at least 1 h, washed with deionized water (18.2 Ω cm) and dried in an oven before use. NPs were washed in Rotina (model 380R) and Profuge (model 14D) centrifuges.

7.4.2 Synthesis of Gold Nanocuboids

Refer to Sect. 5.2.1. The experimental details are described in Sect. 5.4.

7.4.3 Experimental Techniques

We transferred 1.0 ml of the cuboidal Au NPs solution from the glass vial into a 1.5 ml-centrifuge tube. Centrifugation and redispersion in water was performed twice at 10,000 rpm for 10 min in order to minimise the concentration of CTAB prior to loading to the liquid-cell. Note that too many times of washing (centrifuge and redisperse) will cause the deformation of Au cuboids. 10 μl of 10 mM ascorbic acid aqueous solution was added into the as-washed Au cuboids solution.

Approximately 500 nl of the resulting solution was loaded into a TEM liquid-cell, which comprised of two ultrathin ($\sim$30 nm) electron translucent SiN_x membranes separated by 200 nm. Prior to solution loading, these liquid-cells were oxygen plasma treated to make their SiN_x membrane surfaces hydrophilic. We used a Hummingbird Scientific Liquid Flow holder and a JEOL 2010FEG TEM operated at 200 kV for *in situ* imaging with low electron doses ranging from 50 to 150 e/$Å^2$ s, acquiring images at a rate of 10 frames per second with an ORIUS SC200 CCD camera (Gatan, Inc.). The reaction was followed in real-time by observing cuboids found in 30 μm by 200 μm window of the TEM liquid-cell. The high-angle annular dark-field scanning TEM (HAADF-STEM) imaging and chemical analysis were performed with an FEI Titan TEM equipped with a Schottky electron source operated at 200 kV. We obtained the STEM images by using an electron probe with an approximate diameter of 0.3 nm. EDX was performed with a probe ca. 0.5 nm in diameter with 150 ms acquisition time for each spectrum. The Inspect3D software from FEI was used for 3D tomography reconstruction. We recorded the UV/Vis spectra on UV/VIS/NIR spectroscopy (PerkinElmer Lambda 750). We measured the light transmission through a cuvette of 1 cm light-path.

References

1. Oldenburg SJ, Averitt RD, Westcott SL, Halas NJ. Nanoengineering of optical resonances. Chem Phys Lett. 1998;288(2–4):243–7.
2. Laurent S, Forge D, Port M, Roch A, Robic C, Vander Elst L, Muller RN. Magnetic iron oxide nanoparticles: synthesis, stabilization, vectorization, physicochemical characterizations, and biological applications. Chem Rev. 2008;108(6):2064–110.
3. Caruso F. Nanoengineering of particle surfaces. Adv Mater. 2001;13(1):11–22.
4. Daniel M-C, Astruc D. Gold nanoparticles: assembly, supramolecular chemistry, quantum-size-related properties, and applications toward biology, catalysis, and nanotechnology. Chem Rev. 2004;104(1):293–346.
5. Kortan AR, Hull R, Opila RL, Bawendi MG, Steigerwald ML, Carroll PJ, Brus LE. Nucleation and growth of cadmium selendie on zinc sulfide quantum crystallite seeds, and vice versa, in inverse micelle media. J Am Chem Soc. 1990;112(4):1327–32.
6. Mews A, Eychmueller A, Giersig M, Schooss D, Weller H. Preparation, characterization, and photophysics of the quantum dot quantum well system cadmium sulfide/mercury sulfide/cadmium sulfide. J Phys Chem. 1994;98(3):934–41.

7. Ma GH, He J, Rajiv K, Tang SH, Yang Y, Nogami M. Observation of resonant energy transfer in Au:CdS nanocomposite. Appl Phys Lett. 2004;84(23):4684–6.
8. Ghosh Chaudhuri R, Paria S. Core/shell nanoparticles: classes, properties, synthesis mechanisms, characterization, and applications. Chem Rev. 2012;112(4):2373–433.
9. Ma Y, Li W, Cho EC, Li Z, Yu T, Zeng J, Xie Z, Xia Y. Au–Ag core–shell nanocubes with finely tuned and well-controlled sizes, shell thicknesses, and optical properties. ACS Nano. 2010;4(11):6725–34.
10. Gong J, Zhou F, Li Z, Tang Z. Synthesis of Au–Ag core-shell nanocubes containing varying shaped cores and their localized surface plasmon resonances. Langmuir. 2012;28(24):8959–64.
11. Fu W, Yang H, Chang L, Li M, Bala H, Yu Q, Zou G. Preparation and characteristics of core–shell structure nickel/silica nanoparticles. Colloids Surf A. 2005;262(1–3):71–5.
12. Tsuji M, Matsuo R, Jiang P, Miyamae N, Ueyama D, Nishio M, Hikino S, Kumagae H, Kamarudin KSN, Tang X-L. Shape-dependent evolution of Au–Ag core–shell nanocrystals by PVP-assisted *N*,*N*-dimethylformamide reduction. Crys Growth Des. 2008;8(7):2528–36.
13. Lim B, Kobayashi H, Yu T, Wang J, Kim MJ, Li Z-Y, Rycenga M, Xia Y. Synthesis of Pd–Au bimetallic nanocrystals *via* controlled overgrowth. J Am Chem Soc. 2010;132(8):2506–7.
14. Cho EC, Camargo PHC, Xia Y. Synthesis and characterization of noble-metal nanostructures containing gold nanorods in the center. Adv Mater. 2010;22(6):744–8.
15. Jungjohann KL, Bliznakov S, Sutter PW, Stach EA, Sutter EA. In situ liquid cell electron microscopy of the solution growth of Au–Pd core-shell nanostructures. Nano Lett. 2013;13(6):2964–70.
16. Wu J, Gao W, Wen J, Miller DJ, Lu P, Zuo J-M, Yang H. Growth of Au on Pt icosahedral nanoparticles revealed by low-dose in situ TEM. Nano Lett. 2015;15(4):2711–5.
17. Fan F-R, Liu D-Y, Wu Y-F, Duan S, Xie Z-X, Jiang Z-Y, Tian Z-Q. Epitaxial growth of heterogeneous metal nanocrystals: from gold nano-octahedra to palladium and silver nanocubes. J Am Chem Soc. 2008;130(22):6949–51.
18. Xia X, Xie S, Liu M, Peng H-C, Lu N, Wang J, Kim MJ, Xia Y. On the role of surface diffusion in determining the shape or morphology of noble-metal nanocrystals. Proc Natl Acad Sci. 2013;110(17):6669–73.
19. Tan SF, Chee SW, Lin G, Bosman M, Lin M, Mirsaidov U, Nijhuis CA. Real-time imaging of the formation of Au-Ag core-shell nanoparticles. J Am Chem Soc. 2016;138(16):5190–3.
20. Mirsaidov UM, Zheng H, Bhattacharya D, Casana Y, Matsudaira P. Direct observation of stick-slip movements of water nanodroplets induced by an electron beam. Proc Natl Acad Sci. 2012;109(19):7187–90.
21. Zheng H, Smith RK, Jun Y-W, Kisielowski C, Dahmen U, Alivisatos AP. Observation of single colloidal platinum nanocrystal growth trajectories. Science. 2009;324(5932):1309–12.
22. Liao H-G, Niu K, Zheng H. Observation of growth of metal nanoparticles. Chem Commun. 2013;49(100):11720–7.
23. Woehl TJ, Evans JE, Arslan I, Ristenpart WD, Browning ND. Direct in situ determination of the mechanisms controlling nanoparticle nucleation and growth. ACS Nano. 2012;6(10):8599–610.
24. Noh KW, Liu Y, Sun L, Dillon SJ. Challenges associated with in-situ TEM in environmental systems: the case of silver in aqueous solutions. Ultramicroscopy. 2012;116:34–8.
25. Pennycook SJ, Jesson DE. High-resolution incoherent imaging of crystals. Phys Rev Lett. 1990;64(8):938–41.
26. Goris B, Polavarapu L, Bals S, Van Tendeloo G, Liz-Marzán LM. Monitoring galvanic replacement through three-dimensional morphological and chemical mapping. Nano Lett. 2014;14(6):3220–6.
27. Xia Y, Xia X, Peng H-C. Shape-controlled synthesis of colloidal metal nanocrystals: thermodynamic versus kinetic products. J Am Chem Soc. 2015;137(25):7947–66.

28. Penn RL, Soltis JA. Characterizing crystal growth by oriented aggregation. Cryst Eng Comm. 2014;16(8):1409–18.
29. Ataee-Esfahani H, Skrabalak SE. Attachment-based growth: building architecturally defined metal nanocolloids particle by particle. RSC Adv. 2015;5(59):47718–27.

Chapter 8
General Conclusions and Outlook

This thesis describes the controlled immobilization of molecules between two cuboidal metal nanoparticles (NPs) by self-assembly to control quantum plasmon resonances. Mixed self-assembled monolayers (SAMs) of thiolates and dithiolates molecules were used to control the gap sizes between the metal NPs down to sub-nanometer scales. We studied quantum mechanical tunneling across the metal-molecules-metal junctions by a combination of complimentary characterization techniques, e.g., electron microscopy, electron spectroscopy, and theoretical support was provided *via* quantum-corrected finite-element-model (FEM) simulations. It was demonstrated that the SAMs not only could control the width between two plasmonic resonators but also could act as frequency controllers in the terahertz regime, providing a new control parameter in the fabrication of electrical circuits facilitated by quantum plasmon tunnelling.

Chapter 2 provided a literature overview to show that engineering sub-nanometer gaps in metal nanostructures for plasmonics applications are key to study the quantum mechanical effects at nanoscales. The self-assembly process to fabricate the high aspect ratio gaps between silver (Ag) NPs was studied in some depth in Chap. 3 , by comparing different mixed SAMs of thiolates and dithiolates (aliphatic SAMs: EDT, HDT, ODT; aromatic SAMs: BDT, BPDT, OPV, and NDT) using various characterization techniques (TEM, 3D STEM Tomography, UV-Vis, XPS, and UPS). 3D STEM Tomography showed clearly that the gaps are free of metal filaments. TEM gap size characterization indicated that the experimentally measured gap sizes are in good correlation with the molecular length predicted by the CPK model. The aromatic SAMs showed more linear assemblies in UV-Vis than the aliphatic SAMs due to the stronger pi-pi interaction between rigid benzene rings than the intercalating alkyl chains. XPS results further demonstrated the presence of the SAMs in connecting the metal NPs while UPS results revealed that the SAMs could provide control over the energy barrier heights of the studied system.

Chapter 4 demonstrated the realization of quantum plasmon tunnelling by using metal-molecules-metal junctions as a platform and electron microscopy for

S. F. Tan, *Molecular Electronic Control Over Tunneling Charge Transfer Plasmons Modes*, Springer Theses, https://doi.org/10.1007/978-981-10-8803-2_8

characterization. By combining atomic-resolution imaging, single-particle spectroscopy and monolayer molecular control, we demonstrated the direct observation of and control over the quantum plasmon resonances at the length scales in the range 0.4–1.3 nm across the metal-molecules-metal junctions. Besides control over the distance, the SAMs also control the tunnel barrier energy height. The measured resonance frequency of the tunnelling charge transfer plasmon varied from 145 ± 10 THz for monolayers of BDT molecules to 244 ± 3 THz for monolayers of EDT molecules. Through-bond tunnelling is the dominant mechanism of charge transport which is only weakly dependent on the gap size as we observed, in contrast to the alternative through-space model, which would have a very strong gap size dependence. The tunnelling was observed for gap sizes (tunnel distances) up to 1.3 nm, for Ag-BDT//BDT-Ag junctions, which potentially indicated that even longer molecules of perhaps 4–5 nm may also be used for plasmon-asssisted electron tunneling.

Physical-organic studies similar to those discussed in Chap. 4 were also performed on closely-spaced gold (Au) nanocuboids. However, in this case, the dimer gaps suffered from filament formation. This triggered us to study the degradation mechanism of passivated Au and Ag NPs under high energy electron beam. In Chap. 5, a stability study was presented of cuboidal metal NPs under electron beam irradiation, and strategies were discussed for avoiding radiation damage. The thiolated SAMs coated Au nanocuboids suffered from surface diffusion-driven filament formation while the electron beam-induced heating at the metal-ligand interface is dominant for thiolated SAMs-coated Ag nanocubes. Replacing the thiolated SAMs with PVP provides stabilization for both Au and Ag nanocuboids. PVP could act as a diffusion barrier and is more resistant to damage induced by the electron beam.

The synthesis of high-quality cuboidal metal NPs we used for quantum plasmonics requires deeper understanding of the reaction chemistry and kinetics at the nanoscale. Chapters 6 and 7 described the real-time visualization of chemical reactions of cuboidal metal NPs in solution by using liquid-cell electron microscopy techniques. In Chap. 6, a detailed mechanistic study of galvanic replacement reactions between Ag nanocuboids and chloroauric acid was provided. The detailed analysis of Ag removal rate and Au deposition indicated that the morphology and composition of the final product are dependent greatly on the subtle changes of the stoichiometric ratio between Au and Ag.

Chapter 7 demonstrated the overgrowth process of Ag on Au nanocuboids in silver nitrate solution in the presence of the reducing agent ascorbic acid using *in situ* liquid-cell electron microscopy. The detailed analysis of Ag deposition revealed that there are two mechanistic pathways: nuclei coalescence and monomer attachment, both result in the same Au–Ag core-shell nanostructures formation. A comparison of *in situ* and *ex situ* synthesized nanostructures tells us that this reaction may be insensitive to the electron beam and is chemically-mediated by the reducing agent. This study showed that the *in situ* TEM technique not only can be used to study NP growth mechanisms, but also to elucidate the role of the chemical additives.

The results presented in this thesis show that precise control of the structural and opto-electronic properties between two closely-spaced NPs is essential to switch on the quantum plasmon tunnelling. It was shown that the frequencies of the quantum mechanical plasmon modes can be tuned by simply changing the layers of molecules linking two NPs. This study provided a key advance towards the creation of technologically accessible tunnelling length scales of up to 1.3 nm, which is 3–4 times larger than what has been reported before. On the other hand, *in situ* liquid-cell electron microscopy has evolved as a tool to elucidate the reaction mechanism and kinetics during chemical reactions such as galvanic replacement reactions and core-shell NPs formation at the nanoscale. This study provided a quantitative picture of the growth process that is useful for engineering the composition and morphology of metal nanostructures that could potentially open up more opportunities for application in plasmonics.

The ability of molecules to bring two NPs closely together in a controlled way is going to be a primary feature for combining molecular electronics and plasmonics. From the discipline of molecular electronics, it is known that the transport characteristics are dependent on the intrinsic properties of the molecules. This inspired us to study different molecules inside the junctions between two NPs to explore whether more concepts from the field of molecular electronics can be incorporated into the field of plasmonics. It is worth noting that before this demonstration, it was unknown that molecular electronics is possible at all at optical frequencies. The link between the fields of optics and molecular electronics demonstrated in this work may provide potential for molecular control over quantum plasmonic systems through even longer gap sizes (4–5 nm) that are currently accessible by top-down fabrication techniques. Examples of longer molecules with higher conductance values are: biphenyl dithiols derivatives, naphthalene dithiol derivatives, etc. The reconciliation of molecular electronics with plasmonics at engineerable scales may then open up possible new design routes for plasmonic-electronics that combine the small scale of nano-electronics with the fast operating speed of optics. Following up the new ideas that are developed from these results, we hope ultimately to resolve the challenges that are presented in the course of this work, such as the integration of these devices into real opto-electronic circuits.